HIGH TEMPERATURE MATERIAL PROCESSES

An International Quarterly of High Technology Plasma Processes

Volume 14, Number 3, 2010

Jacques AMOUROUX
Pierre FAUCHAIS
Editors

begell house, inc.
publishers

High Temperature Material Processes: An International Journal (ISSN 1093-3611) is published quarterly and owned by Begell House, Inc., 50 Cross Highway, Redding, Connecticut 06896, Telephone: 203-938-1300. US rate for 2010 is $685.00. Add $10.00 per issue for airmail service outside the United States and Canada. All subscriptions are payable in advance. Subscriptions are entered on an annual basis, i.e., January to December. For immediate service and charge card sales, call (203) 938-1300 Monday through Friday 9:00 am – 5:00 pm EST. To order by FAX: (203) 938-1304. Send written orders to Begell House, Inc., 50 Cross Highway, Redding, Connecticut 06896. Payments should be made by dollar checks drawn on a U.S. bank.

High Temperature Material Processes: An International Journal is indexed and abstracted in chemical Abstracts, and covered in SciSearch®, Research Alert®, Materials Science Citation Index®, and Current Contents®/ Engineering, Computing, and Technology.

Printed February 20, 2011

High Temperature Material Processes

An International Quarterly of High Technology Plasma Processes

High Temperature Material Processes

An International Journal Quarterly of High Technology Plasma Processes

Volume 14, Issues 3 **2010**

TABLE OF CONTENTS

HIGH TEMPERATURE MATERIAL PROCESSES **14** (2010) 211-221

NUMERICAL STUDY OF THE REACTIVE SPECIES

D. Pelletier[1], **Y. Delannoy**[2], **C. Trassy**[2]

[1]*SIMAP-EPM, BP 75, 38402 St Martin d'Hères, France. Now at CEA/INES-RDI, BP332, 73377 Le Bourget du Lac, France*
[2]*SIMAP-EPM, BP 75, 38402 St Martin d'Hères, France*

ABSTRACT: Local thermodynamic equilibrium (LTE), frequently used as first approximation in modeling of thermal plasma processes, is sometimes unable to explain experimental results. It is particularly true near a wall and a surface impacted by the plasma jet. In this work, a 2-D custom model using the CFD commercial code Fluent was developed for argon-oxygen inductively coupled plasma (ICP) at atmospheric pressure. The assumption of thermal equilibrium was made but not that of chemical equilibrium. The transport properties were calculated using higher-order approximation of Chapman-Enskog theory. Reaction kinetics rates of dissociation and ionization were also considered. The model was applied to a process torch used for carving experiments on graphite, and the distribution of reactive species brought to the surface was analyzed in terms of reaction rate distribution: the experimental effect of different injection geometries on the distribution of the reaction rate is qualitatively reproduced by the model.

KEY WORDS: inductively coupled plasma, argon-oxygen plasma, non equilibrium, kinetics, thermal plasma process

1. INTRODUCTION

Plasmas at atmospheric pressure are widely used in chemical analysis systems, known as ICP-OES or ICP-MS for inductively coupled plasmas with optical emission spectroscopy, or mass spectroscopy. Those systems use small torches (power $\sim$1 kW, internal diameter $\sim$2 cm) to dissociate the products to be analyzed into atoms, so that the range of operating conditions is only bounded by the limit providing a complete decomposition. Applications of inductively coupled plasmas are now emerging in process engineering, when purity is a main concern and high temperatures are needed (Boulos, 1994). In that case, the operating conditions have to be optimized to produce the desired physicochemical transformations in the gas, at gas/liquid or gas/solid interfaces. For example, the plasma purification process described by Alemany *et al.*, (2002) uses a 40 mm torch powered by a 60kW generator to blow an argon plasma with reactive gases (H_2 and O_2) on liquid silicon to purify it from boron (for photovoltaic applications).

Numerical modeling of atmospheric ICP assuming local thermodynamic equilibrium (LTE) has already been performed, and recently developed to 3-D cases (Bernardi, 2003). The use of these models has allowed the deep understanding of the transport of mass, momentum, energy and temperature fields. From thermodynamic considerations, radicals, excited atoms and ionized species are present in the hot part of plasma systems, inside the torch, but should disappear when the plasma cools down traveling towards the reacting zone. However, because of chemical kinetics, the rate of recombining reactions is limited outside the torch, so that radicals and ions are over concentrated compared to thermodynamic equilibrium.

Some modeling works of inductive thermal plasmas including chemical reaction kinetics have already been proposed. Zhao *et al.* (1990) have developed a kinetic model for argon ICP with $SiCl_4$ injection. Finite-rate dissociation and recombination of diatomic gases in argon plasma have also been modeled (Girschick and Wu, 1990), and compared to an equilibrium model. More recently, Tanaka (2004) has developed a two-temperature chemical non-equilibrium model of a high-power Ar–N_2 ICP, and Watanabe and Sugimoto (2004) have proposed a chemical non-equilibrium (CNE) model of oxygen ICP. Authors point out the importance of the good estimation of thermodynamic and transport properties. The oversimplified estimation, such as use of equilibrium properties and use of the first-order approximation of the Chapman–Enskog method, would cause an error in the numerical results. So, more sophisticated models are required to design new material processing using thermal plasmas.

The present work aims at quantifying the concentration or flux of reactive species provided by such a torch at the reacting interface, so that surface reactions can be studied more precisely. An existing model describing the fluid flow, heat transfer and electromagnetism of a plasma at local thermodynamic equilibrium (LTE) and local chemical equilibrium (LCE), was extended by adding a model for chemical kinetics of ionization and dissociation, i.e. avoiding the LCE hypothesis. In that case, the plasma is a mixture of species at varying temperature and composition, and we calculate it's thermodynamic and transport properties from the energy level of every species and collision integrals between those species. Considering the great amount of basic physical data needed, the model has been run only for argon-oxygen plasmas. Furthermore, the reaction at the surface is extremely simplified by imposing a zero concentration of reactive species (anything except argon), representing an instantaneous reaction, only limited by diffusion in the gas, or a zero flux boundary condition, representing no reaction at all.

The model is applied to a process torch that was used for carving experiments on graphite (Degoulange *et al.*, 2008), which provide a distribution of the reaction rate (speed of carving) for several geometries of oxygen injection in the torch.

2. NUMERICAL MODEL

In this work, the calculations are based on the following assumptions to derive the different governing equations:

(a) The plasma is considered as axisymmetric, and in steady state.

(b) Pressure in the plasma is the atmospheric pressure and the Mach number is low.

(c) The plasma is an ideal gas that can be described by continuum mechanics.

(d) Heavy particles and electrons follow Maxwellian velocity distribution functions, with the same temperature for all species (local thermodynamic equilibrium).

Hypothesis (d) may be approximate in view of results obtained by Mostaghimi *et al*. (1987). They have pointed out that the two-temperature state can be established in argon ICP, even at atmospheric pressure, especially near the wall and probably near a target under the plasma jet. However, the present study is only focused on chemical non equilibrium effects.

The governing equations can be derived from hypothesis (c) as transport equations for mass, momentum, energy, species concentration. The model has been developed using the commercial code Fluent dedicated to fluid dynamics, using a finite volume discretization technique, and the classical Simple C algorithm. Viscosity and thermal conductivity of the mixture are needed to solve those equations.

Two additional transport equations were used to describe the flow turbulence (RNG k-ε), which could become important in cold zones with strong velocity gradients, such as the target of plasma processes. All in all, in the results presented hereafter, the turbulence remains weak.

The electromagnetic field is described, using the A-V formulation of Maxwell's equations, by two other diffusion equations for the complex azimuthal vector potential. The corresponding home-made module provides source terms for the energy equation (Joule heating) and momentum equations (Lorentz forces). It uses the local electrical conductivity calculated from species concentrations and the local temperature. The radiative heat loss is simply modeled by a net emission coefficient, with a thickness of the plasma zone estimated to 5mm, but neglecting the influence of oxygen on the radiative loss. The electromagnetic module and the net emission coefficient technique are described in details by Lacombe *et al.* (2008).

A unique temperature for all species is calculated from the transport equation for the enthalpy of the mixture. Thermodynamic properties (heat capacity, formation enthalpy) are needed for each species, in the present work Ar, Ar^+,

O_2, O_2^+, O, O^+ and e^-. Concentrations of the seven species are calculated from six transport equations (argon is deduced by difference); including individual diffusion of each species (a diffusion coefficient is needed for species j in the mixture). Sources due to chemical reactions (11 reversible reactions), are calculated from the mass action law with modified Arrhenius laws for the forward reaction rate constant:

$$k_f = A.T^b e^{-(E/T)} \tag{1}$$

The backward reaction rate constant, $k_b = k_f/K$ is deduced from the equilibrium constant K, calculated from formation enthalpy and entropy of reacting species, and the temperature. The set of reactions and kinetic data are presented in Table 1.

Table 1: Reaction Set and Associated Kinetic Data for Ar-O_2 ICP.

	k_f			
Réactions	A ($cm^3.mol^{-l}.s^{-1}$)	b	E(K)	Référence
Ar + $e^- \rightleftarrows Ar^+ + 2e^-$	3.06E+13	0.50	135300	Hoffert et Lien, 1967
O_2 + Ar $\rightleftarrows$ 2O + Ar	1.00E+22	–1.50	59500	Park, 1989
O_2 + O_2 $\rightleftarrows$ 2O + O_2	2.00E+21	–1.50	59360	Park et al., 2001
O_2 + O $\rightleftarrows$ 2O + O	1.00E+22	–1.50	59360	Park et al., 2001
O_2 + O^+ $\rightleftarrows$ 2O + O^+	2.00E+21	–1.50	59360	Park et al., 2001
O_2 + e^- $\rightleftarrows$ 2O + e^-	9.68E+22	–2.00	59500	Park, 1989
O_2 + e^- $\rightleftarrows$ O_2^+ + $2e^-$	5.42E+14	2.00	146217	Chung et al., 1994
O_2 + e^- $\rightleftarrows$ O + O^+ + $2e^-$	3.19E+14	0.90	232090	Chung et al., 1994
O + O_2^+ $\rightleftarrows$ O_2 + O^+	2.92E+18	–1.11	28000	Gnoffo et al., 1989
O + O $\rightleftarrows$ O_2^+ + e^-	1.60E+17	–0.98	80800	Gnoffo et al., 1989
O + e^- $\rightleftarrows$ O^+ + $2e^-$	3.91E+33	–3.78	158500	Park et al., 2001

This difficult numerical problem is solved using a stiff chemistry solver, and in-situ adaptative tabulation, both available in Fluent. Furthermore, to converge towards a physically significant state, such a technique needs an accurate and coherent set of physical properties.

3. THERMODYNAMIC AND TRANSPORT PROPERTIES

In contrast with the chemical equilibrium model, where the transport and thermodynamic properties are only function of the temperature, properties in the chemical non equilibrium model are also strongly dependent of the plasma composition.

Transport properties of the plasma, namely the electrical conductivity, the thermal conductivity, the viscosity and the species binary mass diffusion coeffi-

cients, are derived from the Chapman-Enskog theory (Hirschfelder *et al.*, 1964). Higher-order approximation of the Chapman-Enskog theory is needed according to the required accuracy for the computation of the transport properties. Indeed using first order approximation leads to error on the estimation of thermal and electrical conductivities at high temperature. Higher order collisions integrals (basic data to compute transport properties) were taken from different sources found in the literature (Mason *et al.*, 1967, Devoto, 1973, Capitelli *et al.*, 2000). Detailed expressions and methods to compute the transport properties are available in some works (Pelletier, 2006, Bottin, 1999) and would not be developed here. For the treatment of the species diffusion, the notion of effective mass diffusion of species j in the mixture was introduced in the Fick's law. Moreover, for ions and electron, the effective mass diffusion coefficient was doubled to take into account the ambipolar diffusion phenomenon.

The thermodynamic properties, namely the enthalpy and the specific heat at constant pressure, were obtained from equilibrium data for each species (Bolzman's law and partition function). The number of excited levels taken into account is important for the self-consistency of the properties obtained (Bottin, 1999). The resulting enthalpy of the mixture is not the same as in LCE conditions at the same temperature, because of a non-equilibrium composition driven by convecto-diffusive transport and kinetic-limited reaction rates. The enthalpy of species influences directly the thermal transport by diffusion of individual species, which is directly modeled, without the need of a reactional thermal conductivity. Species enthalpy are also responsible for the thermal effects of chemical reactions (heat of reaction), which play a great role in the temperature distribution of the plasma.

4. ATOMIC OXYGEN SUPPLIED BY A PROCESS TORCH TO ITS TARGET

The numerical model has been applied to a process torch, sketched in Fig. 1, made of a copper, water cooled, sectorized wall (cold cage).

The electromagnetic field is provided by a four-turn coil, out of the cold cage, but the induced current in the cold cage was simply represented in the calculations by an uniform current density on the inner surface of the wall, indicated on part b) of Fig. 2. A water cooled copper injector and a silica tube are used to inject three separate gas flows (outer, intermediate, and inner gas). The injector is placed inside the coupling zone, so that the inner gas is not mixed with other flows by recirculations at the top of the coupling zone. The reactive gas, oxygen, was added either to the inner flow, or to the outer flow, to study the effect of the injection geometry.

The calculated streamlines, temperature distribution and molar fraction of atomic oxygen are drawn in Fig. 2 for the case of oxygen injected in the inner

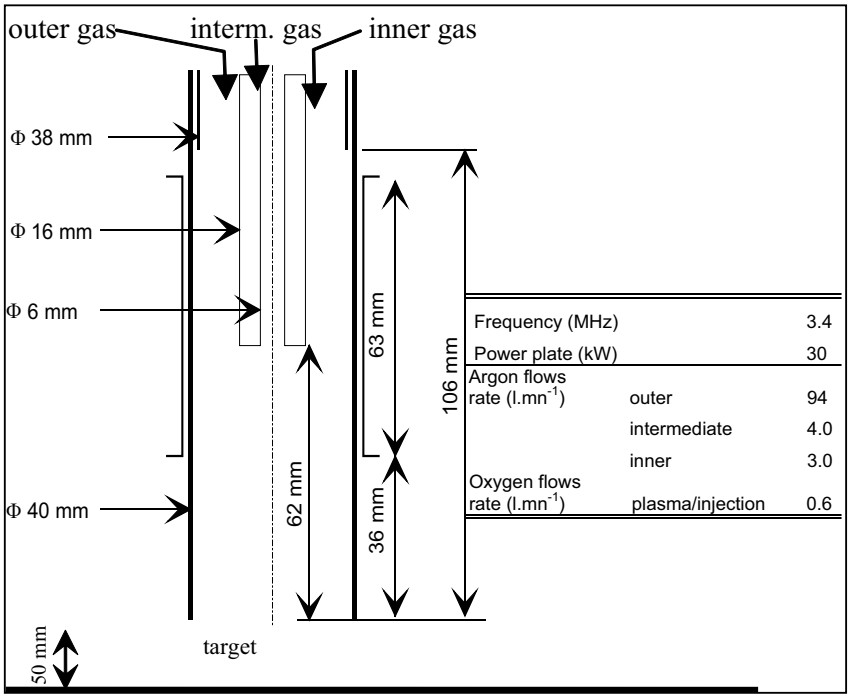

Fig. 1: Sketch of the experimental setup and main operating conditions.

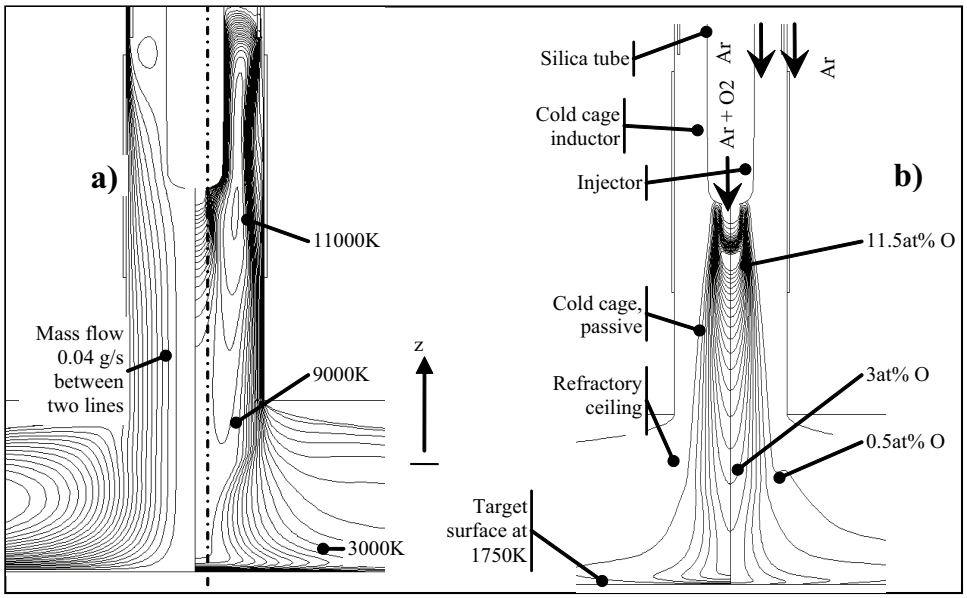

Fig. 2: a) streamlines and temperature distribution calculated for 0.6 l/mn of dioxygen added to the inner gas flow, b) molar fraction of atomic oxygen in the same case, with (on the left) or without surface reaction (on the right).

gas. The reactive gas and the outer flow (which is heated by induction) are only slightly mixed, so that the mole fraction of oxygen arriving in the center of the target is far above the overall flow rate ratio of 0.6%. Furthermore, the inner gas is heated up to 9000K, so that oxygen is present under the form of atomic oxygen above the center of the target (the kinetic of dissociation is very fast compared to the transit time).

To reach the surface, the reactive gas has to cross the hot plasma zone, where it is partially dissociated and partially mixed with other gas flows, and then to cross the boundary layer above the target, where it can be partially recombined and/or consumed at the surface at different radii. The available flux and concentrations for the surface reactions depend of course of the reaction itself, the study of which is out of focus of the present paper. Calculations have been run with two extreme boundary conditions: zero concentration for all species excepted argon that correspond to highly reactive surface, or zero mass flux at the interface, corresponding to chemically passive surface. The recombination in the ”cold” boundary layer is still taken into account in both cases. The resulting concentrations or fluxes are plotted in Fig. 3 for the same flow rate of oxygen (0.6

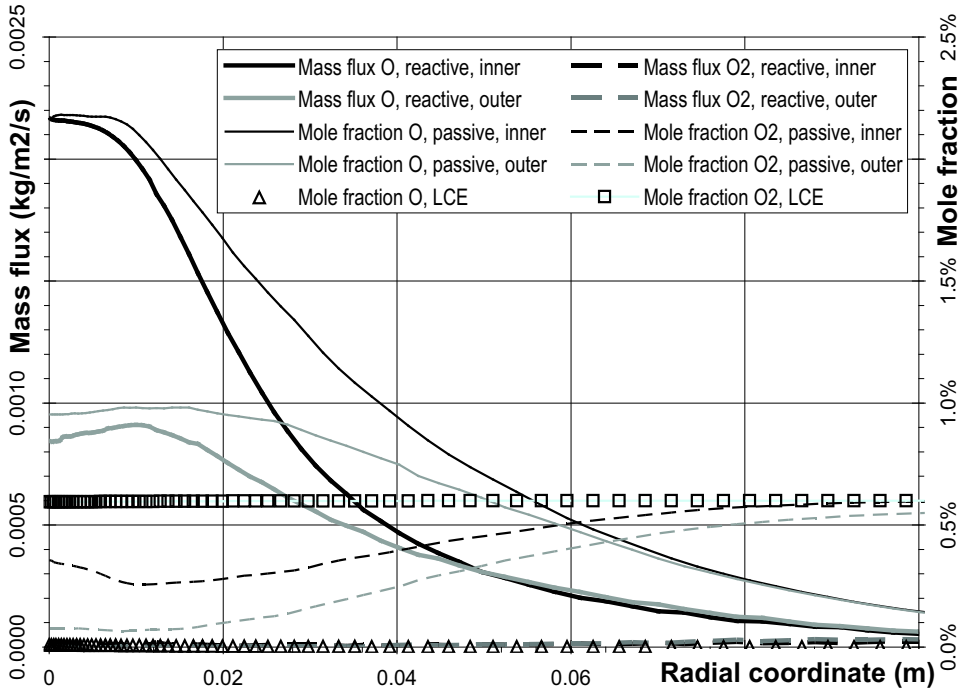

Fig. 3: Oxygen provided on the target surface: mass flux for calculations with zero imposed concentration (reactive surface), mole fraction for calculations at LCE or with zero flux imposed (passive surface). Oxygen added to the inner gas or outer gas as mentioned.

l/mn) added to the inner gas (black curves) or to the outer gas (grey curves). In a real process, the surface reaction would consume a part of the available oxygen, eventually limited by transport of other reactive species (if the target is a liquid), by evacuation of the products of reaction or by surface kinetics. In any case the reaction rate will depend on the flux of oxygen and/or the concentration at the surface, so that its distribution will be similar to the curves plotted in Fig. 3: for a reaction with atomic oxygen, injection in the outer gas will thus give a more homogeneous reaction rate than injection in the inner gas.

The distribution of atomic oxygen flux or mole fraction, presented in Fig. 3, correspond roughly to the profiles of carving obtained on the facility modeled here, when the target is a graphite block reacting with oxygen added to the plasma (Degoulange et al, 2008). More precisely, the radius at mid-depth of experimental carving profiles was approximately 2.5 cm for oxygen injected in the inner gas, and 4.5 cm for oxygen injected in the outer gas (in this last case, the target-torch distance was slightly reduced at 40 mm). Taking the point at half the maximum value of flux or mole fraction in Fig. 3, one obtains from 23 to 33 mm (depending on the reactivity of the surface) for oxygen in the inner gas, and from 37 to 60 mm (reactive to passive surface) for injection in the outer gas. Nevertheless, the experimental carving profiles exhibit a lack of reactivity on the axis (compared to r = 2 cm), for both injection modes, whereas the calculations give it only for oxygen added to the outer gas. In this zone with high reactivity and low flow velocity, a limitation due to the evacuation of gaseous reactive products (CO in experiments, not modeled in our calculations) could be responsible for this discrepancy.

5. NON EQUILIBRIUM PHENOMENON FOR PROCESS PLASMAS

A calculation at chemical equilibrium (LCE) has been run for reference, where the fraction of each species is simply determined from the local temperature and an overall fraction of oxygen atoms deduced from the injected flow rates. Such a calculation predicts no atomic oxygen at the target surface, because of the equilibrium composition at 1750K (O_2 predominant), also plotted in Fig. 3. The chemical non equilibrium is thus an important mechanism to bring reactive species up to the surface, as well as diffusion of individual species in the boundary layer, which is also a non equilibrium mechanism not described by LCE calculations. Boundary layer profiles plotted in Fig. 4 show that the thickness of this boundary layer is approximately 2 mm, whereas the LCE calculation predicts a transition for the species concentration in only 0.5 mm, making it very difficult to develop mass transfer estimations from such a model.

The conditions out of the boundary layer (temperature, velocity and species contents plotted in Fig. 4) change between LCE and kinetic calculations. Nevertheless, the plasma temperature and velocity do not depend on the injection

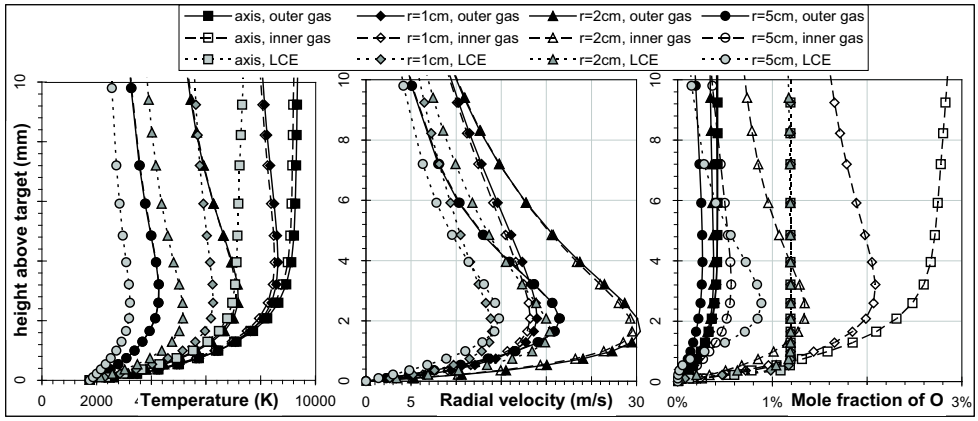

Fig. 4: Profiles of temperature, velocity, and atomic oxygen contents across the boundary layer above the target, at different radii. Reactive surface with O2 added to the outer (black symbols) or inner gas (white), or uniform supply without chemical kinetics (LCE, grey).

mode of reactive gases, which modify only the distribution of reactive species. The species diffusion term, part of the kinetic model, could be responsible of such non equilibrium effects, by modifying the thermal field (by ”reactional” thermal conductivity) and the electrical conductivity, coupled to induction heating (by diffusion of ions and electrons). Delayed reactions (especially recombinations) could also play a role: heat of recombination is brought near the target in kinetic models.

6. CONCLUSIONS AND PERSPECTIVES

The model presented here is able to predict the reactive species brought by inductively coupled plasma to an interface maintained at a prescribed temperature. Compared to experiments, the model is able to reproduce the different distributions of the reaction rates when the injection mode of oxygen is changed (the reaction is more homogeneous when oxygen is added to the outer gas than when it is added to the inner gas). Analysis of the reaction rates in plasma processes could thus be improved with such a model, even if quantitative predictions are not available yet, mainly because of the lack of detailed experiments needed for the validation of the model.

Further modeling is necessary to deal with more complex cases, involving more than one reactive gas, and eventually surface reactions with gaseous products. A specific model for the surface chemistry (based on boundary layer laws for mass transfer) could be developed and coupled to a plasma model, which has then only to describe the reactive species brought to that boundary layer. The

diffusion processes and kinetic limitations of the reaction rates are both included in our model, but a detailed analysis of the results could lead to simplified models with only one of those phenomena for specific zones (hot zone with inductive coupling, post-discharge zone, and boundary layer) of process systems.

REFERENCES

C.Alemany, C.Trassy, B.Pateyron, K-I.Li, and Y.Delannoy, Refining of metallurgical grade silicon by inductive plasma, Solar Energy Materials and Solar Cells (ISSN 09270248), 2002, 72/1-4, pp. 41–48.

D.Bernardi, V.Colombo, E.Ghedini, and A.Mentrelli, Three-dimensional modelling of inductively coupled plasma torches, The European Physical Journal D—Atomic, Molecular and Optical Physics, 2003, 22(1), p. 119.

B.Bottin, Aerothermodynamic model of an inductively coupled plasma wind tunnel—Numerical and experimental determination of the facility performance, PhD thesis, Université de Liège, Liège, Belgium, 1999.

M.I.Boulos, P.Fauchais, and E.Pfender, Thermal Plasmas, Fundamentals and Applications, Vol. 1, Plenum Press, New York, 1994.

M.Capitelli, C.Gorse, and S.Longo, Collision integrals of high-temperature air species, Journal of Thermodynamics and Heat Transfer, 2000, 14(2), p. 259.

T.Chung, H.Yoon, and D.C.Seo, Global model and scaling laws for inductively coupled oxygen discharge plasmas, Journal of Applied Physics, 1994, 86(7).

J.Degoulange, D.Pelletier, B.Bournonville, G.Chichignoud, Y.Delannoy, and C.Trassy, Experimental study of the effect of reactive gas injection geometry in atmospheric pressure inductive plasma torch on the chemical efficiency, 10^{th} HTTP conference, Patras, Greece, submitted to Journal of High Temperature Material Processes, 2008.

R.Devoto, Transport coefficients of ionized argon, Physics of Fluids, 1973, 15(5), p. 616.

S.L.Girshick and W.Yu, Radio-frequency induction plasmas at atmospheric pressure, Mixtures of hydrogen, nitrogen, and oxygen with argon, Plasma Chemistry and Plasma Processing, 1990, 10(4), p. 515.

A.Gnoffo, R.Gupta, and J.Shinn, Conservation equations and physical models for hypersonic air flows in thermal and chemical nonequilibrium, In NASA Technical Paper Publication 2867, 1989.

J.Hirschfelder, C.Curtiss, and R.Bird, Molecular Theory of Gases and Liquids, John Wiley and Sons, New York, 1964.

M.Hoffert et H.Lien, Quasi-one dimensional, non-equilibrium gas dynamics of partially ionised two-temperature argon, Physics of Fluids, 1967, 10(8), p. 1769.

J.G.Lacombe, Y.Delannoy, and C.Trassy, The role of radiation in modelling of

argon inductively coupled plasmas at atmospheric pressure, Journal of physics D: Applied Physics, in press, 2008.

E.Mason, R.Munn, and F.Smith, Transport coefficients of ionized gases, Physics of Fluids, 1967, 10(8), p. 1827.

J.Mostaghimi, P.Proulx, and M.I.Boulos, A two-temperature model of the inductively coupled rf plasma, Journal of Applied Physics, 1987, 61, pp. 1753–60.

C.Park, Assessment of two-temperature kinetic model for ionizing air, Journal of Thermophysics and Heat Transfer, 1989, 3(3), p. 233.

C.Park, J.Richard, and H.Partridge, Chemical-Kinetic Parameters of Hyperbolic Earth Entry, Journal of Thermophysics and Heat Transfer, 2001, 15(1), p. 76.

D.Pelletier, Modélisation de la cinétique chimique dans les plasmas inductifs, PhD Thesis (in french), INP Grenoble, France, 2006.

Y.Tanaka, Two-temperature chemically non-equilibrium modelling of high-power Ar–N_2 inductively coupled plasmas at atmospheric pressure Journal of Physics D: Applied Physics, 2004, 37, pp. 1190–205.

T.Watanabe and N.Sugimoto, Numerical analysis of oxygen induction thermal plasmas with chemically non-equilibrium assumption for dissociation and ionization, Thin Solid Films, 2004, 457, pp. 201–208.

G.Y.Zhao, J.Mostaghimi, and M.I.Boulos, The induction plasma chemical reactor: Part II, Kinetic model, Plasma Chemistry and Plasma Processing, 1990, 10, pp. 151–66.

HIGH TEMPERATURE MATERIAL PROCESSES **14** (2010) 223-232

ANODE CARBON ENRICHMENT IN GMAW

F. Valensi[1,3], **N. Pellerin**[2,3], **S. Pellerin**[1,3], **M. Collumeau**[1,3], **A. Boutaghane**[4], **F. Briand**[5]

[1] *GREMI, Université d'Orléans/CNRS, Rue Gaston Berger, BP 4043, 18028 Bourges Cedex, France*
[2] *CEMHTI, 1D avenue de la Recherche Scientifique, 45071 Orléans Cedex 2, France*
[3] *Université d'Orléans, Avenue du Parc Floral, BP6749 Orléans Cedex2, France*
[4] *Centre de recherche scientifique et technique en soudage, et contrôle, CSC, Alger, Algérie, Route de Dely Ibrahim, BP, 64, Cheraga, Alger, Algérie*
[5] *CTAS, Air Liquide Welding, Saint Ouen l'Aumone, 95315 Cergy-Pontoise Cedex, France*

ABSTRACT: The shielding gas used in the welding process has a strong influence on the metal transfer characteristics. When the gas is chemically active the physicochemical properties of the electrodes can be strongly altered which can increase or decrease arc stability. In order to get a better control over the process it is essential to understand how the electrodes are affected. As the electrode extremities are molten they can easily adsorb gases from the shielding gas, which can affect their microstructure. CO_2 is one of the most commonly used active shielding gases. It is then interesting to know if the liquid metal at the extremity of the electrode can adsorbed the carbon it supplies, as it has strong influence on steel mechanical properties. Besides, various phases can form during metal cooling, depending on its concentration. It is then possible to get information on the carbon content by studying the ratio between phases. In order to show a possible enrichment, only the relative spatial evolution can be studied and no accurate phase identification is needed. Cross sections of the samples have been studied, using mainly optic microscopy. The two main phase ratio have been calculated after processing the obtained images. The results show a higher ratio of the phase associated to the highest carbon content close to the sample periphery, which support the hypothesis of carbon adsorption by the molten metal.

KEY WORDS: welding, microstructure, CO_2, carbon, anode, ferrite

1. INTRODUCTION

In Gas Metal Arc Welding (GMAW), an arc burns between a consumable electrode, usually acting as anode, and the workpiece constituting the other electrode. To

avoid interaction between the melted metal and the air, a shielding gas is used. It can be inert like argon in the Metal Inert Gas (MIG) process or active like CO_2 or argon and CO_2 mixtures in the Metal Active Gas (MAG) process. The metal is transferred as droplets to the weld bead under various working modes depending on the welding parameters (Lancaster, 1984). The most important are arc current and shielding gas composition, but the electrode composition is also relevant regarding the working modes. Under pure argon, the transfer is called "short arc" for current under 150 amperes and occurs by successive contacts between the wire electrode and the weld bead, the resulting short circuits causing large spatter. From 150 to 250 amperes, the transfer is called "globular" with large droplets detaching from the electrode at low frequency in all direction, also causing a high spatter level. For the highest intensities the transfer is called "spray arc" and consist of a stream of small droplets detaching along the wire axis at high frequency, producing few spatter. Users then prefer this later transfer mode. When CO_2 is added to the shielding gas, the main modification is an elevation of the current needed to reach spray transfer. For example with a CO_2 concentration of 10% the spray transfer occurs above 330 A. Under pure CO_2, even for the highest available intensities the transfer remains globular. Apart from the modification of arc stability, we have shown (Zielinska et al., 2009) that the adjunction of CO_2 leads to a modification of the consumable electrode microstructure. The main one is the formation of an oxide layer wrapping the droplet in the case of the globular transfer mode. This gangue concentrates the steel alloying elements, to such extent that the iron element can become a minor component. The gangue has a major influence on the working mode. There are also larger and more numerous precipitates compared to spray transfer modes. The alloying elements also concentrate in these precipitates but in proportions that can differ from the gangue. The steel main alloying elements, in term of quantity, are silicon and manganese, but carbon is also an important one as it has a strong influence on the steel mechanical properties, such as hardness or resistance. The main difference between carbon and the other alloying elements is that it can also be present in the shielding gas in the form of CO_2. Due to the high temperature, the gas can adsorb on the melted metal surface, in particular on the droplet at the end of the consumable electrode. Apart from having influence on steel characteristics, carbon has also an influence on its physical properties under the liquid state as it decreases, like oxygen, the iron surface tension, what can affect the force balance governing the droplet detachment. It is then interesting to get information on the droplet carbon enrichment, and study the migration of this element in the droplet. Unfortunately, small variations of the concentration are not easily detected by direct measurement, as the initial carbon content is low – less than 0.1wt% – and because this element cannot be detected accurately using methods keeping the sample structure. We propose then a method based on the microstructure observation and the various phases study, in order to get more information on carbon concentration. The method used allows yet to get only a qualitative indication of the carbon content evolution,

but further development could possibly lead to quantitative measurement of this element concentration.

2. EXPERIMENTAL PROCEDURE

2.1 Setup

The experimental setup, described in Fig. 1, is organised around a welding generator SAFMIG 480 TRS Plus equipped with a SAFMIG 480 TR 16 kit. This generator used a transistorised power supply controlled by a 16-bit controller. Under the settings used, the current is regulated at the value set by the user while the voltage depends on the welding conditions. The experiments are performed under reverse polarity with direct current. During the process the electrical parameters, are monitored using a voltage probe and a shunt probe to get the current intensity, the data being displayed and recorded on a numerical oscilloscope.In this configuration, that is most commonly used GMAW, the consumable wire acts as anode and the workpiece as cathode. The wire feed speed can also be set manually and is chosen to match the wire melting rate. A 70S mild steel wire (AWS A5.17) was used as consumable electrode, which composition is shown on Table 1. The torch is fixed on a support and the distance between the contact tip end and the workpiece is set at 20 mm. The workpiece consists of a 8 mm thick steel plate and is placed on a table driven by a step motor. This allows creating a relative displacement between the torch and the welded plates as in the case of actual welding. The linear speed is set at 4 mm per second. The gas comes from two bottles of industrial gas of

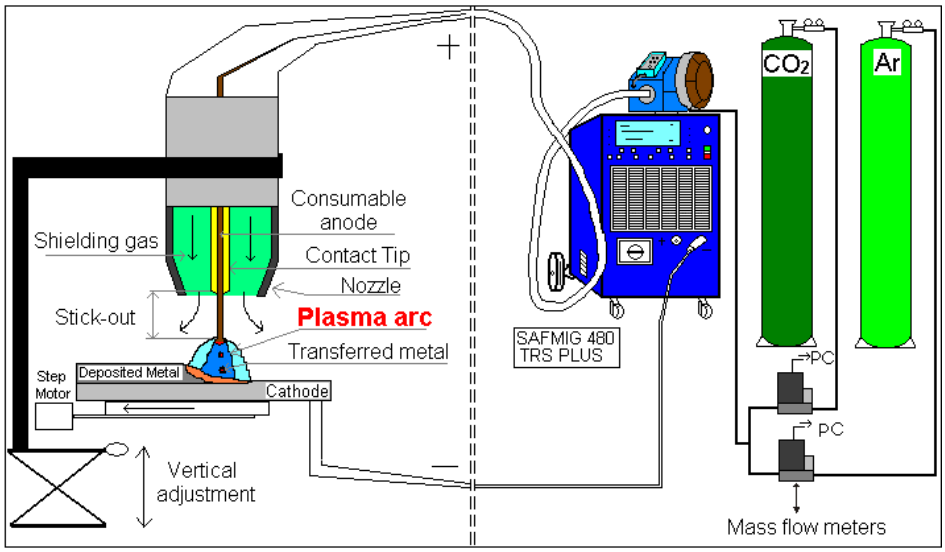

Fig. 1: Experimental setup.

Table 1: Anode wire (70S – AWS A5.17) composition

Wire composition:

Element	Composition (wt.%)	Composition (at.%)
Fe	98.17	97.47
Mn	1.07	1.07
Si	0.35	0.69
C	0.087	0.4
Cu	0.16	0.14
Ni	0.058	0.055
O	0.014	0.048
N	0.0062	0.0244
Cr	0.022	0.023
Mo	0.038	0.022
P	0.011	0.02
S	0.011	0.019
Co	0.008	0.007
V	0.002	0.002
Al	< 0.001	< 0.002
Nb	0.002	0.001
Ti	0.001	0.001
B	0.0002	0.001
Zr	< 0.001	< 0.001

argon and CO_2, as these two gases are the most widely ones used in industry. The flow of each gas is controlled and measured by a mass flow meter BROOKS MASS FLOW CONTROLLERS 5850S which allows getting pure argon, pure CO_2 or an argon-CO_2 mixture. The CO_2 in argon concentration setting step is $0.8_{\text{vol.}}\%$ and the total flow is always kept at 20 L/mn.

3. SAMPLE COLLECTION

Welding experiments have been performed under a current of 330 amperes and a wire feed speed of 9 m/mn. The shielding gas was pure argon (MIG process) and argon/CO_2 mixtures (MAG process) with increasing concentration of CO_2 by a step of $5_{\text{vol.}}\%$ up to $30_{\text{vol.}}\%$. Experiments with a concentration of $40_{\text{vol.}}\%$ and $50_{\text{vol.}}\%$ have also been made. At 330 amperes, the spray transfer is obtained with a CO_2 concentration below $10_{\text{vol.}}\%$; at 240 amperes the arc works always in globular mode except under pure argon where the working conditions are close to the transition to spray transfer.

The welding operation is sustained until the instabilities following arc initiation are over and then shut down a few seconds later. The time needed to reach stability is evaluated using the electrical data and is in the order of one or two seconds. When the arc is shut down, the generator parameters are set so that the last droplet remaining at the end of the consumable wire is nor detached or stick to the weld bead. Then the droplet is cooled down in the shielding gas that is kept flowing after arc extinction. The time needed to cool the droplet down to ambient temperature is considered short enough to get a quench. Indeed, as the temperature drops rapidly one can consider that no significant modification, such as carbon enrichment, occur after arc extinction. As the droplet detachment frequency can be more than a few hundred Hertz, it is not possible to control precisely the droplet growth stage at arc extinction. Then several experiments are made under the same condition to get representative samples. Once the droplet is cooled, the wire is cut once centimetre above the tip. In order to validate this method, some experiments have been made using a hollow cathode setup (Zielinska et. 2009; Valensi, 2007). The droplets that would have been transferred to the weld bead are collected in a water or oil container, providing a more efficient quench.

4. SAMPLE OBSERVATION

Each anode sample is polished to get a cross section along the wire axis. The finest polishing step is performed using alcohol to prevent further oxidation. The droplet are then observed using a scanning electron microscope (SEM) PHILIPS XL 40 coupled with an energy dispersive X-ray spectroscopy (EDS) analysis. The measurements have been completed with an electron microprobe CAMECA SX 50 microbeam. As theses analyses give a poor precision on the carbon concentration, an alternative method has been used. It is based on the fact that steel microstructure depends on the carbon concentration, forming different phases according to the present quantity. Then it becomes possible to get information on the carbon rate evolution in the droplet by observing the evolution of the repartition of the various phases. The sample are then revealed using a $4_{\text{vol.}}\%$ Nital solution ($4_{\text{vol.}}\%$ of nitric acid NO_3^- in ethanol) and observed using an optic microscope LEICA MEF 4M. This method shows the grains defined by contrast differences. The recorded images are then processed using a Matlab program to get the relative importance of the phases. For this they are first converted into a black and white picture by adjusting the threshold so that the image is as few as possible altered. Then the program calculates, for a given area, the ratio of black pixels over white pixels. Due to the small size of the droplet, only three measurement areas have been selected on a single sample. More points have been acquired by comparing the results obtained from several samples obtained under the same experimental conditions.

5. RESULTS

5.1 EDS and Microprobe Analysis

The two main features that appear in the droplet using SEM are oxide precipitates, mainly in globular mode, and an oxide layer ant the periphery, only in globular mode. The alloying elements concentrate in these two structures that can contain up to $50_{wt.}$% of oxygen (S. Zielinska et al., 2009) [2]. The carbon is detected, using EDS, in all part of the droplet. The microprobe analysis show quantities of a few percent, but the precision is almost of this order. It is then impossible to detect a significant evolution of carbon quantity in the droplet.

5.2 Microscope Observation

The optic microscope images show mainly two phases that form grains in the droplet matrix, as seen in Fig. 2. The precipitates appear as the dark spots in Fig. 2a. The clearest phase can be identified as white ferrite, the lowest carbon-containing phase in steel. Its maximum concentration is $0.022_{wt.}$%, at 727 (Barralis and Maeder, 1998). The darkest phase, when observed at high magnification as seen in Fig. 2b, shows small inclusions of a darker phase in the ferrite matrix. This phase can be identified as acicular ferrite (Babu and Bhadeshia, 1990) and corresponds to a higher carbon rate. Indeed, acicular ferrite consists of a fine structure of interlocking ferrite plates, similar to needles, with inclusion of other phases that could contain more carbon. Then the carbon content of acicular ferrite itself cannot easily be defined, as it is a mixture of other phases. As the results are qualitative, the survey of the darkest phase ratio over the clearest one allows only seeing the difference between high and low carbon content areas.

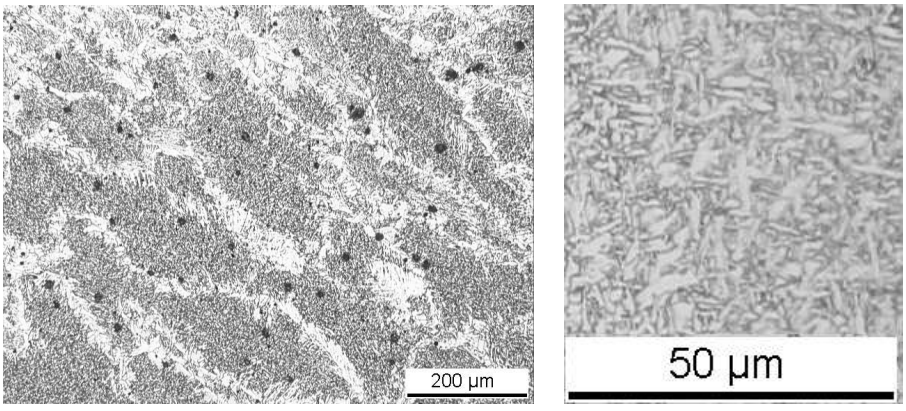

(a) (b)

Fig. 2: Phase identification on wire cross section: general view (a), dark area detail (b).

In spray transfer, the droplets seen in Fig. 3 are smaller than the wire, less than one millimetre in diameter. The main phase is the clearest one, which could support the hypothesis of low carbon content. Due to the small size of the droplets, the evolution of the ratio can not be studied along the droplet, as the required area needed to calculate it is of the same order of the droplet dimension.

In the case of pure argon, some dark grains can be observed in Fig. 3a. Their size is less than 100 μm. In the case of a shielding gas containing $5_{vol.}$% of CO_2, no dark grains can be seen in Fig. 3b. The dark phase forms actually only veins between the clearest areas.

5.3 Carbon Evolution in Droplet

When the CO_2 content in the shielding gas is greater than $10_{vol.}$% the droplets become larger than the wire, which corresponds to the transition from spray to globular transfer. The diameter can increase to 1.5 or even 2 mm in the case of globular mode. The droplets are large enough to discern an evolution of the grain size in their various parts. Contrarily to what happens in spray transfer, the dark phase is the most important one, forming large grains in contrast to the clear matrix, as seen in Fig. 4.

At the droplet periphery, the grains are large and can extend along the curvature of the droplet. The dark phase ratio is then close to 100%. For the lowest value of CO_2 content leading to globular transfer, the dark proportion decreases rapidly towards the centre of the droplet. The minimal value is about 50%, as seen in Fig. 5 in the case of welding under a shielding gas containing $10_{vol.}$% of CO_2.

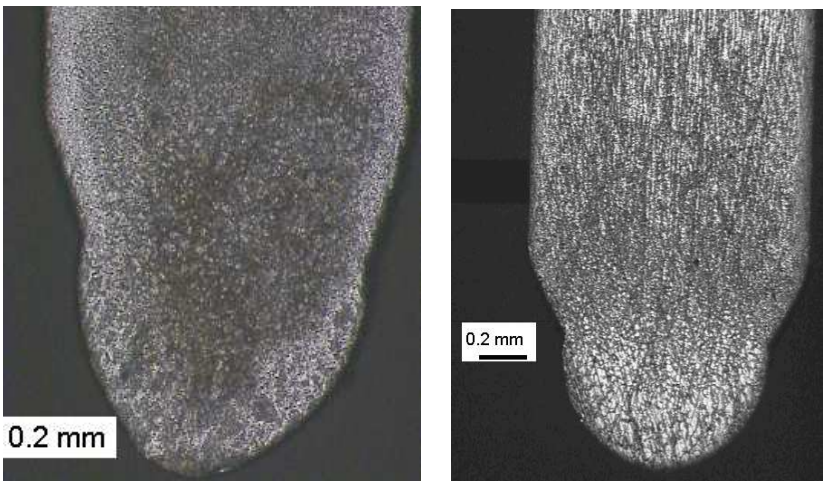

(a) (b)

Fig. 3: Droplet microstructure in spray transfer at 330 A: pure argon (a); Argon + 20 % CO_2 (b).

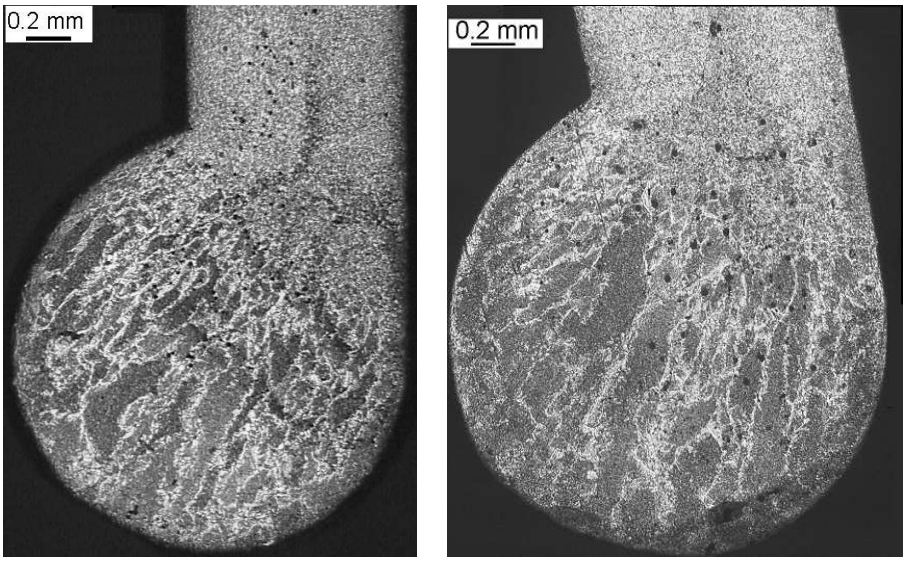

(a) (b)

Fig. 4: Droplet microstructure in globular transfer at 330 A: Argon + 15% CO_2 (a); Argon + 20 % CO_2 (b).

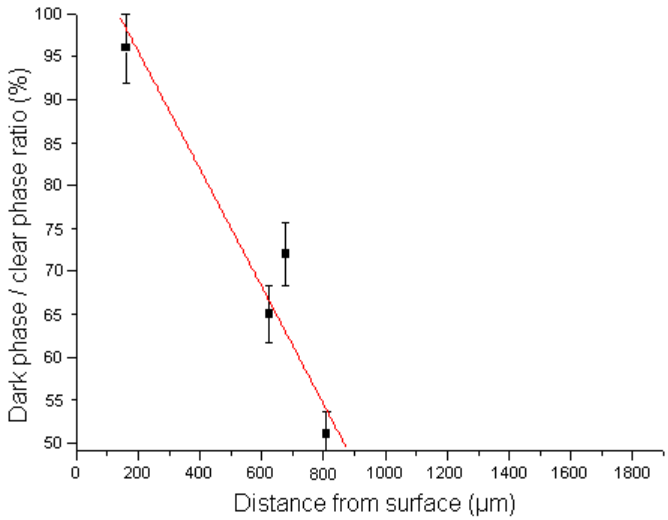

Fig. 5: Dark phase proportion evolution on droplet under Argon + 10% CO_2, I = 330 A.

With a higher CO_2 content in the shielding gas, the carbon concentration decreases more slowly towards the droplet center. The minimal value remains higher than 50%, with values close to 70% as seen in Fig. 6 in the case of a shielding gas containing $20_{vol.}$% of CO_2.

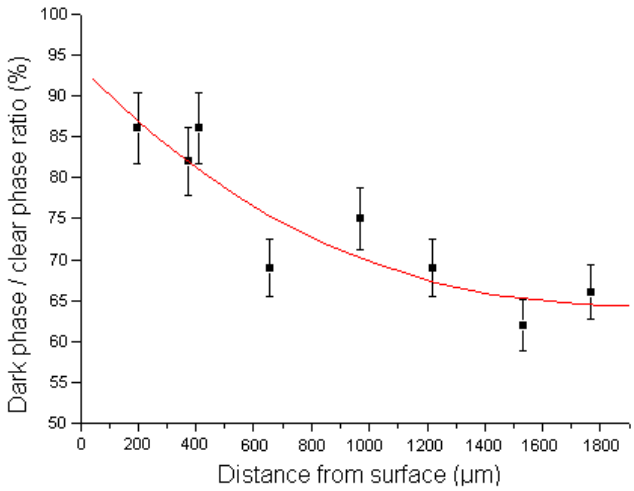

Fig. 6: Dark phase proportion evolution on droplet under Argon + $20_{vol.}$ % CO_2, I = 330 A.

6. ANALYSIS

In the case of MIG welding, it is reported in literature that the droplet composition does not evolve during transfer to the weld bead (Muller et al., 1951). The presence of sparse high concentration areas corresponding to dark grains can then result just from the concentration of carbon initially contained in the wire. The results would seem to indicate lower carbon content in the case of welding with an addition of $5_{vol.}$%, as the dark phase is even narrower. However the droplet is small, which decreases the precision of the method. As the droplet lifetime is short (less than 2 ms) the interaction with the shielding gas is reduced.

When welding under a higher CO_2 content, transfer occurs under globular mode. The droplets become larger and the results seem to indicate carbon enrichment from the shielding gas. In the case of concentration of $20_{vol.}$% and above, the evolution of the dark phase ratio seems to correspond to a diffusion law, supporting the hypothesis of carbon enrichment from the shielding gas.

The maximum quantity of carbon provided by the gas can be estimated by considering its flow and CO_2 content, and the droplet lifetime. When operating at 330 amperes with $20_{vol.}$% CO_2 in the shielding gas, the droplet detachment speed is about 100 Hz (Rhee and Kannatey-Asibu, 1992), which means a 10 milliseconds lifetime. This corresponds to a carbon mass of 93 µg, to be compared to the droplet mass and initial carbon content. The collected samples diameter varied from 1.5 to 2 mm, which leads to a mass from 14 to 33 mg, by taking the solid iron density at 7.8. Based on the wire initial composition, the carbon contained corresponds to a mass from 12 to 29 µg, which equals less than a third of the carbon available in the gas.

Then it seems possible that the carbon concentration at the droplet periphery could be twice as it is at the centre. If all the carbon present in the gas is adsorbed, the droplet concentration would be close to $0.3_{\mathrm{wt.}}\%$

7. CONCLUSION

The droplet microstructure has been investigated under various experimental conditions. The results seem to show a carbon enrichment of the electrode in the case of high content CO_2 shielding gas. The darkest phase that is associated to the highest carbon concentration is more extended at the periphery of the droplet. Its ratio over the brightest phase decreases towards the centre of the droplet where it is closer to 50%. The evolution seems to match a diffusion law, which supports the hypothesis of a diffusion law.

REFERENCES

S.S.Babu and H.K.D.H.Bhadeshia, Transtion from bainite to acidular ferrite in reheated Fe-Cr-C weld deposits, Materials Science Technology, *Materials Science Technology*, 1990, 6, pp. 1005–1020.

J.Barralis and G.Maeder, *Précis Métallurgie: Elaboration, Structures-Propriétés, Normalisation*, Paris: Nathan, 1997, p. 49.

J.F.Lancaster, The Physics of Welding, Pergamon Press, Oxford, 1984, pp. 204–234.

A.Muller, W.Greene, and G.Rothschild, Characteristics of inert-gas-shielded metal-arcs, *Welding Journal*, 1951, 30(8), pp. 717–727.

S. Rhee and S.Kannatey-Asibu, Observation of metal transfer during GMAW, *Welding Journal*, 1992, p. 381.

F.Valensi, Contribution à l'étude des phénomènes liés aux effets anodiques et cathodiques en soudage MIG–MAG, Ph.D. Thesis, Orléans University, France, 2007.

S.Zielinska, F.Valensi, N.Pellerin, S.Pellerin, K.Musiol, C.de Izarra, and F.Briand, Microstructural analysis of the anode in gas metal arc welding (GMAW), *Journal of materials processing technology*, 2009, 209, pp. 3581–3591.

HIGH TEMPERATURE MATERIAL PROCESSES **14** (2010) 233-244

SMELTING OF NIOBIUM PENTOXIDE IN A TRANSFERRED ARC ARGON PLASMA AND CHARACTERIZATION OF THE SMELTED PRODUCT

B. B. Nayak[1], **B. K. Mishra**[1], **S. Pradhan**[2]

[1] *Institute of Minerals and Materials Technology, Bhubaneswar-751013, India*
[2] *Institute for Plasma Research, Gandhinagar-382428, India*

ABSTRACT: Smelting of Nb_2O_5 was carried out in a dc extended arc argon plasma using carbon as the reductant. Plasma was produced in a reactor operating in transferred arc configuration (normal polarity mode). The plasma smelted product was analysed and found to contain up to 97.5% Nb with 86% (all by wt.) metal recovery. Characterization of the smelted product by XRD shows that majority of reflections are due to Nb metal and carbon occurs in the form of carbide. One minor reflection due to Nb_2O_5 was recorded which is attributed to the unreacted oxide. Wavelength dispersive spectra of x-ray confirmed the carbon presence in the smelted product. Micro Raman spectroscopy study makes a comparison between the spectra due to smelted product and that of high pure superconductor grade Nb in order to identify presence of any carbide and/or oxide in the metal. Optical and scanning electron microscope studies reveal the typical surface morphologies of the plasma smelted Nb. Plasma smelted Nb has a good scope for use as a starting material towards preparation of high pure Nb for application in superconductors and electronic capacitors . This can be achieved by suitable removal of carbon followed by electron beam melting of the metal.

KEY WORDS: smelting, plasma, transferred arc, normal polarity arc, niobium pentoxide, high purity niobium, Raman spectra

1. INTRODUCTION

Niobium pentoxide (Nb_2O_5) is a refractory oxide (M.P. 1520°C) which is used as the starting material in the extraction of niobium metal (M.P. 2468°C). Nb is used in alloys for improved strength as in high strength low alloy steel, stainless steel for oil and gas, tool steel, etc. High pure Nb is used in electronic capacitor, sputtering target and low temperature superconductors (Nb-Ti, Nb_3Sn). Because of the refractory nature of Nb_2O_5, and high melting point of Nb, extraction of Nb through pyro metallurgical route is usually not preferred. Some of the difficulties faced in developing pyro metallurgy process include: non-availability of conventional high temperature

furnaces (that are low cost and easy to handle from industrial standpoint), high energy input for endothermic oxide reduction, high reactivity of oxygen with niobium at increased temperatures, non-availability of suitable non-reacting crucible material that can withstand temperatures in excess of 2468°C, and limited numbers of reductants available to work at high temperatures. Therefore, Nb metallurgy is worked out mostly by hydrometallurgical, chemical, and electrochemical routes to overcome expensive high temperature processing. However, the chemical processes including hydrometallurgy and electrolytic processes for niobium, involve number of process steps, unit operations, and toxic wet chemical reactions which create environment pollution. In such a background, it is felt worthwhile to explore and work out some alternate route like plasma smelting of Nb_2O_5. The smelted product, which generally occurs in less pure form of metal, can be further purified over a few more steps to achieve desired level of purity, and thus arc plasma smelting of Nb_2O_5 may open a new scope in the production of high pure Nb used in various applications as highlighted above.

In this paper we report the plasma smelting of Nb_2O_5 carried out in a dc extended arc reactor working in the transferred arc mode. Argon gas was used to produce the plasma and carbon was employed as the reductant for the oxide. Activation energy for the highly endothermic reduction reaction was provided by the argon plasma available in the arc reactor/furnace. In literature, few studies report about carbothermic reduction of Nb_2O_5 using plasma technology (Munz and Chin, 1991) and lack of good characterization techniques available in the seventy's and early eighty's could not correctly evaluate quality of the smelted niobium products. Polyakov and Polyakova (2003) gave an overview of the world wide trends in Nb concentrate, Nb metal, and its alloy production. Nayak and co-workers (Nayak et al., 1989; Sahu et al., 2000; Mishra et al., 2001) have worked on the arc plasma reactor systems over the last two decades and have developed different reactors/furnaces for various kinds of carbothermic reduction of oxide materials (Nayak et al., 1996, 2000). The present work has been taken up based on their past experience in arc plasma smelting using normal polarity arc. Reduction of Nb_2O_5 by carbon requires use of low or sub-atmospheric pressure as per existing literature (Gupta, 2003). However, we find that pressure reduction is not necessary to produce metallurgical grade Nb by the normal polarity arc plasma method. The smelted product has been microstructurally characterized by optical as well as electron microscopy and the purity of the metal thus achieved in the process is discussed in the light of results obtained from XRD, wavelength dispersive spectra of x-ray and micro Raman spectra.

2. EXPERIMENTAL

Niobium pentoxide (Nb_2O_5) powder of 98.5% purity and <63 μm grain size was taken as the starting raw material for carbothermic reduction in a normal polarity

thermal plasma arc reactor. To start with, 10 to 20 wt% excess carbon above the stoichiometric requirement for the reaction Nb_2O_5 + 5C = 2Nb + 5CO, was externally added to the oxide powder in the form of graphite ($<$150 μm grain size) and was intimately mixed. Then the resulting powder mixture was placed inside a graphite crucible which was kept in the hearth of a dc arc plasma reactor operating in the transferred arc mode. Graphite crucible is generally known to provide *in situ* carbon sufficient for maintaining stoichiometric carbon ratio for high temperature reactions in small scale operations. The reactor was subjected to plasma heating by passing Ar through one of the electrodes into the arc zone and applying electric field across the electrodes. Plasma inside an arc reactor is generated initially by ionization of Ar atoms by the impressed electric field which is then followed by collisional ionization of the atoms. Thus, under laboratory condition, few Ar atoms are ionized (not more than 1–2%) but huge energy is released in the form of heat when the ions recombine. Temperature of arc thermal plasma (flame) reaches as high as 8,000 to 10,000°C under such condition. The detailed configuration of the plasma reactor used for this investigation has been reported by Nayak et al. elsewhere (Sahu et al., 2000; Mishra et al., 2001; Nayak et al., 1996, 2008). Arc voltage and current were maintained at 40–60V and 400–550A respectively. Temperature of the charge at the reaction stage in the plasma reactor was monitored by a two colour pyrometer and was found to lie between 2550 and 2650°C.

In the smelting, no external addition of slag was made to the charge; available impurities such as silica, alumina, and calcia existing within the starting Nb_2O_5 and graphite, worked as the slag. Smelting of Nb_2O_5, that melts at 1520°C, was completed in 15 to 20 minutes of arcing after which electric power was switched off and the reactor was cooled for 2 hours. Ar flow was maintained inside the reactor for 15 min after power switch off, in order to prevent oxidation of Nb metal at the initial high temperatures following power switch off. Solid metal product in the form of chunk or mass was manually removed from graphite crucible and then the small amount of slag sitting on the top of metal was mechanically removed. Smelting experiments were done with 100g of charge material. Smelted product was cut and polished for micro structural and chemical analysis. XRD (x-ray diffraction), optical microscopy, SEM (scanning electron microscope), WDS (wavelength dispersive spectra of x-ray) and micro Raman characterization were done to identify Nb. Inductively coupled plasma spectroscopy (ICPS) was employed to analyse percentage of Nb content in chunk sample.

3. RESULTS

Metal yield in the range 74–86% Nb was obtained by the plasma smelting. Chemical analysis of the product by ICPS showed the purity to lie in the range 96–97.5% Nb with presence of 0.06–0.07% Mo as impurity (all by wt%). The product was characterized by XRD using Mo Kα radiation. The identified phases along with

hkl-planes are shown in Table 1 for the best sample which was obtained with 15% excess carbon. The best smelted product was obtained at 86% yield with a 97.5% Nb content. Besides the Nb in metallic phase, presence of some carbides and oxides of Nb were found. However, when the excess carbon addition was increased to 30%, all the Nb reflections vanished and the product was found to consist of a mixture of carbides with a trace of oxide, as shown in Fig. 1.

Figure 2 shows the picture of an overview of the plasma smelted Nb chunk observed under stereo microscope. Figs. 3a and 3b make a comparison between the morphologies observed under SEM for Nb obtained by arc plasma smelting and high purity sample (superconductor grade). Presence of carbon in the plasma smelted sample was confirmed from WDS and the typical spectra shown in Fig. 4 establish the result. Micro Raman spectra of plasma smelted Nb product and niobium carbide (marked BBN), superconductor grade Nb (marked IPR) and standard analytical grade NbC (marked Good fellow) were studied and the spectra are compared in Fig. 5 to arrive at some more conclusive evidence.

Table 1: XRD results for typical plasma smelted product with 97.5% Nb content.

d-value (nm)	Relative intensity (%)	Possible plane (hkl)
0.2322	89.3	110 Nb
0.2188	94.2	200 NbC / 131 Nb_6C_5
0.1798	18.7	206 Nb_2O_5
0.15479	44.7	200 Nb / 220 NbC
0.1317	32.8	211 Nb
0.1170	03.5	220 Nb
0.1095	16.1	310 Nb
0.1089	10.0	222 Nb

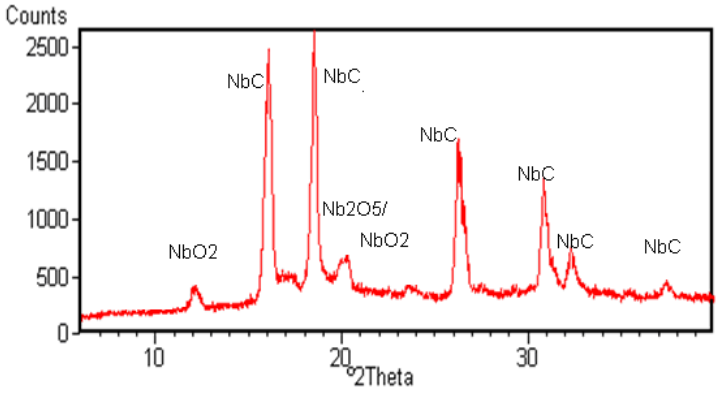

Fig. 1: XRD of arc plasma smelted niobium carbide (30 wt% excess C added in excess of stoichiometry).

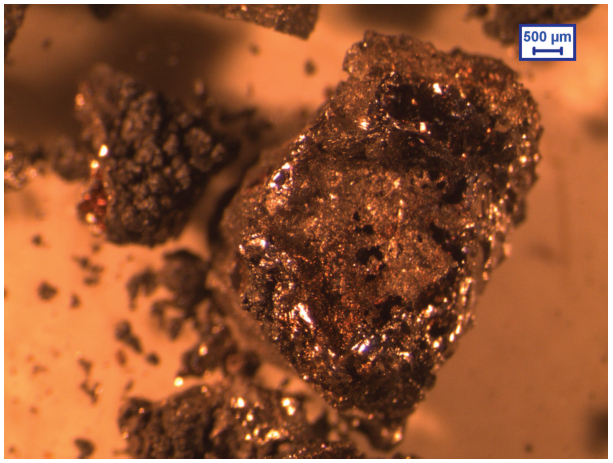

Fig. 2: Typical picture of as-produced metal chunk prepared by arc plasma smelting of Nb_2O_5 (97.5 wt% Nb content).

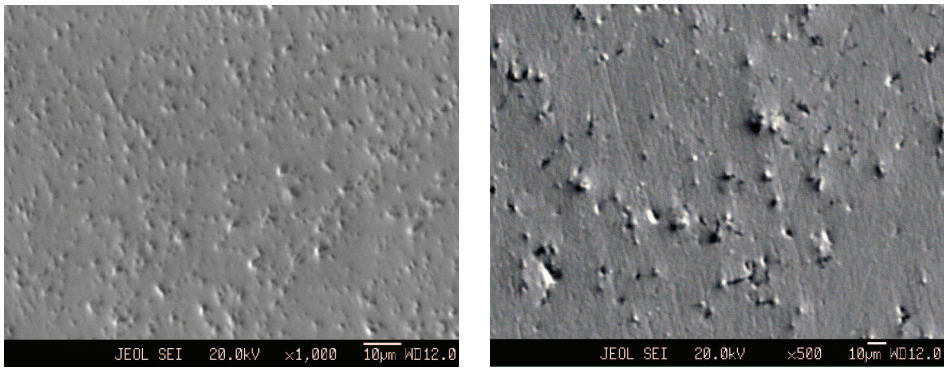

(a) (b)

Fig. 3: SEM image of the surface (a) of plasma smelted Nb (97.5 wt% Nb content) and (b)of the surface of superconductor grade Nb (99.97 wt% Nb content).

4. DISCUSSION

Oxide reduction in niobium is commonly done by aluminothermic process which is simple, inexpensive and fast. Kamat and Gupta (1987) have discussed about the open aluminothermic reduction and purification of reduced metal. Krishnakumar et al. (2002) have reported the removal of about 6% Al and 0.6-1% oxygen in the thermit product that required many steps such as aluminium-deoxidation reaction, sacrificial deoxidation, volatilization of metal vapours and electron beam melting. The lengthy process steps add to energy consumption and increases cost of Nb

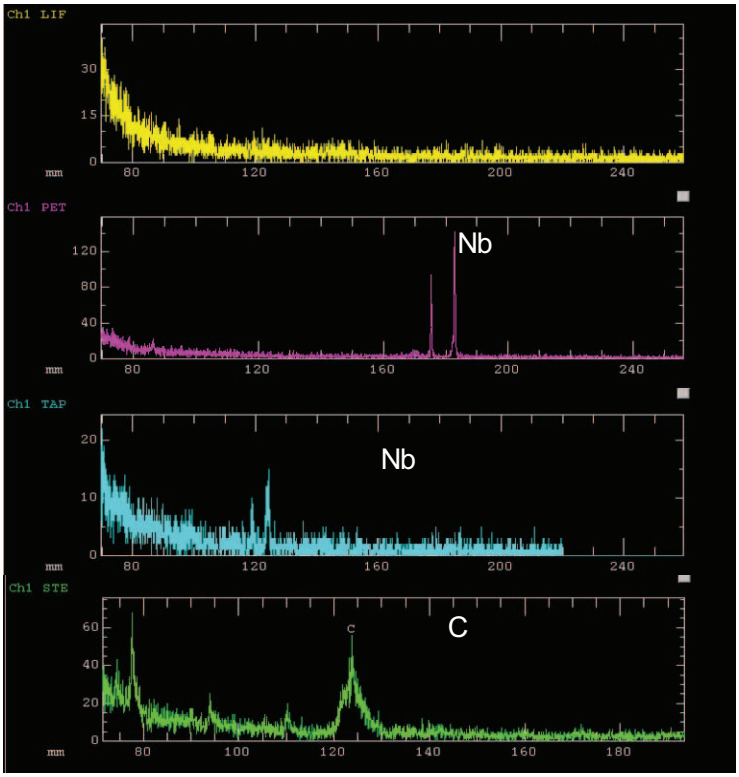

Fig. 4: Typical WDS of plasma smelted Nb (97.5 wt% Nb content); x-axis represents wavelength in nm and y-axis represents intensity counts of detector employing different analyzer crystals.

metal. Recently Gorkunov and Munter (2007) have studied the effect of Ca addition in the aluminothermic process at Silmet JSC, Estonia in the pilot plant scale and found that addition of metallic Ca to the Nb_2O_5 mixture as raw material with 10% excess carbon reduced the Al content in the Nb ingot to 4.4% and increased the Nb content in the final product in excess of 90%. In contrast, when cabothermic reduction process is adopted for Nb production by oxide reduction, carbon as impurity is incorporated in Nb matrix in relatively lesser extent ($\sim$2 wt%) (Gupta, 2003; Nayak et al., 2008) whose removal can be achieved by decarburization with oxygen. The source of oxygen is either the metal where it is dissolved or the atmosphere which has 10^{-2} to 10^{-3} Pa O_2 pressure at 2300 K (Koethe and Moench, 2000). The method is successful to achieve carbon concentration of the order of 10-40 ppm (at.) in Nb. It therefore appears that carbothermic reduction process is more attractive not only from cost point of view but also from the point of view of reduced process steps and pollution. A techno-economic study by Liang and Munz (1981) has shown that carbothermic process in ferro-niobium is cost competitive to aluminothermic process when pyrochlore is used as raw material.

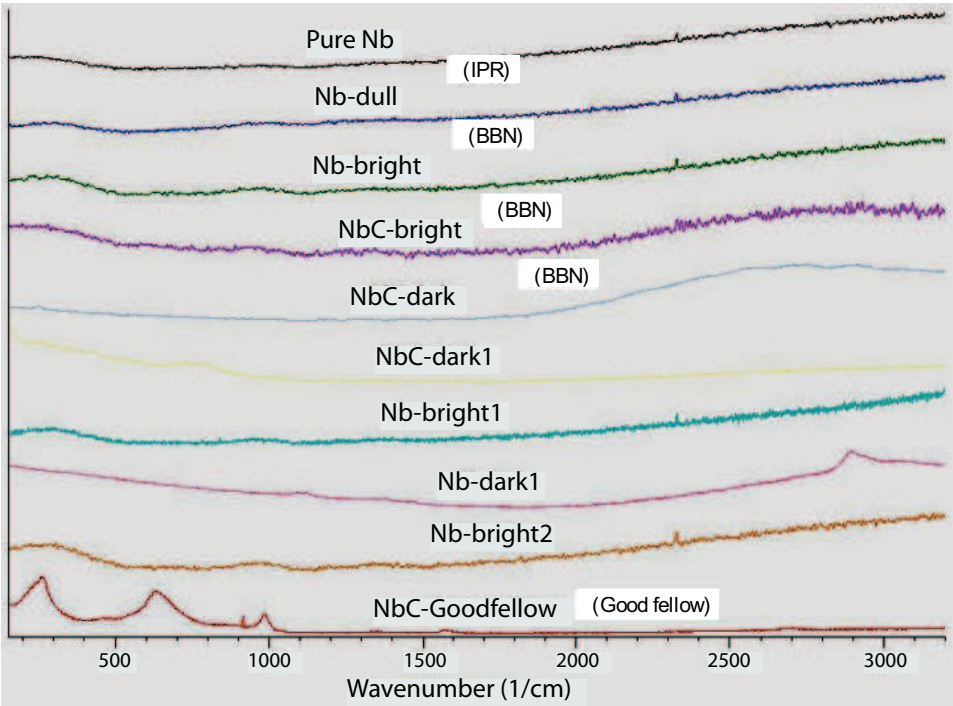

Fig. 5: Micro Raman spectra of plasma smelted Nb (marked BBN) compared with superconductor grade Nb (marked IPR) and standard NbC (Good fellow make).

In the smelting operation reported in the paper, arc plasma is employed in the normal polarity mode with a view to obtain clear metal and slag separation. Argon gas is ionized in the intervening space between cathode and molten Nb_2O_5 surface by application of electric potential (40–60V, arc length $\sim$3 cm) and the active species playing role here are mostly Ar^+ and electron. In arc plasma, the whole arc length can be divided into three regions: a voltage gradient at the anode (V_a), a voltage gradient at the cathode (V_c), and the arc column. V_c is relatively higher than V_a and the voltage gradients at the electrodes generally do not exceed some 20V (Dembovsky, 1985a). For example, in a plasma torch at current intensities between 50 and 200A, V_c is 7 ± 2V (Dembovsky, 1985b). With tungsten cathode and copper anode, V_c and V_a are almost of same order (5–8 V) (Venkatramani, 2002). Taylor and Wang (2001, 2003) and Starostin et al. (1998) introduced reverse polarity method in dc arc plasma processing and its effect on the extraction of refractory metals and steel respectively. In reverse polarity driven metal extraction, the liquid metal at the bottom works as cathode and the molten oxide melt plays the role of an electron transfer layer. Carbon-free chromium and steel with less nonmetallic inclusion are reported to have been produced by the respective groups. However, the reverse polarity method have major disadvantages like temperature gradient existing from top to bottom (resulting in poor slag-metal separation) and decrease

of electrical conductivity of molten glass phase after metal is removed. Up till now the disadvantages hardly seem to have been overcome. In our present study, by changing the polarity of the electrodes, V_c and V_a values are likely to change but the differences resulting in V_c and V_a values are likely to be not more than few volts. Compared to 40-60V potential difference impressed across the arc, these few volt difference may not significantly change the results. Keeping in view the wide scale use of normal polarity arc method in metallurgy and minerals processing for clear metal–slag separation, this paper has chosen the normal polarity method of arc plasma for Nb_2O_5 smelting. The reverse polarity method and polarization issues are not addressed.

Thermal plasma does not behave like an equilibrium or thermodynamic system. However, it may be treated like a system with local thermodynamic equilibrium. In such a situation, the Ellingham diagram is not strictly valid. However, in absence of any good and acceptable theory existing in thermal plasma based reactions, we have tried to use Ellingham diagram for understanding our results in this paper. This may not be considered out of place. Measurement of partial pressure of CO in a semi-open type plasma reactor like ours is not an easy task and thus the working out of detailed reaction kinetics has not been possible. In spite of all these limitations, we have made here an effort to use Ellingham diagram to qualitatively understand our findings/results, particularly, in respect of quality of Nb and product yield.

The chemistry of carbothermic reduction of niobium oxide is not simple. If one looks at the Ellingham diagram (Gupta, 2003) for the free energy of formation of metal oxides and carbothermic reduction of oxides, one finds that CO is actually responsible for the reduction reaction rather than C. Free energy of CO is given by Gupta (2003a):

$$\Delta G = RT\ln(P_2/1) = RT\ln P_2$$

where P_2 stands for partial pressure of CO and

$$\Delta G = \Delta G^\circ + RT\ln P_2$$

At any given temperature ΔG assumes more negative value than ΔG° if $P_2 < 1$. Thus, $2C + O_2 = 2CO$ (P in atm), $P<1$. For this reason, Kruger (Gupta, 2003) suggests that at about 1750°C, and at a CO pressure lower than 10^{-3} atm. carbon is the most efficient reducing agent for oxides.

The Ellingham diagram for Nb-C-O system which shows a plot of RT $\ln Po_2$ vs. T(K) gives clues to the carbide–oxide reaction occurring at a pressure around 10^{-3} atm. The carbon reaction takes place as follows (Gupta, 2003b):

$$\frac{1}{y}M_xO_y + \frac{x+y}{y}C = \frac{x}{y}MC + CO$$

$$MC + \frac{1}{y}M_xO_y = \frac{x+y}{y}M + CO$$

In the case of Nb, three types of reaction as follows are possible (Gupta, 2003c):

(i) Nb_2O_5 +7C = 2NbC + 5CO
Nb_2O_5+5NbC = 7 Nb + 5CO
(Takes place at 10^{-3} atm. pressure; produces 228 m^3 CO per kg of Nb)

(ii) Nb_2O_5 + 5C = 2Nb + 5CO
(Takes place at 10^{-3} atm. pressure; produces 798 m^3CO per kg of Nb)

(iii) $Nb_2O_5 \rightarrow$ NbO
NbO + Nb_2C = 3Nb + CO

Gupta (2003) has reported production of Nb with C<0.2, O<0.1, N<0.2 by oxide–carbide reaction with O/C ratio=1.15 (carbon black is used as source of carbon). The temperature and pressure maintained in this reaction are 2100°C and 10^{-4} atm. respectively.

From the above discussion, it is evident that carbide-oxide reaction under low pressure is required for better recovery and purity of Nb metal. But, it is difficult to ascertain the kind of reaction taking place under the plasma condition adopted in this investigation. First of all, in the semi-open type reactor where low pressure was not applied, the chances of other two kinds of reaction besides the first type carbide-oxide reaction cannot be ruled out. Secondly, and more importantly, the arc plasma although thermal in nature, is characterized by local thermodynamic equilibrium and beyond the main arc zone, thermal gradient (of the order of several hundred degrees over a cm distance) exists. In view of all these issues, it may therefore be stated that Nb_2O_5 smelting in the plasma reactor takes place in a non-equilibrium reaction zone. Also, unlike conventional reaction in gases, in the plasma stage, participation of charged species in chemical reaction accelerate the kinetics. Taking all these points into account, one may lead to conclude that all the three kinds of oxide reduction reactions could be possible in the plasma smelting of Nb_2O_5. It may not be surprising against the above backdrop to find the presence of both Nb and its carbide (small quantity) together in the smelted product (evident from XRD) when kinetics of three different kinds compete in the arc plasma processing.

The d-values determined by XRD were compared with standard d-values of respective metal and compounds available in the International Centre for Diffraction Data (ICDD) base, USA, and the possible phases, planes along with observed relative intensity are given in Table 1. Only carbide peak due to (200) NbC /131 (Nb_6C_5) reflection is seen to appear and it is prominent. The second peak due to NbC is also equally possible for Nb. The oxide peak appearing due to (206) Nb_2O_5 is low in intensity; its origin may be attributed to unconverted oxide from the starting material (charge). Carbide formation may be understood in the light of competing oxide-carbon and oxide-carbide reactions together as highlighted earlier. Carbide reaction generally takes over when excess carbon in higher quantity is added to oxide charge or is available during reduction of metal oxide. To prove this point, 30 wt% excess carbon was added to the niobium oxide charge at the beginning of

smelting experiment. In the subsequent characterization of the smelted product, no Nb peak appeared in the XRD as shown in Fig. 1.

Optical as well as electron microscopy studies were carried out to observe the surface features of plasma smelted Nb. Fig. 2 shows the overall picture of an as-smelted recovered metal chunk (97.5% Nb content). Some dark patches appear on the surface which may be due to unreacted carbon. Brilliant metallic lustre due to grains is marked on the surface. SEM pictures of polished smelted Nb sample and high purity superconductor grade samples are shown in Fig. 3a and 3b respectively. Voids, holes and pores are seen in Fig. 3a where as similar defects (less in number) with presence of few dimples are marked in Fig. 3b. Typical WDS spectra of the plasma smelted Nb product are shown in Fig. 4. It is qualitatively evident that carbon is present in the Nb matrix to a relatively smaller extent.

Micro Raman spectra is a very powerful modern technique to identify presence impurity molecules in metals. Although it is qualitative in nature, the modern spectrometer used here (Renishaw inVia Reflex) with Ar-ion laser source and CCD detector can identify even one Raman active molecule amidst ten million molecules. As such, any pure metal is not Raman sensitive because of aggregation of electrons on the surface. However, when impurity molecules (oxides, carbides etc.) occur in metal, their spectra can be recorded with precision and accuracy by the modern spectrometers. Recently such a tool was ingeniously employed by us to predict the genesis of graphite spherulite in a carbothermally reduced spheroidal graphitic (SG) iron (Pradhan et al., 2007). The micro Raman spectra shown in Fig. 5 for superconductor grade Nb sample (IPR), plasma smelted Nb and NbC samples (BBN), standard NbC sample obtained from M/s Good fellow, UK, gives a comparison among different kinds of spectra for the first time. To study micro Raman spectra, polished sample is first viewed under optical microscope for focusing the laser beam on surface grains. The dark, bright, and dull are attributes of grains as seen under optical microscope. From the micro Raman spectra it is evident that the plasma smelted Nb does not contain much NbC as observed in XRD and SEM studies. Such conclusion is further corroborated from the chemical analysis of sample done by ICPS. ICPS result shows that the plasma smelted niobium sample (prepared from 15 % excess carbon added sample) contains 97.5% Nb which is very much on higher side compared to Nb content in its carbides (88.56% in NbC, 90.281% in Nb_6C_5).

5. CONCLUSION

The normal polarity arc plasma smelting of niobium pentoxide employing carbothermic reduction produces Nb with purity as high as 97.5%. This product is suitable for use as a metallurgical grade niobium in various applications. Low pressure application in the reactor is not required in this process to produce the metal at this grade of purity. Advanced characterization methods such as XRD, SEM, WDS and Micro

Raman spectra, employed to analyse the plasma smelted Nb, show that carbon in the form of carbide is the main impurity with minor presence of niobium pentoxide. Carbon in Nb matrix is generally removed by decarburization at high temperature (2300K) under low pressure oxygen atmosphere. Reverse polarity arc plasma method can also be adopted to produce carbon free Nb if limitation posed due to poor slag-metal separation in the process is overcome. The plasma smelted Nb reported in this investigation can undergo high temperature decarburization to serve as a feed stock for electron beam melting to produce high purity superconductor grade ($>$99.97 %) Nb.

REFERENCES

V.Dembovsky, *Plasma Metallurgy: The Principles*, Elsevier, NY, 1985, (a) pp. 191, (b) pp. 194.

V.Gorkunov and R.Munter, Calcium-Aluminothermal Production of Niobium and Mineral Composition of the Slag, *Proc. Estonian Acad. Sci. Chem.*, 2007, 56, pp. 142–156.

C.K.Gupta, *Chemical Metallurgy: Principles and Practice*, Wiley-VCH, 2003, (a) pp. 363, (b) pp. 365, (c) pp. 370–372.

G.R.Kamat and C.K.Gupta, Open Aluminothermic Reduction of Columbium Pentoxide and Purification of Reduced Metal, *Metall. Trans. B*, 1987, 2, pp. 2817–20.

A.Koethe and J.I.Moench, Preparation of Ultra High Purity Niobium, *Mater. Trans. JIM*, 2000, 41, pp. 7–16.

B.Krishnakumar, K.V.Mirji, D.U.Rao, and S.C.Jain, Development in Processing of Niobium Thermit by Electron Beam Drip Melting, *Proc. of Conference on Power Beams and Materials Processing (PBAMP-2002)*, BARC, Mumbai, India, 2002, pp. 208–215.

A.Liang and R.J.Munz, Ferroniobium Production by Plasma Technology: A Techno-Economic Assessment, *Proc. of 2ndWorld Conf. on Chemical Engineering*, Montreal, 1981, vol. III, pp. 252–256.

S.C.Mishra, B.B.Nayak, and B.C.Mohanty, Arc Plasma Nitriding of Low Carbo Steel, *Surf. Coat. Technol.*, 2001, 145, pp. 24–30.

R.J.Munz and E.J.Chin, The Carbothermic Reduction of Niobium Pentoxide and Pyrochlore in a Transferred Arc Argon Plasma, *Canad. Metall. Q.*, 1991, 30, pp. 21–29.

B.B.Nayak, J.L.Gumaste, S.C.Mishra, S.K.Singh, B.C.Mohanty, R.K.Galgali, U.Syamaprasad, S.Bhatttacharjee, and P.K.Jena, Fe-Al-C Structural and Magnetic Alloys prepared by Plasma, *Proc. of 9th Intl. Symp. Plasm. Chem., Pugnochiuso, Italy*, 1989, vol. III, pp. 1719–1725.

B.B.Nayak, B.C.Mohanty, and S.K.Singh, Synthesis of Silicon Carbide from Rice Husk in a DC Arc Plasma Reactor, *J.Am. Cer. Soc.*, 1996, 79, pp. 1197–1200.

B.B.Nayak, B.C.Mohanty, and R.K.Paramguru, Production of Pig Iron and SG Iron

from Iron Ore Fine by Plasma Smelting, *Trans. Ind. Inst. Met.*, 2000, 53, pp. 639–41.

B.B.Nayak, B.K.Mishra, P.S.Mukherjee, and S.Pradhan, *A process for carbothermic reduction of niobium oxide*, Indian Patent, 2008 (filed).

E.G.Polyakov and L.P.Polyakova, Current Trends in the Production of Tantalum and Niobium, *Metallurgist*, 2003, 47, pp. 33–41.

S.K.Pradhan, B.B.Nayak, B.K.Mohapatra, and B.K.Mishra, Micro Raman Spectroscopy and Electron Probe Micro Analysis of Graphite Spherulites and Flakes in Cast Iron, *Metall. Mater. Trans. A*, 2007, 38A, pp. 2363–2370.

A.Sahu, B.B.Nayak, N.Panigrahi, B.S.Acharya, and B.C.Mohanty, DC Extended Arc PlasmaNitriding of Stainless and High Carbon Steel, *J. Mater. Sci*., 2000, 35, pp. 71–77.

B.M.Starostin, Yu.V.Kofman, N.I.Vorob'ev, A.F.Shkapa, and A.P.Shchetinin, Electroslag remelting in vacuum arc furnaces, *Metallurgist*, 1998, 42, pp. 103.

P.R.Taylor and W.Wang, Producing Carbon–Free Cr/Cr Alloys Using a Reverse-Polarity Transferred-Arc Plasma, *JOM*, January 2001, pp. 25-26.

P.R.Taylor and W.Wang, Reverse–Polarity Dc Plasma-Driven Electro-Reduction of Refractory Metals in Molten Oxide Melts, *SME Annual Meeting and Exhibit, February 24-26, Cincinnati, OH, USA*, 2003, pp. 03–046.

N.Venkatramani, Industrial plasma torches and application, *Current Sci.*, 2002, 83, pp. 254–262.

HIGH TEMPERATURE MATERIAL PROCESSES **14** (2010) 245-253

INFLUENCE OF NICKEL OXIDE AMOUNT ON ELECTRICAL PARAMETERS AND STABILITY OF SUPERCAPACITORS

Ž. Kavaliauskas[1], L. Marcinauskas[2], L. L. Pranevičius[1,3], L. Pranevičius[3], P. Valatkevičius[1]

[1]*Lithuanian Energy Institute, Breslaujos 3, LT-4440, Kaunas, Lithuania*
[2]*Kaunas University of Technology, Studentu 50, LT-51368, Kaunas, Lithuania*
[3]*Vytautas Magnus University, Vileikos 8, LT-44404 Kaunas, Lithuania*

ABSTRACT: A carbon/nickel oxide composite capacitors were made using arc plasma jet and magnetron sputtering deposition techniques. Carbon coatings were deposited on stainless steel substrates at atmospheric pressure from argon-acetylene gases mixture by plasma jet chemical vapor deposition. Nickel oxide (NiO_2) layer was formed on the carbon coating employing magnetron sputtering deposition. The thickness of the deposited nickel oxide film was verified in the range from 18 to 360 nm. In order to characterize differences between produced capacitors, the specific capacitance (C) and maximum working voltage (U) were measured. It was obtained that the increase of NiO_2 film thickness from 18 nm up to 72 nm, increases capacitance from 9 F g^{-1} up to 15 F g^{-1}. Further increase of the metal oxide thickness decreases the specific capacitance value. Experimental results showed that the supercapacitors with thinner nickel oxide layers work much stable. The stability voltages were 0.58 V and 0.35 V, for the capacitors with NiO_2 layer thickness of 18 nm and 360 nm, respectively.

KEY WORDS: supercapacitors, nickel oxide, carbon, capacitance

1. INTRODUCTION

In resent decade, a great attention is focused on the development and research of the supercapacitors. The supercapacitors due to the specific properties (large capacitance, high power density, high efficiency of discharge) are widely used in the electronic devises, uninterrupted power supplies, hybrid cars and power distribution systems (Burke, 2007; Pandolfo and Hollenkamp, 2006; Kotz and Carlen, 2000).

Carbon materials such as carbon black, carbon nanotubes, carbon aerogel, or activated carbon are widely uses as the electrode materials of supercapacitors (SC) (Pandolfo and Hollenkamp, 2006; Kotz and Carlen, 2000; Li et al., 2008; Yuan

et al., 2005; Ganesh et al., 2006). These materials are attractive due to their high surface area, low electrical receptivity, high porosity, and also their remarkable thermal and mechanical properties. The carbon materials are derived from carbon rich organic precursors by heat treatment, sol-gel formation, plasma technology, and etc. (Pandolfo and Hollenkamp, 2006; Li et al., 2008). The plasma jet technology allows easier control of the carbon materials structure and the production of coatings at very high deposition rates (up to 100 nm/s). The high growth rates influence the growth of carbon films with rough, porous, and non-uniform surfaces. Therefore the effective surface area of these coatings will be high enough for their application as double-layer capacitors (Reinhard, 2001; Marcinauskas et al., 2007).

Beside carbon materials metal oxides (Yuan et al., 2005; Liu and Pickup, 2008; Wu et al., 2008), nitrides (Deng et al., 1998), conducting polymers (Alexis et al., 1999) are considering to be promising materials for the creation of redox supercapacitors. It was reported (Liu and Pickup, 2008; Wei-Chun et al., 2004) that ruthenium oxide is the most suitable material for the production of SC. RuO_2 SC performs great reversibility and high specific capacitance (up to 10^3 F g^{-1}). However due to their relative high cost and technological problems of its production new materials are considering as alternatives for the SC fabrication. Nowadays much attention has been paid to low cost metal oxides such as NiO_x (Yuan et al., 2005; Ganesh et al., 2006), SnO_2 (Wu et al., 2008), MnO_2 (Ravinder and Ramana, 2003), and so on (Venkat and Weidner, 2002; Winny et al., 2003). The cost of the nickel oxide is relatively small and the manufacturing technology is very simple comparing to the ruthenium oxide. Good temperature stability, resistance to calcium alkali impact and high dielectric properties makes nickel oxide a great candidate for the application in double-layer SC formation (Yuan et al., 2005; Liu et al., 2006; Zhao et al., 2008; Wu et al., 2006).

Production of the double-layer SC made using carbon material covered by a nickel oxide layer is very promising. NiO_x acts as catalyst and increases the active surface area; due to it higher capacitance values are obtained. Wu et al. (2006) showed that the specific capacitance of the NiO/graphite electrodes was 195 F g^{-1}. However the specific capacitance of SC depends on the nature of the carbon material, nickel oxide fabrication conditions and oxide layer thickness (Pandolfo and Hollenkamp, 2006; Liu et al., 2006; Zhao et al., 2008; Wu et al., 2006; Huang et al., 2007).

The objective of the present study is to form the double-layer carbon/NiO_2 electrode and to investigate the influence of the NiO_2 layer thickness on the specific capacitance and stability voltage of prepared SC.

2. EXPERIMENTAL SETUP

A two-step technology was used for the fabrication of supercapacitor electrodes. The atmospheric plasma torch technology was used for the deposition of carbon

coating on stainless steel 1X18H9T substrates. A detailed description of the plasma torch has previously been given (Akdogan et al., 2006). Formation of nickel oxide on the top of carbon film was done using magnetron sputter-deposition vacuum system.

Carbon layer was deposited at atmospheric pressure conditions from an argon acetylene gases mixture. Argon was used as plasma working gas, and acetylene as precursor, with flow rates of 6.6 l/min and 0.12 l/min, respectively. The arc voltage was 36 V, current –24 A, deposition time –150 s, and the distance between the plasma torch outlet and the sample was 0.01 m. The deposition rate was determined from the slope of the sample‘s weight change obtained using a microbalance with a weight uncertainty of 2 μg.

The deposition of the NiO_2 was done using reactive magnetron sputtering. A water cooled substrate holder and a shutter were located in front of the magnetron. The target-to-substrate distance was 0.06 m. The chamber was evacuated to a typical background pressure of 10^{-5} to 10^{-4} Pa by a pumping unit. This unit includes a turbomolecular pump at pumping speed about 150 $\ell \cdot s^{-1}$ for Ar, which was controlled by a throttle valve. The sample temperature was controlled with the accuracy ± 5 ∘C. The steady state sample holder temperature during the film deposition was 400 K which was reached after two minutes of irradiation. The deposition parameters of the nickel oxide layers were following: magnetron voltage –244 V, current –1.5 A, estimated partial pressure of the oxygen gas 1.36÷1.85 Pa. The deposition times were 15, 30, 60, 120, 180, and 300 s, which lead to growth of nickel oxide films with thickness of 18, 36, 72, 144, 216, and 360 nm, respectively.

The surface topography analysis of fabricated electrodes was carried out using a scanning electronic microscope (SEM) JSM – 5600. The carbon coating was characterized by Raman scattering (RS) spectroscopy. The RS spectra were recorded by conventional grating Raman spectrometer. For excitation of the Raman spectra argon ion laser, operating at 488 nm wavelength with 20 mV power was used. The overlapped background corrected Raman spectral bands were fitted using least squares fitting software. Concentrated potassium alkali KOH (10 mol·dm^{-3}, 40 ml) was used as electrolyte. The electrical characteristics of fabricated supercapacitors were measured using a typical electrical circuit (Pandolfo and Hollenkamp, 2006).

3. RESULTS AND DISCUSSION

In order to evaluate structure of the deposited carbon layer RS measurement was used. As seen from Fig. 1 the RS spectrum has two separate D and G peaks lied at 1360 cm^{-1}and 1607 cm^{-1}. The G peak refers to the symmetric E_{2g} carbon–carbon stretching mode in graphite-like materials. The D band assigns to the zone edge A_{1g} mode activated by disorder. The relative ratio of the D peak to G (I_D/I_G) indicates relative ratio of sp^3 to sp^2 sites in the films. A smaller I_D/I_G ratio shows higher

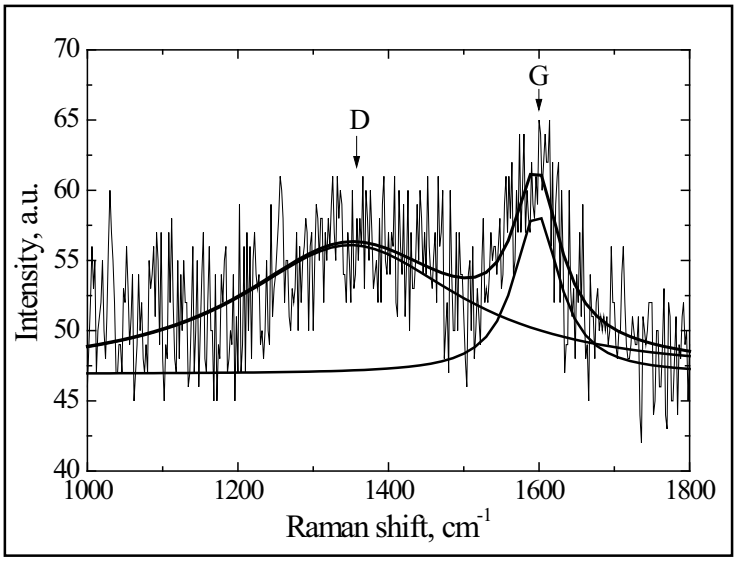

Fig. 1: Raman spectrum of carbon layer.

sp^3 content (Robertson, 2002). The D-band and G-band full width at half-maxima (FWHM) is 306 cm^{-1} and 62 cm^{-1}, while the relative integrated intensity ratio I_D/I_G is 4.52. The broad D peak and high I_D/I_G ratio suggests the presence of large concentration of sp^2 carbon sites in the film (Robertson, 2002; Kim et al., 2003). The narrow FWHM of the G band shows that the bond angle disorder of the carbon sites is low and graphitic domains structure are close to microcrystalline graphite. Similar intensity values of both D and G peaks associated with existence of glassy carbon inserts in the coating (Robertson, 2002).

SEM micrographs indicated that after deposition of various nickel oxide layers surface morphology changes (Fig. 2). The as-deposited carbon film exhibits self-developed micro formations and contains many loosely adhered particles. Rough cluster formations, randomly distributed with deep holes between clusters were obtained after deposition of 18 nm nickel oxide layer. It may be noticed that the clusters consists of the grains with 500 nm size, which are agglomerated into different size (mostly 1–10 μm) clusters.

If the thickness of the nickel oxide reaches 72 nm, SEM surface morphology changes to 3D mesh-like structure (Fig. 2c). The structure of this electrode is composed from many interconnecting pores. It may be noticed that the density of this film will be very low; however the effective surface area will be high. The further increase of the NiO_2 film thickness decreases the porosity of carbon layer and mesh-like structure is transformed into a grain-like one. The double-layer carbon/NiO_2 electrodes with the nickel oxide thickness of 144 nm (Fig. 2d) and 216 nm (Fig. 2e) still have some fragments of the mesh-like structure; meanwhile it completely disappears when the NiO_2 layer thickness is 360 nm (Fig. 2f).

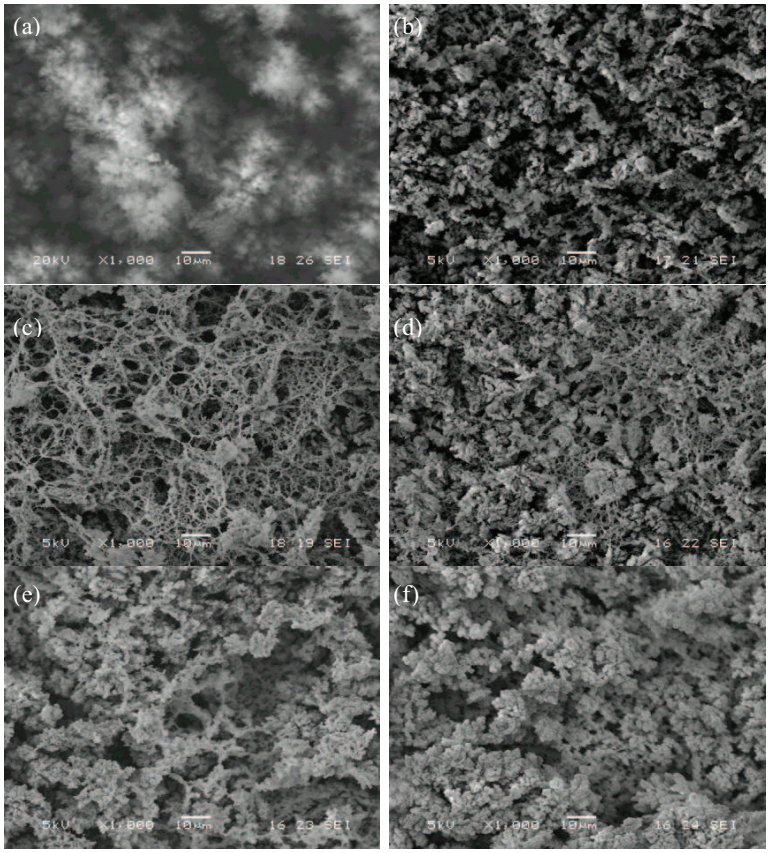

Fig. 2: Surface morphology of as-deposited carbon film (a) and carbon layers after formation of various thicknesses of NiO_2 films: (b) 18 nm, (c) 72 nm, (d) 144 nm, (e) 216 nm, and (f) 360 nm.

Studies of electrical characteristics of the supercapacitors have shown that the electrical properties of obtained double-layer electrodes significantly changed if on the surface of carbon layer a different amount of NiO_2 is formed by magnetron sputtering deposition. Influence of the effective thickness of deposited NiO_2 film on the supercapacitor specific capacitance is presented in Fig. 3.

The specific capacity increases and reaches a maximum value (15 F g^{-1}) for the thickness of the 72 nm, and when starts decreasing with the increase of the NiO_2 film thickness. The highest capacity value for 72 nm thickness of NiO_2 may be explained by the fact that the surface morphology is the most porous due to existence of the mesh-like structure. It also indicates that the surface area at these conditions is the highest one. Li et al. (2008) found that carbon layer, which consists of smaller particles, has higher surface area, hence facilitating ions transport to the pores. As a result the specific capacitance also will be higher. It indicates that

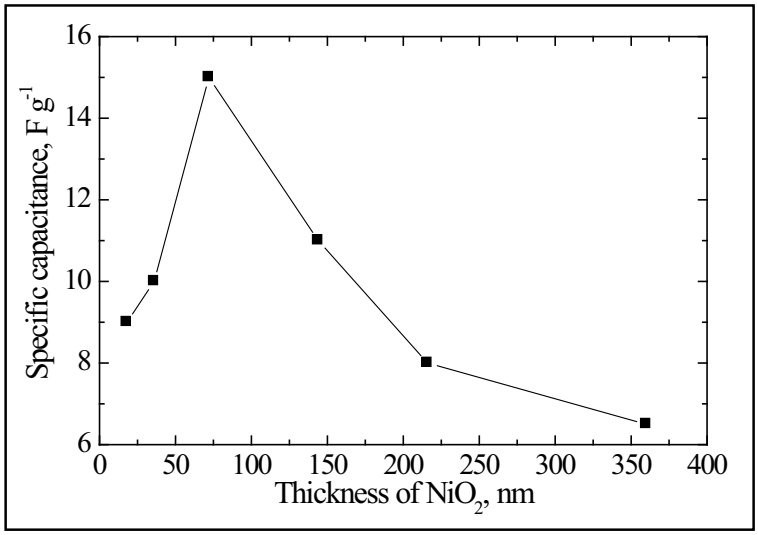

Fig. 3: Dependence of specific capacitance on the nickel oxide layer thickness.

the surface topography has huge effect on the specific capacitance. A substantial decrease of the capacity at nickel oxide layers higher than 72 nm is related not only with the decrease of the effective surface area, but also due to the increase of the distance between electrode surface and ion layer (Liu and Pickup, 2008). This effect is observed for the electrodes with NiO_2 of 144 nm and 216 nm. The surface morphology is similar, however specific capacity decreases from 11 F g^{-1} to 8 F g^{-1}. The changes of the surface morphology could be explained by the plasma etching phenomenon. Formation of the nickel oxide island occurs at the low quantities of deposited NiO_2. Oxygen atoms arriving from the plasma react with available carbon atoms and initiate chemical plasma etching, due to it the effective surface increases. Meanwhile at the high quantities of NiO_2, the nickel oxide formations block heterogeneous reaction between oxygen and carbon atoms and the increasing amount of deposited NiO_2 smoothes surface geometry. It will lead to the disappearance of the mesh-like structure (Fig. 2f).

Measurements of the stability voltage indicated that increase of the effective thickness of NiO_2 from 18 nm to 72 nm decreases the stability voltage from 0.58 V and 0.35 V (see Fig. 4). However, if the nickel oxide layer thickness is equal or more than 72 nm, the stability voltage keeps an almost constant value. This phenomenon of the stability voltage probably is due to insufficient ion kinetics at small nickel oxide layer thicknesses. As the NiO_2 layer thickness increases, the ions kinetics become better, and it leads to the reduction of stability voltage. The steady-state stability voltage value for the films thicker than 72 nm suggests that the kinetics of ions does not change.

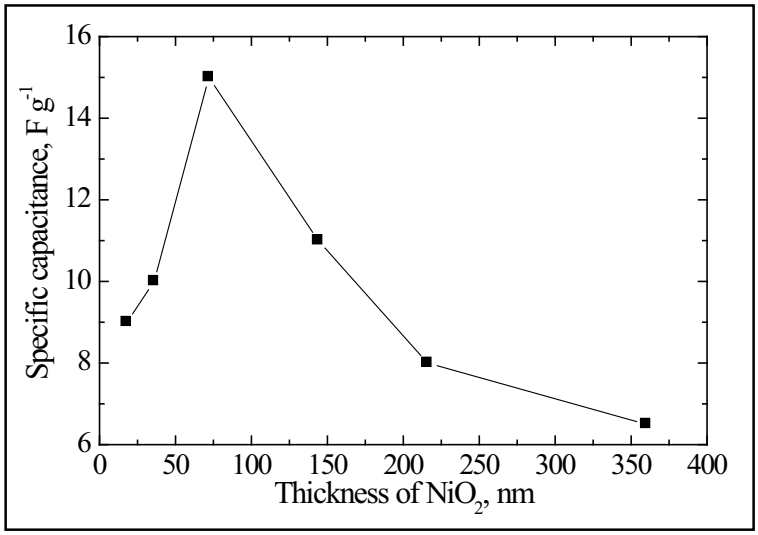

Fig. 4: Dependence of stability voltage on the nickel oxide layer thickness.

4. CONCLUSIONS

Double-layer carbon/NiO_2 electrodes were prepared by plasma jet and the reactive magnetron sputter deposition techniques. RS measurement indicated that carbon layer consist of sp^2 carbon sites and are attributed to graphite-like coating with glassy carbon phase inserts. A dependence of nickel oxide layer thickness on the electrode electrical parameters was demonstrated. It was confirmed that the surface morphology and effective surface area has the highest value when nickel oxide layer thickness is 72 nm. It corresponds to the highest specific capacitance value (15 F g^{-1}). Further increase of the thickness reduces the specific capacitance and the carbon/ NiO_2 electrode with 360 nm nickel oxide layer shows only 7 F g^{-1} capacitance. Experimental results showed that supercapacitors with thinner nickel oxide layers work in a much stable way. The stability voltage decreases from 0.58 V to 0.35 V increasing the thickness of NiO_2 film from 18 nm to 72 nm. Further increase of the nickel oxide layer thickness has no effect on the stability voltage of prepared supercapacitors.

REFERENCES

E.Akdogan, D.Cokeliler, L.Marcinauskas, P.Valatkevicius, V.Valincius, and M.Mutlu, A new method for immunosensor preparation: Atmospheric plasma torch, *Surface and Coatings Technology*, 2006, 201, pp. 2540–2546.

L.Alexis, S.Patrice, S.Christian, and F.Jean-François, Polythiophene-based supercapacitors, *J. Power Sources*, 1999, 80, pp. 142–148.

A.Burke, R&D consideration for the performance and application of electrochemical capacitors, *Electrochimica Acta*, 2007, 53, pp. 1083–1091.

C.Z.Deng, R.A.J.Pynenburg, and K.C.Tsai, Improved porous mixture of molybdenum nitride and tantalum oxide as a charge storage material, *J. Electrochemical Society*, 1998, 145, pp. L61–L63.

V.Ganesh, S.Pitchumani, and V.Lakshminarayanan, New symmetric and asymmetric supercapacitors based on high surface area porous nickel and activated carbon, *J. Power Sources*, 2006, 158, pp. 1523–1532.

Q.Huang, X.Wang, J.Li, C.Dai, S.Gamboa, and P.J.Sebastian, Nickel hydroxide/activated carbon composite electrodes for electrochemical capacitors, *J. Power Sources*, 2007, 164, pp. 425–429.

Y.T.Kim, S.M.Cho, W.S.Choi, B.Hong, and D.H.Yoon, Dependence of the bonding structure of DLC thin films on the deposition conditions of PECVD method, *Surface and Coatings Technology*, 2003, 169-170, pp. 291–294.

R.Kotz and M.Carlen, Principles and applications of electrochemical capacitors, *Electrochimica Acta*, 2000, 45, pp. 2483–2498.

J.Li, X.Wan, Y.Wang, Q.Huang, C.Dai, S.Gamboa, and P.Sebastian, Structure and electrochemical properties of carbon aerogels synthesized at ambient temperatures as supercapacitors, *J. Non-Crystalline Solids*, 2008, 354, pp. 19–24.

X.Liu and P.Pickup, Ru oxide supercapacitors with high loadings and high power and energy densities, *J. Power Sources*, 2008, 176, pp. 410–416.

H.Liu, P.He, Z.Li, Y.Liu, and J.Li, A novel nickel-based mixed rare-earth oxide/activated carbon supercapacitor using room temperature ionic liquid electrolyte, *Electrochimica Acta*, 2006, 5, pp. 1925–1931.

L.Marcinauskas, A.Grigonis, V.Valinčius, and P.Valatkevičius, Surface and structural analysis of carbon coating produced by plasma jet CVD, *Materials Science*, 2007, 13, pp. 269–272.

A.Pandolfo and A.Hollenkamp, Carbon properties and their role in supercapacitors, *J. Power Sources*, 2006, 157, pp. 11–27.

N.R.Ravinder and G.R.Ramana Sol-gel MnO_2 as an electrode material for electrochemical capacitors, *J. Power Sources*, 2003, 124, pp. 330–337.

D.Reinhard, Diamond Thin Films Handbook, New York: Marcel Dekker Incorporated, 2001, p. 686.

J.Robertson, Diamond-like amorphous carbon, *Materials Science and Eng.*, 2002, 37, pp. 129–281.

S.Venkat and J.Weidner, Capacitance studies of cobalt oxide films formed via electrochemical precipitation, *J. Power Sources*, 2002, 108, pp. 15–20.

C.Wei-Chun, H.Chi-Chang, W.Chen-Ching, and M.Chun-Kuo, Electrochemical characterization of activated carbon-ruthenium oxide monoparticles composites for supercapacitors, *J. Power Sources*, 2004, 125, pp. 292–298.

D.Winny, S.S.Jeffrey, and D.Bruce, Electrochemical properties of vanadium oxide aerogels, *Science and Technology of Advanced Materials*, 2003, 4, pp. 3–11.

M.Wu, J.Gao, S.Zhang, and A.Chen, Comparative studies of nickel oxide films on different substrates for electrochemical supercapacitors, *J. Power Sources*, 2006, 159, pp. 365–369.

M.Wu, L.Zhang, D.Wang, C.Xiao, and S.Zhang, Cathodic deposition and characterization of tin oxide coatings on graphite for electrochemical supercapacitors, *J. Power Sources*, 2008, 175, pp. 669–674.

G.Yuan, Z.Jiang, A.Aramata, and Y.Gao, Electrochemical behavior of activated-carbon capacitor material loaded with nickel oxide, *Carbon*, 2005, 43, pp. 2913–2917.

D.Zhao, M.Xu, W.Zhou, J.Zhang, and H.Li, Preparation of ordered mesoporous nickel oxide film electrodes via lyotropic liquid crystal templeted electrodeposition route, *Electrochimica Acta*, 2008, 53, pp. 2699–2705.

HIGH TEMPERATURE MATERIAL PROCESSES **14** (2010) 255-270

SIMULATIONS AND MEASUREMENTS OF THE PRE-ARCING TIMES IN HBC FUSES UNDER TYPICAL ELECTRIC FAULTS

S. Memiaghe[1,3], **W. Bussière**[1,3], **D. Rochette**[1,3], **R. Touzani**[2,3], **P. André**[1,3]

[1]*Laboratoire Arc Electrique et Plasmas Thermiques CNRS FRE 3120, Phys. Bât. 5—Université Blaise Pascal 24, Avenue des Landais 63177 Aubière Cedex, France*

[2]*Laboratoire de Mathématiques CNRS UMR 6620, Campus Universitaire des Cézeaux, 24 Avenue des Landais, F63177 Aubière Cedex, France*

[3]*P.R.E.S. Clermont Université, 9 rue Kessler B.P. 10448 63012 Clermont-Ferrand Cedex 1*

ABSTRACT: This work deals with the comparison between calculations and measurements of pre-arcing times in High Breaking Capacity fuses under typical fault current conditions. This paper also describes the temperature evolution and the Joule energy dissipated in a fuse element during the pre-arcing time. By varying typical electrical parameters, namely the closing angle and the power factor, we show that various prospective currents such as those observed in industrial case can be fairly simulated. The pre-arcing time and then the clearing of the fault current are shown to be deeply dependent on these electrical characteristics. We exhibit simulated results of prospective current and supply voltage waves for given closing angles under two typical power factors which are compared with the experimental ones. A comparison between simulated pre-arcing times with experimental ones shows some discrepancies and a discussion on the numerical assumptions is made.

KEY WORDS: HBC fuses, pre-arcing time, closing angle, power factor, prospective current

1. INTRODUCTION

The role of High Breaking Capacity (HBC) fuses is to restrict the damages to the persons and to the electrical equipments by limiting and interrupting prospective faults occurring in power distribution networks and in industrial installations. This is realized by means of the combination of four main elements from which HBC fuses are built. A typical HBC fuse consists of a calibrated silver fuse element. This fuse

element configuration (geometry and notches regularly spaced through the length) and its physical properties (resistance for example) are selected to achieve a good conducting current path through the fuse. The current path is also ensured by fuse contacts (in each end side of the fuse) in which the fuse element is welded. The fuse element is surrounded by silica sand as filler which role is to absorb the heat generated by the fuse element and to absorb the arc energy when the fuse clears the fault current. The fuse element and the filler are enclosed in a mechanically and thermally strengthened cylindrical fuse body. When a sustained overload occurs, the fuse element will generate heat (especially in the notches) dissipated along the fuse length in a first time, and in a second time the heat can be passed to the filler. If the overload persists and becomes higher, the thermal equilibrium is not achieved in the fuse, and then the fuse element reaches firstly its melting point, secondly its vaporization point and finally disrupts by the appearance of an electric arc (Wright and Newberry, 2001). Industrialists call this time step the pre-arcing time. The electric arc created leads to a silver plasma composed of metallic vapours. When increasing its length (burn-back phenomenon), the electric arc also interacts with the sand filler due to the energy brought by the fault. Once the electric arc is much longer, this latter could not be maintained by the supply voltage and then the current in the fuse falls to zero. This defines the arcing time. The whole fuse operation is usually divided in these two latter stages (Wright and Newberry, 2001).

In the past many authors were interested in the optimization of fuse performance with special reference to the pre-arcing. Some studies were carried out under *AC* supply (Gibson, 1941; Leach et al., 1973; Wilkins and McEwan, 1975; Wheeler, 1976; Bussière et al., 2008), others under *DC* supply (Gibson, 1941; Wheeler, 1976). The main tasks of these investigations were to understand in which manner electrical characteristics of a circuit network play a role in the fuse performance and to link the electrical energy dissipation of the fuse to the prediction of pre-arcing times.

In this work the pre-arcing behaviour of HBC fuses is analysed in the case of realistic industrial test conditions in terms of some characteristics of the prospective fault current under *AC* supply. This is done by varying the closing angle and the power factor values founded in industrial HBC fuses. As the closing angle and the power factor values decide respectively on the instant of appearance and on the magnitude of the fault, the pre-arcing time is strongly dependent on their values. Simulations and measurements are carried out for closing angle values varying in a wide range as in industrial operation and for two power factor values corresponding to the two typical cases namely the inductive case and the resistive case. In section 2, the experimental test is presented, following by the geometry of the fused element used in simulation and in experiments and the mathematical model. The simulated and experimental results are exhibited in section 3 and discussion is drawn on in section 4. Conclusion is done after.

2. EXPERIMENTAL SET UP AND THERMO-ELECTRICAL MODEL

2.1 Experimental Test

The experimental test device built from a 100kVA true single-phase transformer has been designed to reproduce the whole fuse operation in fault conditions similar to the industrial test conditions. The experimental device and the test operation have been described in previous works by Bussière *et al.* (2008) and Memiaghe *et al.* (2008). The main electrical parameters of the measurements are recalled hereafter.

The first step before a fuse operation is to set the closing angle (defined as the phase angle of the beginning of the fault current or prospective current i_p once the supplied voltage v_s is applied to the fuse) and the power factor. The closing angle θ is expressed in time units (Fig. 1) by:

$$\Delta t(ms) = \frac{\theta(^\circ)}{18} \tag{1}$$

The power factor is deduced from the following formula:

$$\cos\varphi = \frac{R}{\sqrt{R^2 + L^2\omega^2}} \tag{2}$$

where R and L are respectively the resistive load and the inductive load, ω is the pulsation calculated at 50 Hz.

The second step is to set the prospective current which stands for the electric fault. This fault is calculated as:

$$i_p(t) = \frac{\hat{V}}{\sqrt{(R^2 + L^2\omega^2)}} \times \left(\sin(\omega t + \theta - \varphi) - \sin(\theta - \varphi) \times e^{-\frac{R}{L}t}\right) \tag{3}$$

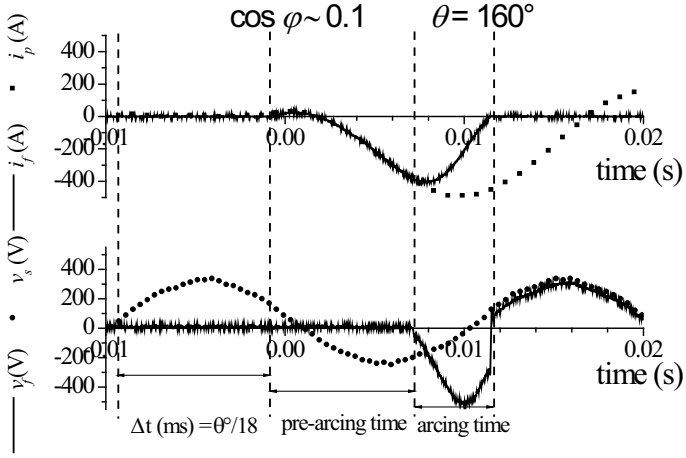

Fig. 1: Characteristic curves of fuse breaking under AC supply: fuse voltage v_f, supply voltage v_s, fuse current $i_{f,}$ prospective current i_p.

where $\hat{V}$ is the peak value of the supply voltage at 50 Hz and t is the time. It is important to notice that according to international standards (IEC, 2005), the current passing through the fuse is equated to the prospective fault current during the whole pre-arcing stage. So current $i_p(t)$, current $i_f(t)$ and current $i(t)$ stand for the same fuse current.

The Joule energy W_J dissipated in the fuse-link due to the passage of the fault current during the pre-arcing time (duration t_p) is given by:

$$W_J = \int_0^{t_p} R_f(t) \times i^2(t) dt, \tag{4}$$

where R_f is the fuse resistance.

2.2 Fuse Element Geometry

Simulations and experiments have been carried out for a fuse-link with circular reduced section shape of $l' \times e$ = 0.5×0.105 mm^2. The fuse-link length is $L = 66$ mm and its cross-section area is $l \times e$ = 1×0.105 mm^2. For the experiments, the fuse element (designed to reproduce elementary phenomenon occurring in industrial fuses) is introduced in the circuit network by means of an experimental fuse cell as depicted in Bussière et al. (2008).

2.3 Thermo-Electrical Model

The mathematical model dealt with thermal effect and electrical effect problem. This problem is based on the heat transfer equation with conduction as the main heat loss term and Joule heating as the main source term. The thermo-electrical problem is usually written as:

$$\frac{\partial H}{\partial t} - \nabla.(k_{Ag} \nabla T) = \frac{|\mathbf{J}|^2}{\sigma_{Ag}}, \tag{5}$$

where H represents the enthalpy of the silver fuse-link, k_{Ag} and σ_{Ag} are respectively the thermal and the electrical conductivity of silver (both depending on enthalpy) and J is the current density vector. The current density is obtained from the Laplace equation and the Ohm's law which are governed by:

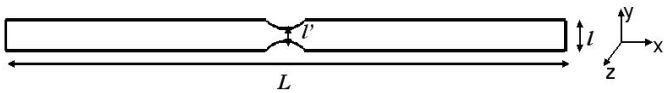

Fig. 2: Fuse element geometry used in simulations and experiments.

$$\begin{aligned} &\nabla.(\sigma_{Ag}\nabla V) = 0, \\ &\mathbf{E} = -\nabla V, \\ &\mathbf{J} = \sigma_{Ag}\mathbf{E}. \end{aligned} \tag{6}$$

V is the potential and *E* is the electric field vector. To solve numerically the system [Eqs. (5) and (6)], the finite elements *method* is used for space discretization and a *Chernoff scheme* is used for time integration. Details of the mathematical model and the numerical method are reported in Rochette *et al.* (2007).

3. RESULTS

We present results of prospective current, supply voltage and the temperature evolutions during the pre-arcing stage under given power factor and closing angle.

3.1 Closing Angle of θ=12.1 under Inductive Power Factor cos φ ∼ 0.1

Figure 3 presents the simulated and the experimental waveforms of the prospective current i_p and the supply voltage v_s during the pre-arcing time in the case of a power factor fixed at cosφ ∼ 0.1 and a closing angle of θ=12.1°. In simulation the pre-arcing time is obtained once the whole latent heat of vaporization is provided. This simulated pre-arcing time is 6.96 ms and the pre-arcing time measured is 6.13 ms (the relative discrepancy is about 12%).

In Figure 4 is exhibited the simulated fuse-link temperature rise and the Joule energy W_J dissipated in the fuse during the pre-arcing time. W_J at the end of pre-arcing time is 10.80 J. We give also the temperature T_{eq} corresponding to the pre-arcing time measured. The pre-arcing time measured is reported on the

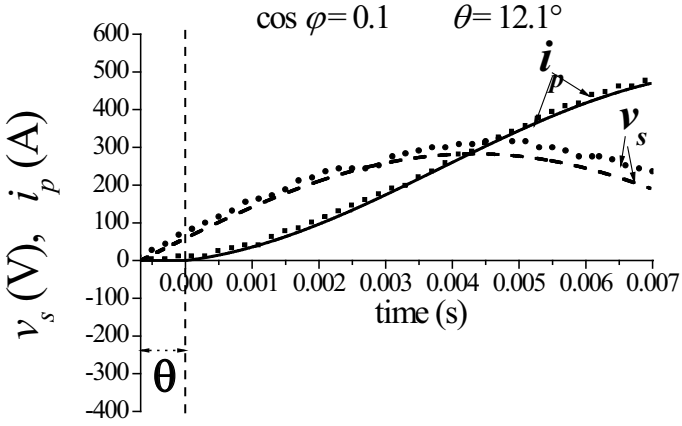

Fig. 3: Simulated (line) and measured (full squares) prospective fault i_p and simulated (dash) and measured (full circles) supply voltage v_s during the pre-arcing time.

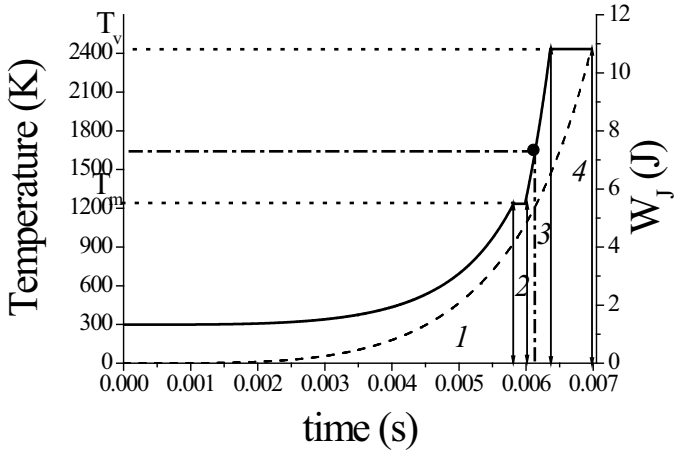

Fig. 4: Simulation of the temperature evolution (continuous line) with the experimental value of t_p (solid circle) and W_J (dashed line) in the fuse during the pre-arcing time.

simulated temperature curve to estimate a temperature related to the pre-arcing time obtained in experiments. This temperature is $T_{eq} = 1656$ K. The temperature evolution exhibits four main stages. During the first stage 1 W_J is devoted to rise the temperature of the fuse element from its initial temperature (300 K) up to its melting temperature (T_m). During the second stage 2 W_J is involved in the solid to liquid state change by means of the latent heat of fusion. This state change participates in a considerable variation of the fuse-link resistivity [the ratio of the liquid resistivity to the solid resistivity for silver is about $\sim$2.1 (Matula, 1979)] and consequently the liquid resistivity leads to a fast temperature rise up to the vaporization temperature (T_v) as it can be seen in the third stage 3. In the fourth stage 4, the constant fuse-link temperature observed is due to the latent heat of vaporization which requires a significant energy [about 10 times related to the energy necessary for the latent heat of fusion (Bahrin, 1995)] is necessary for the whole liquid-vapour state change.

3.2 Closing Angle of θ=90° Under Inductive Power Factor cos $\varphi \sim$ 0.1

Figure 5 gives the waveforms of i_p and v_s during the pre-arcing time in the case of cos$\varphi \sim$ 0.1 and for θ=90° for simulation and experiments. Simulation and experiments give respectively pre-arcing times of 14.16 ms and 12.68 ms (the relative discrepancy is about 10%). The limitation of the fault current occurs in the second half-wave and the pre-arcing time is in both cases much longer compared to the previous ones obtained for θ = 12.1°.

This result is interesting because the fault current has two main characteristics that the fuse tends to reduce as better as possible: the duration and the magnitude.

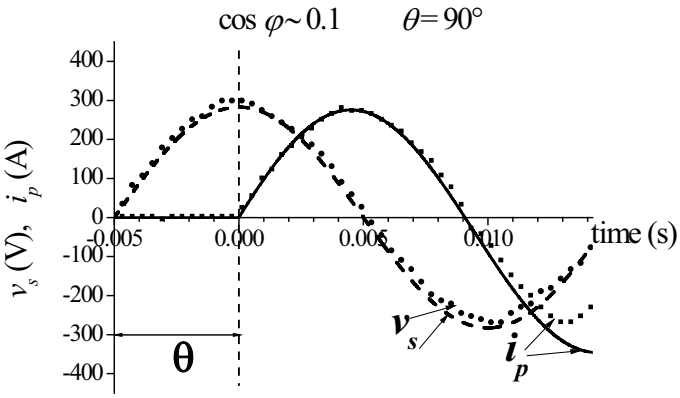

Fig. 5: Simulated (line) and measured (full squares) i_p and simulated (dash) and measured (full circles) v_s during the pre-arcing time.

The duration and the magnitude of the fault are expressed in a parameter which characterizes all fuse performances, the *Joule integral* ($I^2t = \int_0^{tp} i^2(t)dt$). These two characteristics are significant in the case of θ = 90° because in this case the Joule energy is maximum.

This is illustrated in Fig. 6 which exhibits the temperature and the W_J plotted as a function of the time. W_J at the end of pre-arcing is 16.45 J and is 65% higher than that of θ=12.1°. An estimate of temperature corresponding to the pre-arcing time measured is $T_{eq} = 1766$ K.

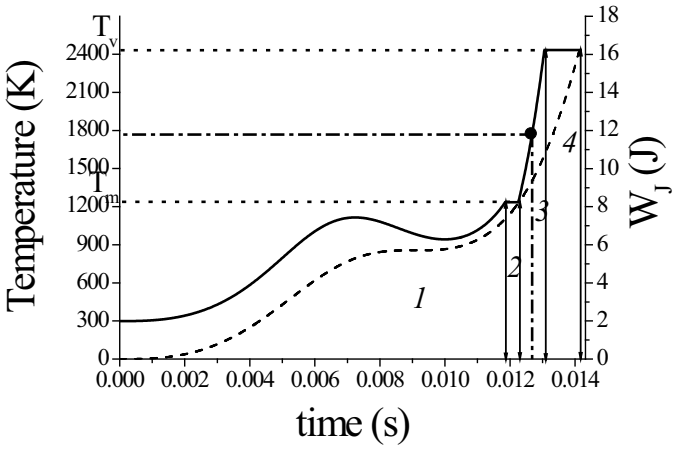

Fig. 6: Simulation of the temperature evolution (continuous line) with the experimental value of t_p (solid circle) and W_J (dashed line) in the fuse during the pre-arcing time.

The curve of Fig. 6 presents the four main evolutions as it was seen in Fig. 4. In stage 1 of Fig. 6 the fuse temperature increases and decreases due to the current waveform. This means that once the current falls down and reaches zero, the Joule heating also decreases: heat transfer by conduction from the hottest points of the fuse element to the remainder fuse appears and consequently the temperature decreases.

3.3 Closing Angle of θ=160° under Inductive Power Factor cos φ ∼0.1

In Fig. 7 we show the prospective current and the supplied voltage waveforms for a closing angle of 160° both for simulations and experiments in the case of cosφ∼ 0.1. From the appearance up to the passage to zero in the first half-cycle, the fault current could not really damages the fuse due to the fact that the magnitude of the fault is not significant ($i_{p,peak}$ ∼19 A) during this period.

The current limitation occurs in the second half-wave and the pre-arcing time is 8.85 ms for simulations and 7.90 ms for experiments. The relative discrepancy is about 11%.

Figure 8 shows the temperature and the Joule energy histories during the pre-arcing time. W_J at the end of pre-arcing time is 10.67 J. From the energy point of view the characteristics of Fig. 8 are very similar to those obtained in the case of θ=12.1° of which W_J is 10.80 J. The duration of the fault current in the first half-cycle (about 2 ms) for θ=160° explains the difference between pre-arcing times values. Figure 8 also gives the estimated temperature corresponding to the pre-arcing time obtained in experiments which is $T_{eq} = 1300$ K.

3.4 Closing Angle of θ=6.7° under Resistive Power Factor cos φ ∼ 0.9

Figure 9 presents the waveforms of the prospective current i_p and the supply voltage v_s during the pre-arcing time in the case of cos φ ∼ 0.9 and for θ=6.7°

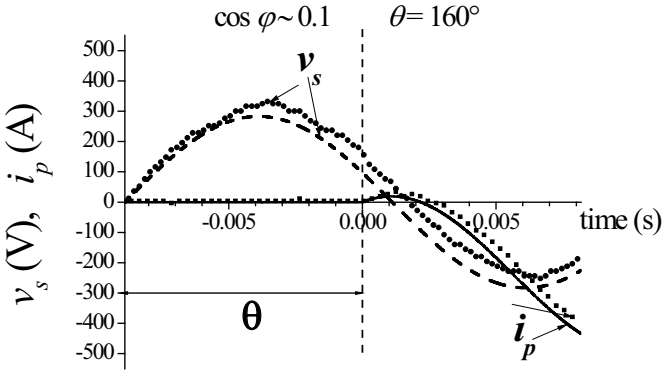

Fig. 7: Simulated (line) and measured (full squares) i_p and simulated (dash) and measured (full circles) v_s during the pre-arcing time.

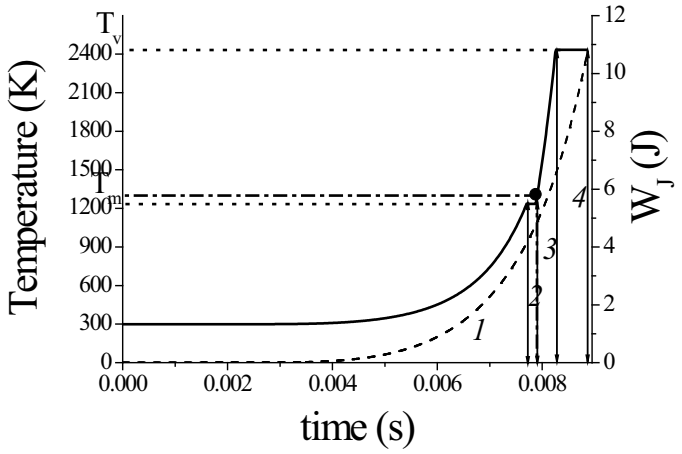

Fig. 8: Simulation of the temperature evolution (continuous line) with the experimental value of t_p (solid circle) and W_J (dashed line) in the fuse during the pre-arcing time.

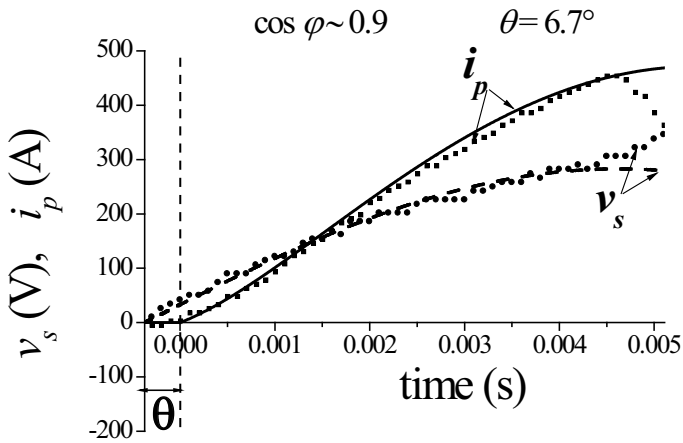

Fig. 9: Figure 9: Simulated (line) and measured (full squares) prospective current i_p and simulated (dash) and measured (full circles) v_s during the pre-arcing time.

for simulations and experiments. Simulations and experiments give respectively pre-arcing times of 5.11 ms and 4.67 ms (the relative discrepancy is about 9%). Compared to the simulated pre-arcing time obtained in the case of cos $\varphi \sim 0.1$ for θ=12.1°, the pre-arcing time obtained from simulations in this case, is shorter and the relative difference represents about 27%. The same observation is done when looking to the measured pre-arcing times for which the difference is about 24%. The value of the closing angle is not the main reason to explain this difference; but the

magnitude of the fault current which is higher in the resistive case compared to the inductive one.

Figure 10 shows the temperature and the dissipated energy histories during the pre-arcing time. W_J at the end of pre-arcing time is 10.30 J is quite equal than to that obtained in the case of cos$\varphi \sim 0.1$ for θ=12.1°. Figure 8 also gives the estimated temperature corresponding to the pre-arcing time obtained in experiments which given by $T_{eq} = 2433$ K.

3.5 Closing Angle of θ=90° under Resistive Power Factor cos $\varphi \sim$ 0.9

Figure 11 presents the waveforms of the prospective current i_p and the supply voltage v_s during the pre-arcing time in the case of cos $\varphi \sim$ 0.9 and for θ=90° for simulation and experiments. Simulations and experiments give respectively pre-arcing times of 4.77 ms and 2.53 ms (the relative discrepancy is about 47%).

Figure 12 shows the temperature and the Joule energy histories during the pre-arcing time. W_J at the end of pre-arcing time is 10.48 J and the estimated temperature corresponding to the pre-arcing time obtained in experiments which correspond to T_{eq} = 1235 K.

3.6 Closing Angle of θ=160° under Resistive Power Factor cos $\varphi \sim$ 0.9

Figure 13 presents the waveforms of the prospective current i_p and the supply voltage v_s during the pre-arcing time in the case of cos $\varphi \sim$ 0.9 and for θ=160° for simulation and experiments. Simulations and experiments give respectively pre-arcing times of 6.60 ms and 5.64 ms (the relative discrepancy is about 15%).

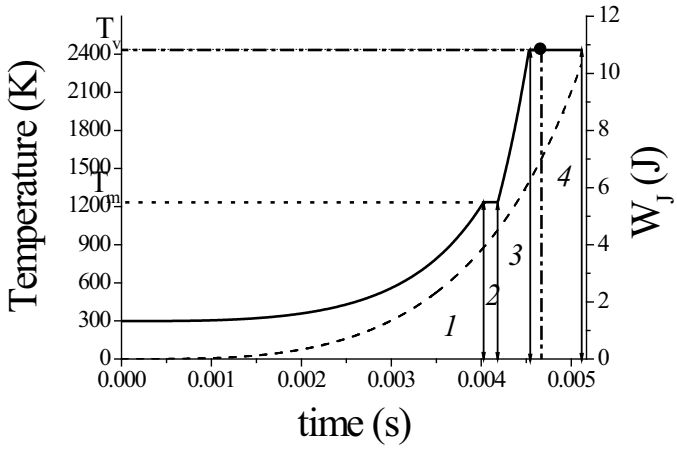

Fig. 10: Simulation of the temperature evolution (continuous line) with the experimental value of t_p (solid circle) and W_J (dashed line) in the fuse during the pre-arcing time.

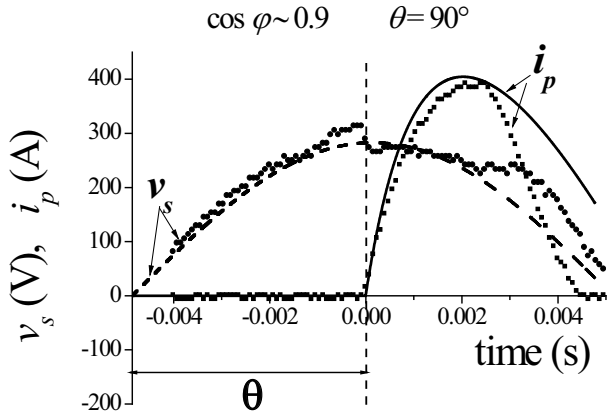

Fig. 11: Simulated (line) and measured (full squares) i_p and simulated (dash) and measured (full circles) v_s during the pre-arcing time.

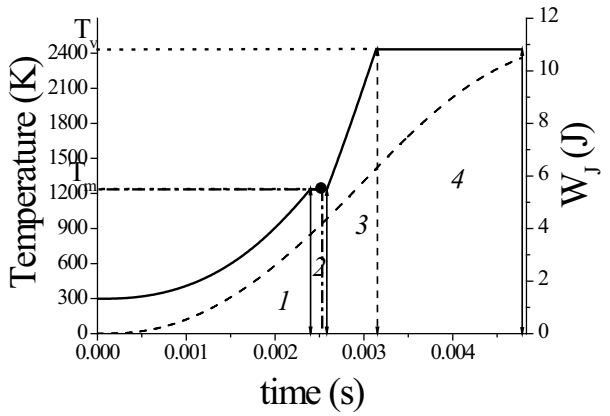

Fig. 12: Simulation of the temperature evolution (continuous line) with the experimental value of t_p (solid circle) and W_J (dashed line) in the fuse during the pre-arcing time.

Figure 14 shows the temperature and the Joule energy histories during the pre-arcing time. W_J at the end of pre-arcing time is 10.37 J and the estimated temperature corresponding to the pre-arcing time obtained in experiments which correspond to T_{eq} = 1235 K.

3.7 Summary of the Results

In Table 1, we recall the different pre-arcing time values obtained from simulation and experiment with the discrepancies observed. In Table 2 a reminder of the corresponding temperature of measured pre-arcing time is given.

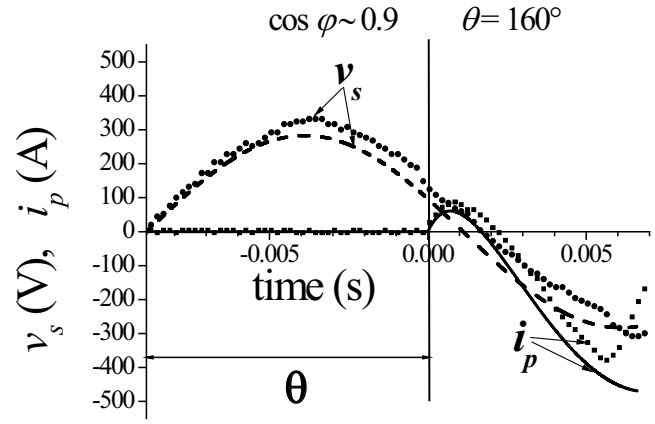

Fig. 13: Simulated (line) and measured (full squares) i_p and the simulated (dash) and measured (full circles) v_s during the pre-arcing time.

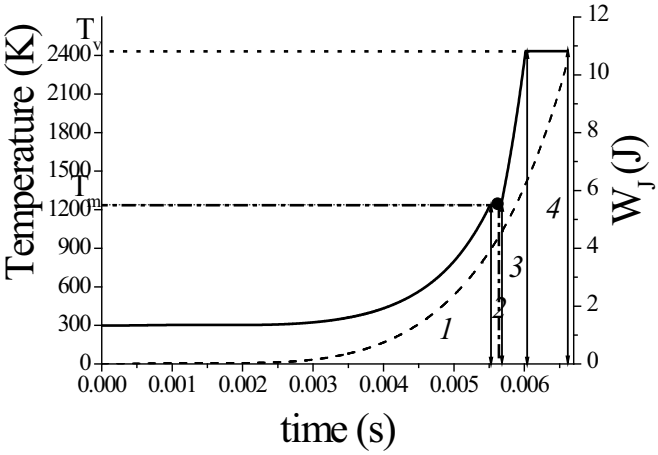

Fig. 14: Simulation of the temperature evolution (continuous line) with the experimental value of t_p (solid circle) and W_J (dashed line) in the fuse during the pre-arcing time.

4. DISCUSSION

Table 3 gives the simulated pre-arcing times and the W_J values, during the four stages previously quoted for the three closing angles under cos φ ∼ 0.1. The distribution of the Joule energies is quite similar during each corresponding stage for the different closing angles. Indeed, except in the stage 1 and in stage 4 of θ=90° for which the energies represent respectively ∼45% and ∼35% of the whole dissipated

Table 1: Relative discrepancy between simulated and experimental pre-arcing times.

	Simulations	Experiments	Relative discrepancy (%)
$\theta(^\circ)$	t_p (ms) – cos $\varphi \sim 0.1$		
12	6.96	6.13	12
90	14.16	12.68	10
160	8.85	7.90	11
	Simulations	Experiments	Relative discrepancy (%)
$\theta(^\circ)$	t_p (ms) – cos $\varphi \sim 0.9$		
6	5.11	4.67	9
90	4.77	2.53	47
160	6.60	5.64	15

Table 2: Experimental pre-arcing times and equivalent temperature for the two power factors.

	cos $\varphi \sim 0.1$		cos $\varphi \sim 0.9$	
$\theta(^\circ)$	t_p (ms)	T_{eq} (K)	t_p (ms)	T_{eq} (K)
6.7 - 12.1	6.13	1656	4.67	2433
90	12.68	1766	2.53	1235
160	7.90	1300	6.64	1235

Table 3: Simulated pre-arcing times and W_J during the four stages under cos $\varphi \sim 0.1$.

cos $\varphi \sim 0.1$		W_J (J)			
$\theta(^\circ)$	Pre-arcing time (ms)	stage 1	stage 2	stage 3	stage 4
12	6.96	4.14	0.62	1.81	4.23
90	14.16	7.39	0.81	2.52	5.73
160	8.85	4.17	0.62	1.77	4.11

energy; the percentages of the dissipated energies for all the relevant cases are quite similar:

- In stage 1 the percentage is $\sim$38% for θ=12° and $\sim$39% for θ=160°,
- In stage 2 the percentage is $\sim$6% for θ=12° and θ=160°, and $\sim$5% for θ=90°,
- In stage 3 the percentage is $\sim$17% for θ=12° and θ=160°, 15% for θ=90°,
- In stage 4 the percentage is $\sim$39% for θ=12° and θ=160°.

The percentages of the dissipated energies for all the relevant cases are quite similar:

- In stage 1 the percentage is ∼38% for θ=6° and θ= 160°, ∼36% for θ=90°,
- In stage 2 the percentage is ∼6% for θ=6°, θ=90° and θ=160°,
- In stage 3 the percentage is ∼17% for θ=6° andθ=160°, 19% for θ=90°,
- In stage 4 the percentage is ∼39% for θ=6°, 40% for θ=90° and θ=160°.

Table 4 gives the simulated pre-arcing times and the dissipated energy values, during the four stages previously quoted for the three closing angles under $\cos\varphi \sim 0.9$.

Table 4: Relative discrepancy between simulated and experimental pre-arcing times.

$\cos\varphi \sim 0.9$		W_J (J)			
θ(°)	Pre-arcing time (ms)	Stage1	Stage 2	Stage 3	Stage 4
6	5.11	3.92	0.58	1.75	4.05
90	4.77	3.78	0.58	1.98	4.14
160	6.60	3.93	0.58	1.72	4.14

In simulation and in experiments it is observed that the pre-arcing stage is much longer in the inductive case compared to the resistive case. This observation is made for all the relevant closing angles due to the fact that the prospective current is most important in the resistive case compare to the inductive one.

Both under inductive and resistive case, pre-arcing times obtained by experiments are lower than those obtained in simulations; two main reasons could explain that.

First, previous works (Bussière et al., 2008; Rochette et al., 2007) attributed the uncertainties between simulation and experiment to irregularity found in the notch shape and to the fact that sometimes one or some silica grains are unfortunately introduced in the center of the fuse. Second, the discrepancies observed between simulations and experiments are mainly due the physical state at which the fuse link should disrupt. According to us, mechanical stress must be taken into account and these forces are also responsible of the rupturing of the fuse. Indeed the equivalent temperature value corresponding to measurements, pre-arcing times is observed in most cases at time t_p corresponding to $t_{Tm} < t_p < t_{Tvap}$.

5. CONCLUSION

In this study was investigated the simulated and measurement response of a HBC fuse submitted to typical fault currents under *AC* supply. Two key parameters such as the closing angle and the power factor were used to characterize electrical fault test conditions close to the industrial test conditions and required by international

standards. The prospective fault was founded to be dependent on such parameters and consequently the pre-arcing time. A resistive power factor gives fault current higher than the inductive power factor, and then the pre-arcing time was founded to be longer in the inductive case compared to the pre-arcing time in the resistive case. The role played by the closing angle in the pre-arcing duration was analyzed and we found that typical closing angle values involve maximum dissipated energy which is interesting for Joule integral prediction. This is very important for industrialist and for standard organizations in prediction of "the current/heat integral" curves. Good agreements between simulations and experiments were founded by the fact that the mathematical model reproduces easily tested conditions close to industrials. Some discrepancies were observed which could be explained by the fact that the enthalpy dependence of the thermal conductivity found in the literature (calculated and measured) is given up to the temperature of 1900 K, above all data has been fitted. We also did not take into account the volume expansion (Cagran et al., 2006) of density calculation after melting.

The equivalent temperature related to the measured pre-arcing time supposed that disrupting of the fuse is not only due the thermal process. This supposed that other contribution possibly due to mechanical stress is combined to the thermal stress to cause the rupturing of the fuse element before the end of the whole latent heat.

REFERENCES

I.Bahrin, Thermochemical Data of Pure Substances, 3rd ed. in collaboration with G. Platzki, vol. 1. Ag-Kr and vol. 2. La-Zr, VCH Weinheim, Federal Republic of Germany, New York, 1995.

W.Bussière, D.Rochette, G.Velleaud, T.Latchimy, J.L.Gelet, F.Gentils, J.C.Perez-Quesada, T.Rambaud, and P.André, Experimental study of HBC fuses working at short and medium pre-arcing times, *J. Phys. D: Applied Physics*, 2008, 41, p. 195210.

C.Cagran, B.Wilthan, and G.Pottlacher, Enthalpy, heat of fusion and specific electrical resistivity of pure silver, pure copper and the binary Ag-28Cu Alloy, *Thermochimica Acta*, 2006, 445, pp. 104–110.

J.W.Gibson, The high-rupturing-capacity cartridge fuse, with special reference to short-circuit performance, *Journal of the IEE*, 1941, 88, pp. 2–24.

IEC, 60282-1 High Voltage fuses—Part 1: Current-Limiting Fuses, November 1, 2005.

J.G.Leach, P.G.Newberry, and A.Wright, Analysis of high-rupturing-capacity fuselink prearcing phenomena by a finite-difference method, *Proceedings of the IEE*, 1973, 120(9), pp. 987–993.

R.A.Matula, Electrical Resistivity of Copper, *Gold, Palladium, and Silver JPCRD*, 1979, 8(4), pp. 1147–1298.

S.Memiaghe, W.Bussière, D.Rochette, R.Touzani, and P.André, pre-arcing times in HBC fuses for high fault currents. Comparison between simulation and experiment, *High. Temp. Mater. and Proc*., 2008, 12(3/4), pp. 345–364.

D.Rochette, R.Touzani, and W.Bussière, Numerical study of the short pre-arcing time in high breaking capacity fuses via an enthalpy formulation, *J. Phys. D: Applied Physics*, 2007, 40, pp. 4544–4551.

Y.S.Touloukian, R.W.Powell, and C.Y.Ho, Thermal conductivity— metallic elements and alloys, Vol. 1 of Thermophysical properties of Matter – the TPRC Data Series, ed. IFI/Plenum New York Washington, 1970.

C.B.Wheeler, Optimum conditions for electrical testing fuses. I Maximization of the prearcing energy, *J. Phys. D: Applied Physics*, 1976, 9, pp. 1809–1816.

R.Wilkins and P.M.McEwan, A.C. short-circuit performance of notched fuse elements, *Proceedings of the IEE*, 1975, 122(3), pp. 289–292.

A.Wright and P.G.Newberry, Electric Fuses, IEE Power & Energy Series, vol. 49, 3^{rd} edn, London, 2001.

HIGH TEMPERATURE MATERIAL PROCESSES **14** (2010) 271-284

CATHODE SPOT EMERGENCE ON COPPER AND CHROMIUM ALLOY USED IN VACUUM BREAKERS

L. André[1], **A. M'hammed**[1], **C. Stéphane**[2]

[1]*Laboratoire Arc Electrique et Plasmas Thermiques—Clermont Université—CNRS, Université Blaise Pascal, Bât. Physique 5—24 Avenue des Landais—F63170 AUBIERE Cedex*
[2]*Laboratoire de Mathématiques pour l'Industrie et la Physique—CNRS—Université Paul Sabatier Toulouse 3—118 route de Narbonne—F31062 TOULOUSE Cedex*

ABSTRACT: For copper and chromium, used in alloy component electrodes of vacuum circuit breakers, the cathode spots are initiated on micron meter spikes above the surface of the electrode, they are considered as cylinders with a height equivalent. After spraying of these peaks the cathode spot reaches the surface of the electrode on which it will expand according to a proposed model. The two studied materials have quite different thermophysical properties, but they lead to comparable results. In both cases the erosion of cylindrical spikes is due to the flow of energy provided by the cathode spot, the mechanism is different from those found for the molten bridge or for fuses where the Joule effect is the only factor to take into account.

KEY WORDS: copper and chromium alloy, vacuum breakers, erosion, cathode spot

1. INTRODUCTION

This study is connected with copper chromium alloys used in vacuum circuit breakers where for currents below 40 kA the anode is not in its contracted form and does not interact with the electrode, only the life time limited spots cathode appear and disappear on the electrode surface and modify it. The structure of the alloy is the result of the inclusion of chromium aggregates in the copper matrix; the cathode spots will then be formed independently on both materials and have different features. The analysis of the behaviour of two materials, studied separately, will assess differences in response to energy supplied by the cathode spots to see if it is possible to consider a macroscopic material with mean physical properties. To achieve this goal it is necessary to analyze the development of cathode spot since its creation to its extinction.

Cathode spots on the contacts of vacuum circuit breakers have a life time limited to a few tens of nanoseconds Beilis et al. (1997), to ensure the passage of current

during the phase when the arc is present, they must have continual renewal. They appear on the end tips of a few micron meters in height and one micron meter in diameter, and then they expand on the flat part of the material when the tip has disappeared through erosion.

In the proposed model these tips are treated as cylinders; this is not inconsistent with the assumptions made by Mesyats (2000), because the cylinder is, before the creation of the cathode spot, surmounted by a conical part that is destroyed very quickly by creation of an Ecton. The transition will be done by increasing the radius of the base of cathode spot. The final size of the spot should be on the order of magnitude of those given by several authors Prock (1986), Klien et al. (1994), therefore the working of the cathode spot should not be disturbed when this transition occur; if the conditions imposed on certain physical parameters are not satisfied it disappears.

After presenting the basic equations governing the interface between the base of the arc and the surface of support material, giving the flow of energy transmitted to the latter, the numerical solution is briefly presented. Applying this model to a metal cylinder shows the linear erosion and precludes the formation of a molten bridge. The complete simulation including the cylinder and the electrode gives results on the comparative erosion of both materials.

2. BASIC THEORY OF CATHODE SPOT, SIMULATION METHOD

2.1 The Cathode Spot

Figure 1 shows the model of the most successful spot currently Beilis (1995) with associated zones. The expansion zone provides the transition between the last part

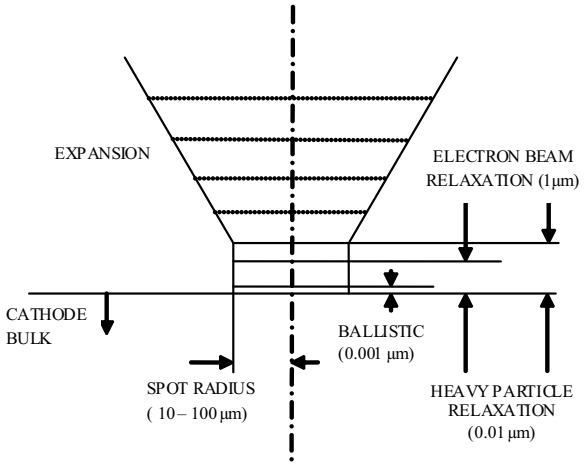

Fig. 1: Schematic diagram of cathode spot zones Beilis (1995).

of the cathode spot and the arc column, it presents large variations in particle temperature and density, it is an area little studied. In the area of electron relaxation, the flow toward the column undergoes a speed reduction resulting from collisions with ions and atoms coming from the electrode. This area of electron relaxation includes the zone of heavy particles relaxation where the vapours emitted by the metal surface are progressively ionized, creating a zone of positive space charge at the edge of the ballistic zone which leads to an intense electric field (about 8×10^9 Vm^{-1} Beilis et al. (1997)), this field is determined by integrating the Poisson equation on the contraction zone. This electric field and high temperature of the surface of the material cause the emission of electrons. The electronic current density J is obtained by the classical equation of Murphy and Good (1956) resulting from solving the Schrödinger equation, knowing the values of surface temperature and electric field J values can be determined. For further calculations presented, the values of J are obtained simply by assuming that the radius of the cathode spot is either assigned (cylinder case) or given by different authors when the spot develops on a large flat electrode. In the article presented the concern is with the change in value of the radius of the spot when the cylinder is completely eroded and that the spot must occupy an area compatible with the values of J for a flat surface larger.

In the ballistic zone particles undergo acceleration resulting from the action of electric field, without any interaction between them. This brief description of the base of the cathode spot shows the need for the presence of metal ions bombardment of the electrode providing the necessary energy, without their presence, i.e. without vaporization of the electrode cathode, the spot does not produce electrons and disappears. It should be noted that another cause of the shutdown of the electronic emission is the collapse of the electric field for geometrical reasons, especially when the surface of the electrode is concave as a result of erosion. Many equations are associated with this model, they describe the flow of particles into different zones. To solve the problem, just write the equation giving the flow of energy P_{ions} arriving on the surface of the electrode, corresponding to the return flow of ions on the electrode Cobine et al. (1955):

$$P_{ions} = (1 - s) \times (V_c + V_i - V_s) \times J \tag{1}$$

$s$is defined as the electronic fraction, the quantity $(1 - s)$ represents the fraction of total current resulting from ion flow, V_c defines the cathode fall, V_i the ionization potential and V_s the potential corresponding to the work function for electrons and J is the current density at the electrode surface. J may vary radially and temporally, for calculations that follow this quantity is considered constant, distributions using lightly parabolic or Gaussian low does not change the conclusions of this study. Table 1 gives the values for these parameters for copper and chromium.

The flow of energy given by Eq. (1) will be dissipated at the electrode in three forms of unequal values Lee (1960), Lee et al. (1961):

$$P_{ions} = P_{thermal} + P_{ec} + P_{rs} \tag{2}$$

Table 1: Associated potentials to copper and chromium.

Potentiel	Copper	Chrome	Références
Cathode fall V_c /V	15.05	17.05	Strachan (1976) Grakov (1967) Beilis (1969)
Ionization V_i /V	7.73	6.77	Lide (2001)
Work function V_s /V	4.8	4.5	Lide (2001)

the first term corresponds to the flow of energy transferred as heat, the second represents the flow of energy for electrons to exit the metal surface and the third is the flow of energy radiated by the spot. Only the $P_{thermal}$ flux is dominant, hence the relation:

$$P_{thermal} = P_{ions} \tag{3}$$

2.2 Numerical Resolution

The evolution as a function of time of the electrode structure that receives the heat flux given by the Eq. (3) is obtained by solving the equation of heat in its enthalpy form Abbaoui et al. (2005):

$$\frac{\partial H}{\partial t} = div(k\overrightarrow{\nabla} T) + Source \tag{4}$$

H is the enthalpy of the material at the considered point, k the thermal conductivity, T the temperature and $Source$ represents the energy created in the material by Joule effect. The enthalpy varies with temperature (Fig. 2), the material turns into liquid or vapour when the values of enthalpies of liquefaction and vaporization are achieved. The calculation program is to solve Eq. (4) for all points of the mesh electrode, it gives enthalpy values, temperature and phase of each point is given by reference

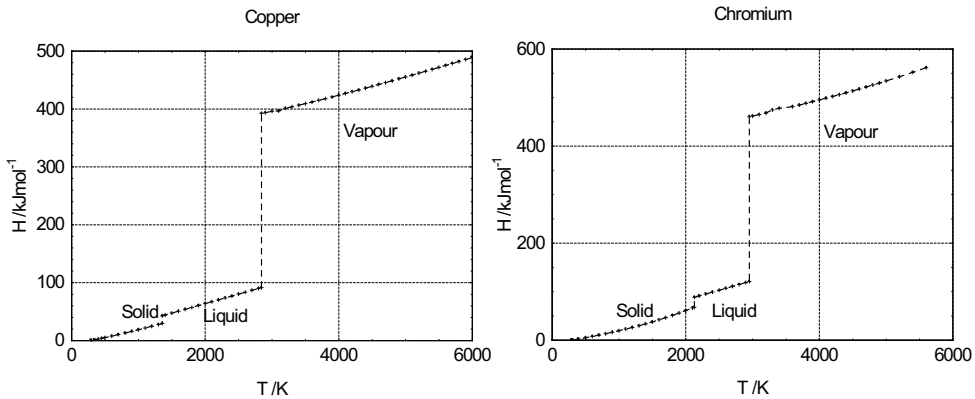

Fig. 2: Enthalpies for copper and chromium Chase (1998).

to the curves in Fig. 2. After transformation, and where the term $Source$ is zero, Eq. (4), showing no analytical solution is solved in an approximate way by the finite element method Rossignol et al. (2000).

If Ω_t is the integration area, this area varies over time, and J_m the set of indices defined on the field, the solution is the function:

$$H_h = \sum_{i \in J_m} H_i(t)\phi_i \tag{5}$$

The temporal discretization is obtained by considering a division of defining regular intervals τ of time space, current time is represented by $t^m = m\tau$, the objective is to determine the function:

$$H_h^{m+1} = \sum\nolimits_{i \in J_m} H_{i,j}^{m+1}\phi_i \tag{6}$$

the function ϕ is a regular function with real values needed to discretize the domain.

The removal of areas that have reached the enthalpy of vaporization requires solving a Stefan problem with removal, in case of an axisymmetric geometry, the solution is the following linear system:

$$\int_{J_m} \frac{H_h^{m+1} - H_h^m}{\tau}\phi r dr dz + \int_{J_m} a(H_h^m)\nabla d H_h^{m+1}\nabla\phi r dr dz = \int_{J_m} P_{thermal}\phi_{J_m} r dr dz \tag{7}$$

$a(H_h^m)$ is the spatial derivative of the function β defined by:

$$\beta = \int_{T_0}^{T} k(u)du \tag{8}$$

the thermal conductivity k changes with material temperature T.

The mesh in two dimensions defined fields K, objects of solving Eq. (7) for an axisymmetric geometry, the field K after evolution can be deleted, so there is evaporation, when the following condition is satisfied:

$$\int_K H dr dz > \int_K H_{vap} r dr dz \tag{9}$$

H_{vap} represents the material vaporization enthalpy.

The boundary conditions are:

- on the surface corresponding to the cathode spot, the flow directed towards the material is defined by $P_{thermal}$,
- for all other surfaces of the cylinder there is no energy exchange, this condition is justified by the short duration of the phenomenon where the surface of the cylinder are considered to set the temperature imposed at $t = 0$ (general case).

3. STUDY OF THE EFFECT OF CATHODE ARC ROOT ON A CYLINDER

3.1 Cathode Spot on Metal Tips

The works of Mesyats (2000) on the formation of cathode spots in vacuum show that they appear at the top of metal spikes arranged on the surface of the contact and measuring about 1 μm height and with a diameter varying around this value. For a copper electrode, the author states that the diameter of the spot in this case is 1.4 μm, and carries a current of 10 A. It is correct to assume that just after the birth of the cathode spot, the tip may be treated as a cylinder. Two physical phenomena are added to transmit energy to the cylinder, the flow of ions and the Joule effect.

3.2 Comparison of the Effects Between Cathode Flow and Joule Effect

Figure 3 shows the ion flux and a 10 A current through a cylinder of 1.4 μm in diameter and 6 μm height, this value was chosen to meet the boundary conditions. The energy flows received, given the Eqs. (1) and (3) and data from Table 1, are respectively 2.34×10^{13} W/m^2 for copper and 2.51×10^{13} W/m^2 for chromium. In this case the lateral surface of the cylinder located at the same height z that the surface receiving the energy flow reaches in a very short time the same temperature, as the heat exchange with the environment (here the vacuum) is negligible, the evolution of thermal phenomena is ultimately comparable to that of a 1D geometry. The time step chosen for this calculation is 0.1 ns and the step space is 0.02 μm.

The removal is homogeneous on the upper surface of the cylinder, the thickness of liquid remains constant after an evolutionary phase that lasts two or three nanoseconds, the average values are given in Table 2.

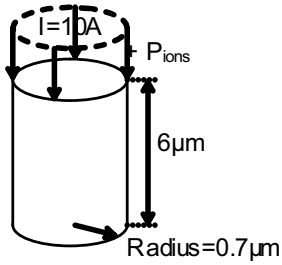

Fig. 3: The cylinder used to simulate Joule and thermal effects.

Table 2: Mean liquid thickness during arc root on the cylinder.

	Copper	Chromium
With Joule effect	0.283 μm	0.178 μm
Without Joule effect	0.251 μm	0.163 μm

Figure 4 gives the volumes of solid material that has changed phase, with and without the presence of the Joule effect.

The Joule effect gives by an increase in the thickness of liquid 12% for copper and 9% for chromium. The removal speed determined from the curves of Fig. 4 is, respectively, 320 m/s without Joule effect, for the copper cylinder and 310 m/s for the chromium, these values increase only of 3% when the Joule effect is taken into account. Given the simplifying assumptions chosen for the study of the effect of the cathode spot on an electrode, it is not necessary to take into account the Joule effect in the material.

The result shows that the tip (here cylindrical) does not explode like in the case of the bridge where the melted spot is not present but evaporates at a constant speed, the points with an average height of 1 μm they will put less of 3 ns to disappear.

4. FLAT ELECTRODE SURMOUNTED BY A CYLINDER OF LITTLE DIMENSIONS

4.1 The Geometry Used

Figure 5 shows the arrangement used for the calculations, the cylinder representing the tip has a radius equal to $r = 0.7$ μm Mesyats (2000), the lower cylindrical part is small in order not to unnecessarily increase computation time, it is large enough for the time life of the cathode spot chosen. The method of calculation uses the symmetry properties of the axisymmetry electrode. To make the mesh, then the calculations should be considered only the area bounded in the axial plane of the diagram by the symmetry z axis (right part of Fig. 5). This party is represented schematically in Fig. 6, the scale of the mesh is not observed in this figure for readability, the finest meshes are equal to 0.2×10^{-7} m, the greatest differ by a factor 5.

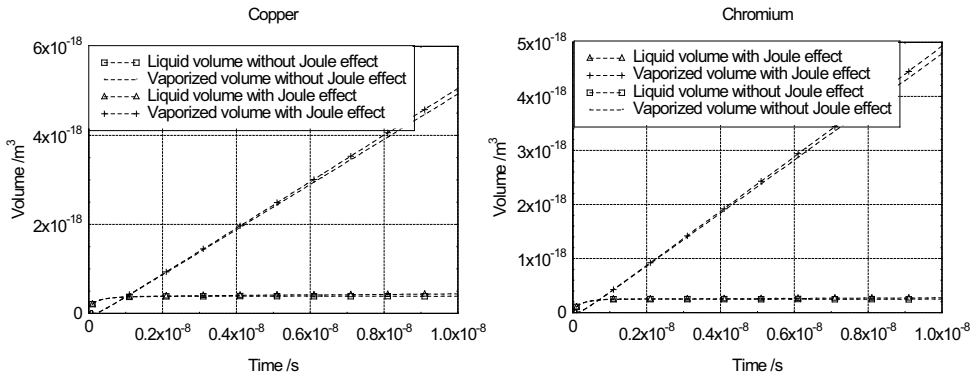

Fig. 4: Vaporized and liquid volume for copper and chromium with and without Joule effect.

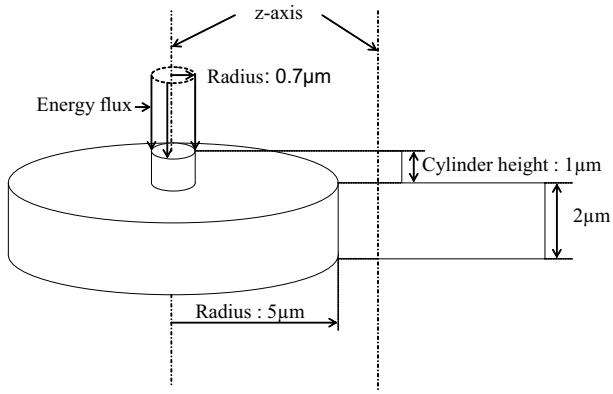

Fig. 5: Electrode with a cylindrical tip.

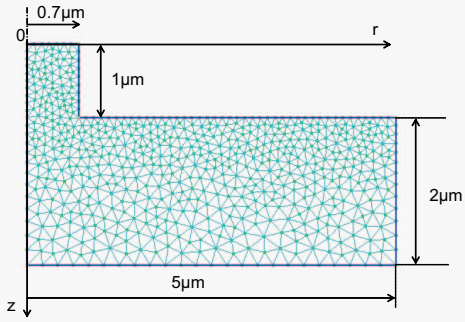

Fig. 6: Mesh used for the electrode.

4.2 Simulation Results about Copper

The results for the two materials are quite similar, only those for copper will be presented in detail. There are two stages: the erosion of the cylindrical tip, then after a transition phase, the erosion of the flat part of the electrode. For the first stage the value of heat flow is the same as defined for the cylinder in section 3.2, a value equal to 2.34×10^{13} W/m^2.

Figure 7 on time $t = 0.4$ ns shows that the phase of spraying is already active and that the erosion is effective, the liquid layer is about 0.2 μm, this value remains constant throughout the erosion phase of the cylindrical tip. Figure 8 shows the temperature changes that have already made in the electrode at $t = 2.6$ ns, only a small portion of the tip is still visible. From Jüttner (2001) the values of the radius of cathode spot currents of 10A are greater than the value $r = 0.7$ μm, an expansion of the value of the surface on which the flow of ions arrives is necessary. The theory of section 2.1 shows that the spray may not stop, otherwise the production of metal ions can not stop, hence a new value of the appropriate flux is necessary for that condition will be satisfied. This theory also shows the need for an electric field sufficient to

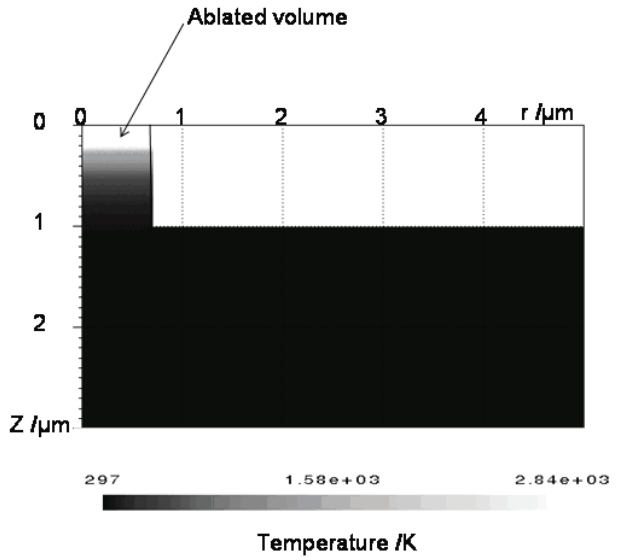

Fig. 7: A representation of the cylindrical tip at $t = 0.4$ ns.

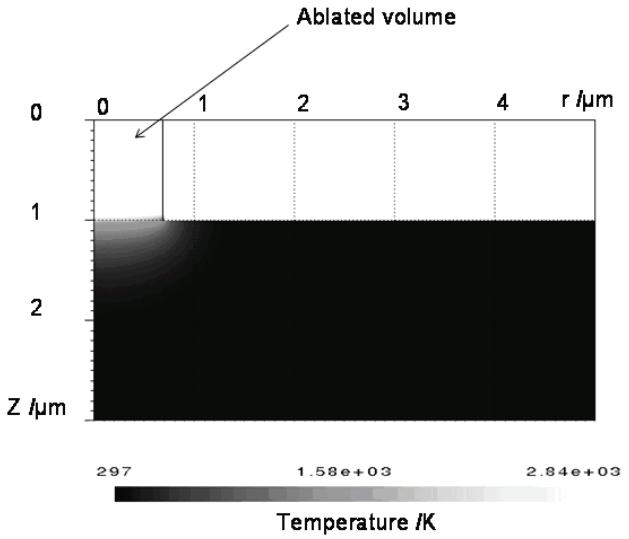

Fig. 8: At $t = 2.6$ ns the cylindrical tip is nearly ablated.

ensure the electronic emission, implying a value not too much of the depth of the crater obtained in relation to its diameter. After several numerical tests, it appears clearly that for the evolution of the radius at $t = 2.7$ ns, in the case of copper only the stepped function limits the digging too fast from the crater, and only the factor of 2 to increase the radius of the surface flow leads to a continuous emission of metal vapour. Figures 9 and 10 show respectively the evolution of the electrode at $t = 2.8$ ns and at $t = 5.0$ ns, the values of temperatures give clearly the position of

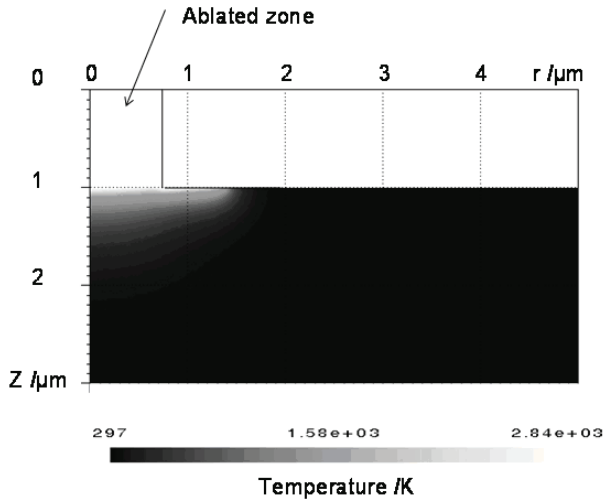

Fig. 9: The electrode at $t = 2.8$ ns with a cathode spot radius equal to 1.4 μm.

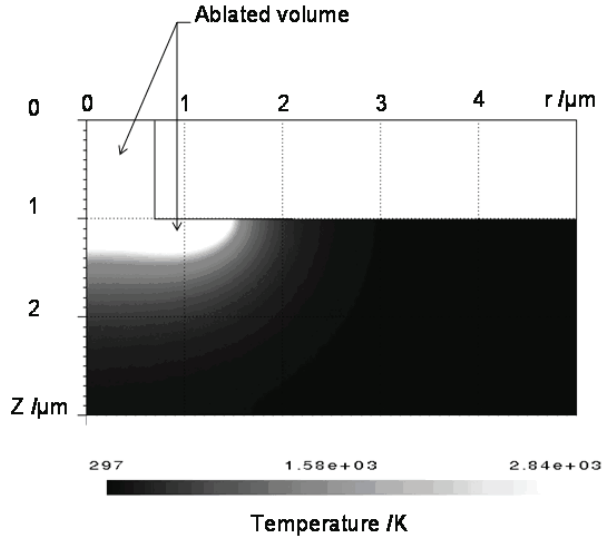

Fig. 10: The electrode at $t = 5.0$ ns.

liquid and solid phases, Fig. 9 shows that erosion is effective after the change of the radius value of the cathode spot. The temperature on the z-axis, represented Fig. 11, for different instants, evolves in a linear fashion in the liquid phase and in a more conventional one in the solid. The small horizontal area between these two phases is in the solid phase, it follows from the linear variation that replaces the enthalpy jump between solid and liquid, this linearization is necessary to satisfy the calculation method.

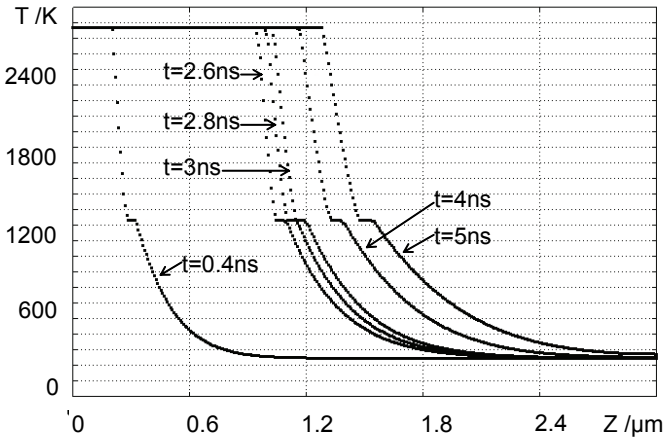

Fig. 11: Temperature evolution on the z-axis versus time for copper.

4.3 Results for the Two Materials

The same reasoning and the same calculations are made for chromium, although different results have similarities. In Fig. 12 the evolution of volumes liquefied and sprayed metal are similar in both cases, for the tip, the spray volume is a linear function of time and the liquid layer is almost constant. After the change in size of the area that receives the ion flow, the spray is maintained, and the volume of the liquid phase is changing rapidly, this phenomenon results from a new division of enrgy between the three phases.

Erosion can be defined here as the result of the vaporization of metal, Table 3 gives the values obtained for copper and chromium at the cathode spot on the

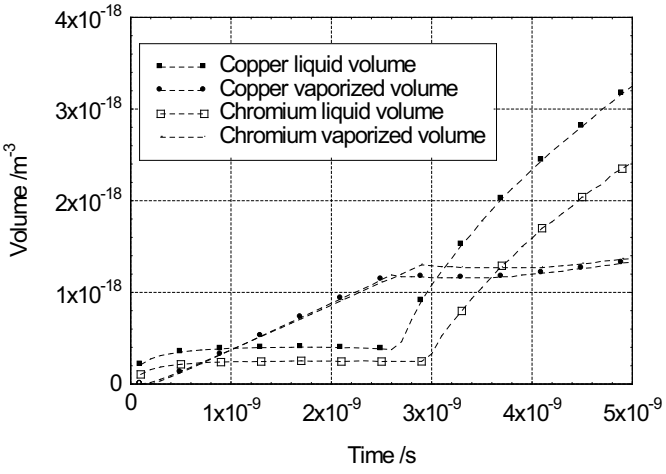

Fig. 12: Vaporized and liquid volumes versus time for copper and chromium electrode.

Table 3: Erosion results for the tip and the electrode.

	Copper	Chromium
Time tip erosion /ns	2.7	3.0
Rate tip erosion /μg/C	520	430
Rate electrode erosion /μg/C	100	30

cylindrical tip of radius 0.7 μm, and then for the electrode that receives the energy flux through a circular area of radius 1.4 μm. Erosion rates are obtained for the two materials, a comparison with literature (Daalder (1976) gives 40 μg/C for copper on a post-mortem spot) shows that the values calculated here are higher than those commonly measured, this follows from to have not take in account the come back of metal vapours on the electrode outside the zone occupied by the spot, and metal vapour coming from the anode.

5. CONCLUSION

The study clearly shows that the cylinder explodes not like a fuse or melts not like a molten bridge, because the energy provided by the cathode spot is predominant compared to that released by Joule effect. The duration of disappearance of a peak height equal to 1 μm average is less than 3 ns.

In conclusion, the first values obtained on the erosion of the two materials lead to fairly consistent results which will result in a conservation of the properties of the alloy, the surface of the electrode does not see its composition enriched in copper or chromium. A more detailed analysis of these results for chromium gives the values of erosion and production of liquid phase lower than for copper, this is a stabilizing factor for the matrix of copper.

To reply to technical considerations on the erosion of copper-chromium alloys, the results are consistent with the theoretical creation of a macroscopic material that integrate the thermodynamic average properties of the two components. Examination of Fig. 2, where the enthalpies and phase change temperatures of these two materials are important differences, clear limits to this approach.

The transition between the evolution of the spot having reached the base of the tip and its extension on the surface of the electrode must meet two requirements: the maintenance of a high electric field and the maintenance of the evaporation of metal. In this case it is clear that this development can only be done by a step function where the radius of the new spot may not take a value more than twice the radius of the tip. The study was limited to a life time of the spot equal to 5 ns, for a life time more important it is necessary to further increase the radius of the surface receiving the energy of the ions and emit new hypotheses, particularly on the radial distribution of current due to the return of ions which would probably lead to a continuous evolution as a function of time of the radius of the cathode

spot. To have new results in that direction experimental confrontation is necessary.

REFERENCES

M.Abbaoui, A.Lefort, S.Clain, and J.Rossignol, A comparative study of the behaviour of copper, silver and nickel submitted to a high power flux density, *Eur. Phys. J. Appl. Phys.*, 2005, 31, pp. 45–51.

I.Beilis, G.A.Liubimov, and V.I.Rakhovskii, *Dokl. Akad. Nauk. SSSR*, 1969, 1988, pp. 202–9, (in russian).

I.Beilis, Theoretical modelling of cathode spot phenomena *Handbook of Vacuum Arc Science and Technology,* ed R.L.Boxman, P.J.Martin, and D.M.Sanders (New Jersey: Noyes), 1995, pp. 208–56.

I.Beilis, B.E.Djakov, B.Jüttner, and H.Purch, Structure and dynamics of high-current arc cathode spots in vacuum, *J. Phys. D: Appl. Phys.*, 1997, 30, pp. 119–30.

M.W.Chase, C.A.Davies, J.R.Downey, D.J.Frurip, R.A.McDonald, and A.N.Syverud, *JANAF Thermochemical tables, J. Phys. Chem. Ref. Data*, 4^{th} edn. (USA), 1998.

J.D.Cobine and E.E.Burger, Analyse of electrode phenomena in the high-current arc, *J. Appl. Phys.*, 1955, 7, pp. 895–8.

J.E.Daalder, Components of cathode erosion in vacuum arcs, *J. Phys. D: Appl. Phys.*, 1976, 9, pp. 2379–95.

V.E.Grakov, Cathode fall on an arc discharge in a pure metal, *Sov. Phys-Tech. Phys.*, 1967, 12, pp. 286–92.

B.Jüttner, Cathode spots of electric arcs, *J. Phys. D:Appl. Phys.*, 2001, 34, R103–R123.

T.Klein, J.Paulini, and G.Simon, Time-resolved description of cathode spot development in vacuum arcs, *J. Phys. D:Appl. Phys.*, 1994, 27, pp. 1914–21.

T.H.Lee, Energy distribution and cooling effect of electrons emitted from an arc cathode, *J. Appl. Phys.*, 1960, 31(5), pp. 924–7.

T.H.Lee and A.Greenwood, Theory for the cathode mechanism in metal vapour arc, *J. Appl. Phys.*, 1961, 33, pp. 916–23.

D.R.Lide, Handbook of Chemistry and Physics (CRC Press LLC, USA), 2001, 10, pp. 175–6.

E.L.Murphy and R.H.Good, Thermionic Emission, Field Emission, and the Transition Region, *Phys. Rev.*, 1956, 15, pp. 1464–73.

G.A.Mesyats, Cathode Phenomena in a Vacuum Discharge ed Moscow: Nauka, 2000.

J.Prock, Time dependant description of cathode crater formation in vacuum arcs, *IEEE Trans. Plasma Sci.*, 1986, 14, pp. 482–91.

J.Rossignol, M.Abbaoui, and S.Clain, Numerical modelling of thermal ablation phenomena due to a cathodic spot, *J. Phys. D:Appl. Phys.*, 2000, 33, pp. 2079–86.

D.C.Strachan and M.Barrault, Axial velocity variation in high current free burning arc, *J. Phys. D: Appl. Phys.*, 1976, 9, pp. 435–46.

HIGH TEMPERATURE MATERIAL PROCESSES **14** (2010) 285-294

COMPOSITION OF A THERMAL PLASMA FORMED FROM PTFE WITH COPPER IN NON-OXIDANT ATMOSPHERE, PART I: DEFINITION OF A TEST CASE WITH THE SF_6

P. Andre[1], **Z. Koalaga**[2]

[1] *LAEPT, Blaise Pascal University, 24 av des Landais 63117 Aubiere Cedex, France*
[2]*LAME, Ouagadougou University, 03 BP7021, Ouagadougou, Burkina Faso*

ABSTRACT: The aim of this paper is to draw the main characteristic from theoretical calculations of a good dielectric gas. The SF_6 is widely used in the electrical industry for its dielectric and insulating properties. In the purpose to define available parameters, we study the molar fractions of chemical species in PTFE, SF_6, Cu mixture for several proportions and pressures. We show that the carbon solid formation and condensed copper formation depends on the SF_6 proportions and the presence of the electronegative ions F^-.

KEY WORDS: circuit breakers, SF_6, PTFE, carbon formation, copper, dielectric gas, plasma composition

1. INTRODUCTION

PTFE $(C_2F_4)_n$ and sulphur Hexafluoride SF_6 are widely used in industry for electrical insulating purposes and also in circuit breakers (Chu, 1986; Qui et al., 1987; Pham et al., 1995; Fleischer et al., 1998; Chritophorou et al., 1997). The SF_6 gas has been well studied since a long time ago (Chritophorou et al., 1997). The thermodynamic properties and transport coefficients are well understood in the gas and plasma phase (Chervy et al., 1994; Krenek, 1992; Belov and Semenov, 1971). Nevertheless the molar fractions of condensed phase had not been studied in details. Notwithstanding, carbon formation on voltage breakdown and sparking is well observed since several years (Mears and Sabatino, 1978; Hayashi et al., 2001). As a matter of fact, the main consequence of solid condensation is the failure of the breakdown. With the SF_6 gas or by adding some CO_2 or Halogened alkanes this carbon deposit can be partially suppressed (Mears and Sabatino, 1978; Manion et al., 1972). The dielectric gases are useful in medium and high voltage coaxial lines, in circuit breakers in substations and in transformers. At the present time the SF_6 gas is usually used.

To our knowledge in the literature no available data on multiphasic composition can be found in temperatures below 6000 K concerning SF_6 with polymer. This

data can be useful to understand the creation or the cooling of the arc. Usually the contactors or the guide of the arc roots is usually constituted of copper. The arc surrounding material is made of polymer or contains it. In the working conditions the pressures can be vary from 1 bar to 30 bars (Boveri, 1977; Shiminn et al., 1990) That is why we choose to study the polyphasic compounds of plasma mixtures of (PTFE, SF_6, Cu).

First, we describe the data base and the computation calculation code. Secondly we describe the results obtained for three mixtures of (PTFE, SF_6, Cu) respectively (1%, 98%, 1%); (50%, 49%, 1%) and (98%,1%, 1%) in weight percentage (wp) and also we discuss the results obtained for three pressures 1 bar, 10 bars and 30 bars for the (50%, 49%, 1%).

In conclusion and from these theoretical results, we give the conditions of a good insulating case. This conditions can be used has a definition of a case test.

2. THEORETICAL FUNDS

2.1 Physical Formulation

The computation of the chemical equilibrium of mixtures as (SF_6, $(C_2F_4)_n$, Cu) is based on the solving of equation derived from classical thermodynamics. The thermodynamic principles are valid for ideal plasma and heterogeneous plasma. Several authors use indifferently the minimization of given thermodynamic functions or mass action laws even with plasmas out of thermal equilibrium (Tanaka, 1997; Andre, 1997). The mass action laws are never used for the heterogeneous case.

In our case we consider the pressure and the temperature as fixed constraints. The thermodynamic function is the Gibbs free energy that has to be minimal if the thermodynamic system reached the thermodynamic equilibrium. So we assume the thermodynamic equilibrium for the condensed phase, the gas and the plasma. We can write this function has the sum of two terms. The first term depends on the plasma and gas phases G_{pg}, and the second term depends on the liquid and solid phases G_{ls}.

- G_{pg} is written as:

$$G_{pg} = \sum_{i=1}^{N_{pg}} n_i \left(\mu_i^0 + RT \ln \left(\frac{n_i}{\sum_{j=1}^{N_{pg}} n_j} \right) + RT \ln \left(\frac{P}{P^0} \right) \right) \qquad (1)$$

where n_i is the mole number, N_{pg} is the number of different species present in the plasma and gas, μ_i^0 is the chemical potential of i species at pressure reference P^0.

- G_{ls} is written as:

$$G_{ls} = \sum_{i=1}^{N_{ls}} n_i \mu_i^0 \tag{2}$$

N_{ls} is the number of liquid and solid phases taken into account for a given temperature. μ_i^0 is the chemical potential of i species at pressure reference P^0. The liquid is assumed to be an ideal and pure liquid that is to say there is no diffusion of the others species inside the liquid. The condensed phases (solid and liquid) are immiscible. Consequently the composition of a condensed phase follows the initial mass percentage.

2.2 Data Sources for the Species Thermodynamic Calculation

The pressure influence on the melting temperature of copper is low in our considered temperature range (Bridgman, 1949). For this reason the same melting temperature for all considered pressures has been chosen fixed at 1358 K (JANAF, 1998).

The thermodynamic properties versus temperature are taken from (JANAF, 1998) for solid and liquid copper. The thermodynamic properties for solid carbon are those of the graphite taken from (JANAF, 1998). For the gaseous polyatomic species data are taken from (JANAF, 1998). For the monatomic and diatomic species the thermodynamic properties are calculated from the partition functions (Andre, 1995; Rochette et al., 2004). The enthalpies of formation are taken in (JANAF, 1998).

In our calculation, for the SF_6, PTFE, Cu mixtures, 12 monatomic species are taken into account: C, C^-, C^+, Cu, Cu^-, Cu^+, F, F^-, F^+, S, S^-, S^+ and electrons, 20 diatomic species: C_2, C_2^-, C_2^+, CF, CF^+, CS, CS^-, CS^+, Cu_2, CuF, CuS, F_2, F_2^-, F_2^+, S_2, S_2^-, S_2^+, SF, SF^-, SF^+ and 37 polyatomic species C_2F_2, C_2F_4, C_2F_6, C_3, C_4, C_5, CF_2, CF_2^+, CF_3, CF_3^+, CF_4, CF_8S, CS_2, CuF_2, $F_{10}S_2$, SF_2, SF_2^-, SF_2^+, SF_3, SF_3^-, SF_3^+, SF_4, SF_4^-, SF_4^+, SF_5, SF_5^-, SF_5^+, SF_6, SF_6^-, FSSF, S_3, S_4, S_5, S_6, S_7, S_8, SSF_2.

2.3 Numerical Method

The mole number must be non-negative and satisfy the conservation of nuclei and quasi neutrality, so the different values n_i must satisfy both conditions:

$$\begin{cases} {}_i \geq 0 \qquad \forall\, i \\ \sum\limits_{i=1}^{N_{pg}} a_{i\,j}\, n_i \;=\; b_j \; j = 1,..,m \end{cases} \tag{3}$$

where m is the number of different nuclei. It is equal to 4 in our case (C, Cu, F, S). $j = 0$ is devoted to the electrical neutrality. $a_{i\,j}$ represents the nucleus number of type j for particle i; b_j is equal to the number of different nucleus types in the initial mixture; a_{i0} represents the number of electric charges of type j for particle i; so

electrical neutrality imposes $b_0 = 0$. By introducing Lagrange multipliers π_k to take the physical conditions (3) into account and using a Newton-Raphson numerical method a system of equation is obtained (Rochette et al., 2004).

The convergence is considered to be reached when the values Δn_i satisfy the following relation:

$$\Delta n_i < 10^{-15} n_i \quad \forall i \quad \in [1, N_{pg} + N_{ls}] \tag{4}$$

In chemical equilibrium thermodynamical calculation, the main difficulty is the choice of the number of condensed (liquid and solid) species. So, the requirement for a new condensed species, which was not previously included as a possible species to now, is that its inclusion will decrease Gibbs energy. So, the test given in (Gordon and McBride, 1976) for the two following species Cu (liquid and solid) and C(solid) at each step of temperature is used.

3. SF_6, $(C_2F_4)_N$, CU MIXTURES

3.1 Influence of Stoichiometric Parameters

In Fig. 1, the molar fraction has been plotted for three mixtures based on SF_6, PTFE and copper. In the case 1, 1% $(C_2F_4,)_n$, 98% SF_6, 1% Cu in weight percentage, the main chemical species are SF_6, SF_4, CF_4 and CuF_2. We do not observe any condensed phase in the considered temperature range. The SF_6 molecules dissociate in SF_4 and F at temperature around 1800 K. SF_4 molecules dissociate in SF_2 and F at a temperature around 2240 K and SF_2 molecule dissociate in SF and F around a temperature of 3000 K. Around 3080 K the diatomic molecules SF dissociate in S and F. For the higher temperature 6000 K the main chemical species are monatomic F, S, C and Cu that the basic elements of the mixture. For the charged particles, the electrical neutrality is reached between Cu^+ and F^- for the temperature lower than 4500 K and e^- and Cu^+ for the higher temperature in the considered temperature range.

In the case 2, 50% $(C_2F_4)_n$ 49% SF_6 1% Cu, the main chemical species are CF_4, SSF_2, S_2 and solid copper. The CF_4 molecules dissociate in CF_2 and F at a temperature around 2900 K. CF_2 molecules dissociate in CF and F around 3650 K and CF dissociates in C and F around 4500 K. The solid copper sublimates in CuF and CuF_2 at a temperature of 1350 K. For the higher temperature at 6000 K the main chemical species are F, S, C, CF, CS, Cu and C_2. The electrical neutrality is reach between Cu^+ and F^- for the temperature lower than 4500 K and e^- and Cu^+ for the higher temperature in the considered temperature range.

In the case 3, 98% $(C_2F_4,)_n$ 1% SF_6 1% Cu, the main chemical species are solid carbon, CF_4, and solid copper at low temperature. The CF_4 molecules dissociate in CF_2 and F at a temperature around 2690K. CF_2 molecules dissociate in solid carbon and F between 3050 K and 3700 K. Thus the molar fraction of solid carbon is stable

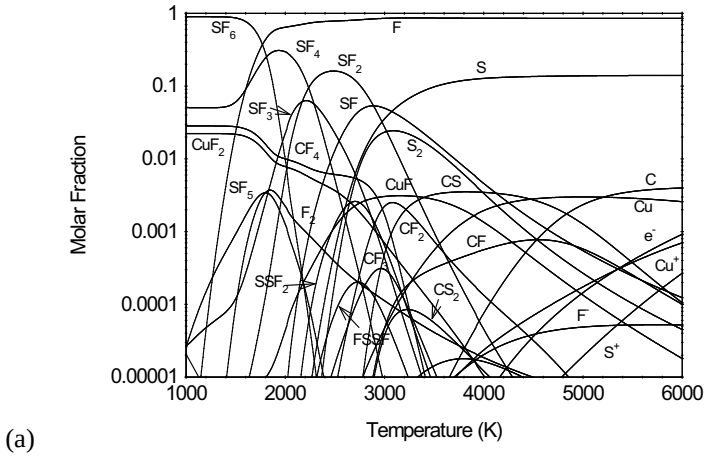

(a)

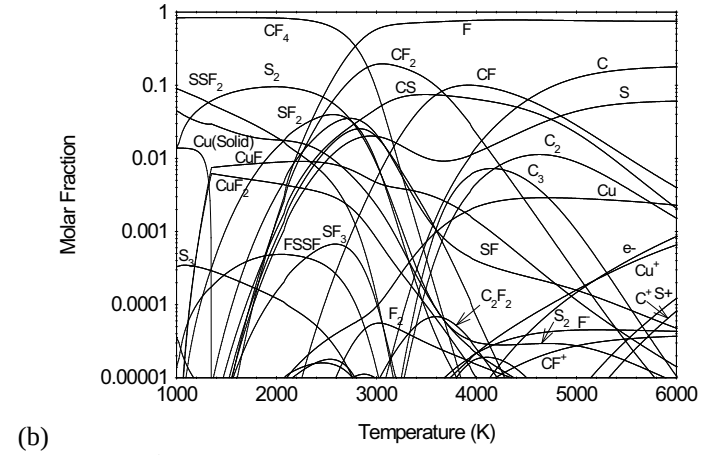

(b)

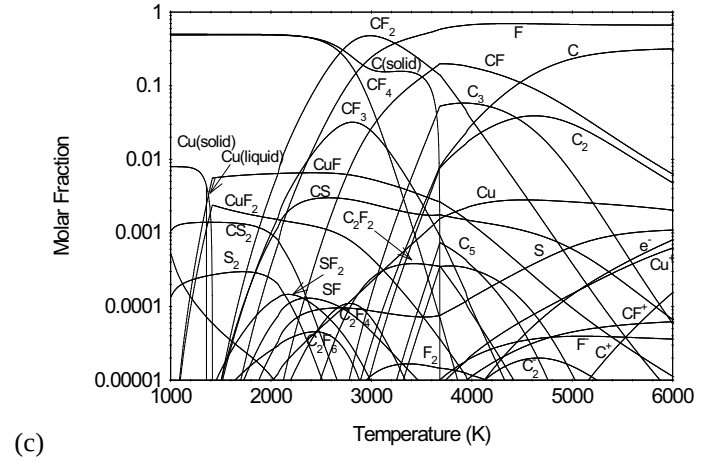

(c)

Fig. 1: Molar fraction versus temperature at 1 bar for a mixture of (a) 1% $(C_2F_4)_n$, 98% SF_6, 1% Cu in weight, (b) 50% $(C_2F_4)_n$, 49% SF_6, 1% Cu in weight, and (c) 98% $(C_2F_4)_n$, 1% SF_6, 1% Cu in weight percentage.

in this temperature range. At 3685 K, when solid carbon sublimates in CF and C_3, the CF_2 molecules dissociate in CF and F. Around 4480 K, CF dissociates in C and F. The liquid phase of copper vaporizes at 1418 K in CuF and CuF_2. For the higher temperature 6000 K the species are monatomic F, C, CF, C_2 and Cu. The electrical neutrality is reach between Cu^+ and F^- for the temperature lower than 4500 K and e^- and Cu^+ for the higher temperature in the considered temperature range.

Comparing the three considered cases, the role of stoichiometric coefficients are indubitable. The chemical compounds are different and depends on the proportion of SF_6 and $(C_2F_4,)_n$. The higher the proportion of SF_6 the lower the proportion of solid carbon is. We also notice the CF_4 molecules that are present in each considered cases. The neutrality in gas phase is made at low temperature between F^- and Cu^+. In Fig. 2, we present the evolution of the solid carbon and the condensed copper for several proportions of SF_6 and PTFE. For the high proportion of SF_6 ($>$50% in wp) the solid and liquid phases of copper and solid phase of solid carbon disappear in the considered temperature range.

3.2 Influence of the Pressure

In Fig. 3, in the case of 50% $(C_2F_4)_n$, 49% SF_6, 1% Cu in weight percentage for two pressures 10 bars and 30 bars, the molar fraction are plotted versus the temperature. The dissociation of CF_4 in CF_2 and F is made at 2900 K at 1 bar, 3160K at 10 bars and 3500 K at 30 bars. CF_2 dissociates in CF and F around 3650 K at 1 bar, 4200 K at 10 bars and 4525K at 30 bars. CF dissociates in C and F around 4500 K at 1 bar, 5300 K at 10 bars and 5800 K at 30 bars. The solid copper sublimates in CuF and CuF_2 at a temperature of 1350 K at 1 bar, 1480 K at 10 bars and 1550 K. The solid carbon appears at low temperature and sublimates at 1015 K for a pressure of 30 bars. For the higher temperature 6000 K, we observe the higher pressure the higher molecule molar fractions. So the main species for 6000 K at 1 bar are F, S, C, CF, CS, Cu and C_2 and for 30 bars F, C, CF, S, CS, C_2, CF_2 and C_3. The electrical neutrality is reach between Cu^+ and F^- for the temperature lower than 4500 K and e^- and Cu^+ for the higher temperature in the considered temperature range at 1 bar. For 10 bars, the electrical neutrality is reach between Cu^+ and F^- for the temperature lower than 5260 K and e^- and Cu^+ for the higher temperature. For 30 bars, the electrical neutrality is made between F^-, CF^+ and Cu^+.

4. CONCLUSION

In this paper, we have presented the molar fraction of mixture of PTFE, SF_6 and copper for several proportions and pressures versus the temperature. The SF_6 is remarkable since it has different behaviour versus its proportions in the mixture. As a matter of fact we have shown that the chemical composition and the presence of non electrical conducting species at low temperature in the mixture depend on the

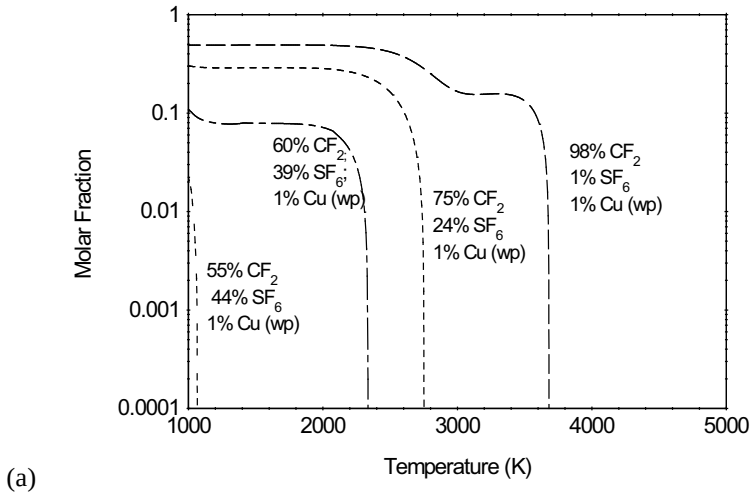

(a)

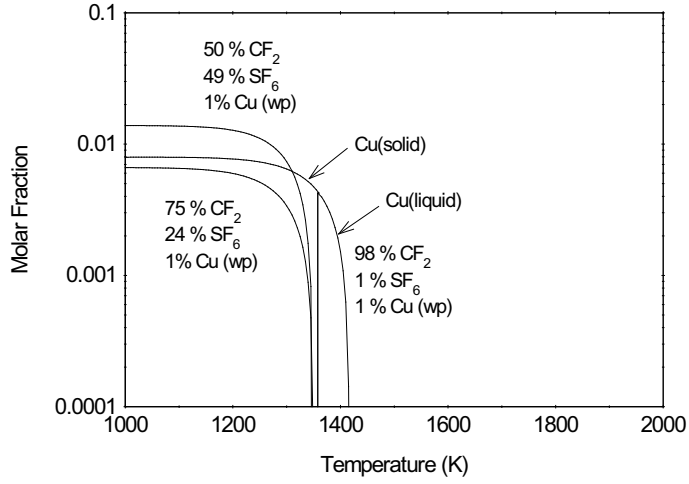

(b)

Fig. 2: (a) Evolution of solid carbon formation molar fraction versus temperature and for several proportion of SF_6, $(C_2F_4)_n$ and Cu, (b) evolution of copper molar fraction versus temperature and for several proportions of SF_6, $(C_2F_4)_n$ and Cu.

proportion of the SF_6. Furthermore, we have shown that the solid carbon formation and condensed copper disappears when a high proportion of SF_6 is present in the plasma. So to test the efficiency of a dielectric gas, we have to study the solid carbon formation and condensed copper. Furthermore, the presence of the electronegative ions F^- helps to avoid the re-strike of the arc. As a mater of fact, the mobility of ions is lower than electrons. The presence of electronegative species in a good proportion is also required to avoid re-strike of the arc.

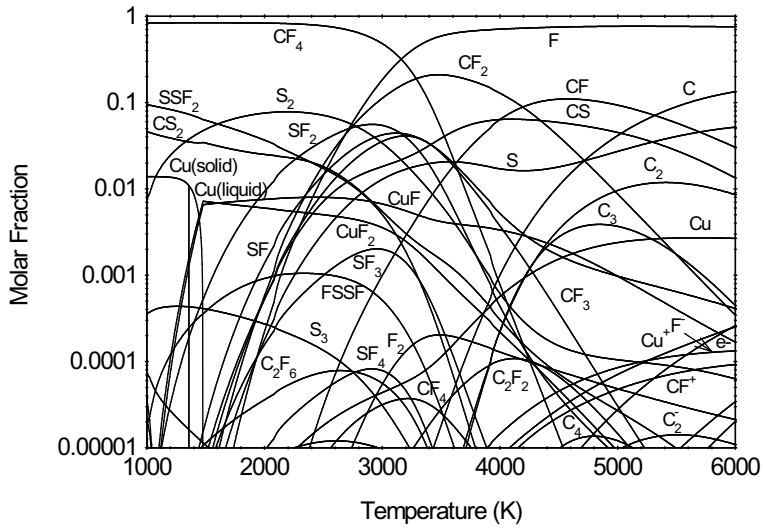

(a)

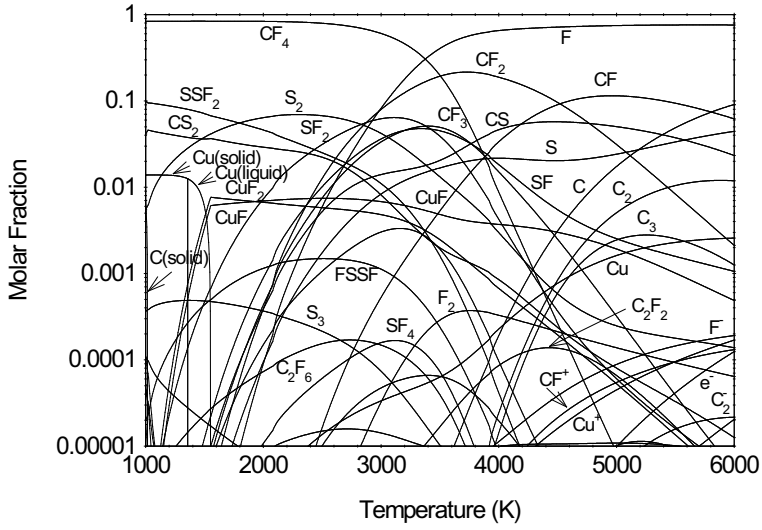

(b)

Fig. 3: (a) Molar fraction versus temperature at 10 bars for a mixture of 50% $(C_2F_4)_n$, 49% SF_6, 1% Cu in weight percentage, (b) molar fraction versus temperature at 30 bars for a mixture of 50% $(C_2F_4)_n$, 49% SF_6, 1% Cu in weight percentage.

ACKNOWLEDGMENTS

The authors wish to thank the European Edulink Program for their financial support to help the development of scientific cooperation between Blaise Pascal University and University of Ouagadougou, and the two laboratories LAME and LAEPT.

REFERENCES

P.Andre, Partition functions and concentrations in plasmas out of thermal equilibrium, *IEEE Transactions on Plasma Science*, 23(3), pp. 453–458, 1995.

P.Andre, Etude d'un plasma de SF_6 hors d'équilibre thermique, *J. Phys. III*, 1997, 7, pp. 1339–1359 (in French).

V.A.Belov and A.M.Semenov, Calculation of the thermal conductivity of a sulfur hexafluorides plasma in the range $10^3 < T < 20\ 10^3$ at pressures of 1, 2, 5 and 10 atm, *Teplofizika Vysokikh Temperatur*, 1971, 9(2), pp. 282–289.

B.Boveri, Theoretical description of the current interruption in HV gas blast breakers, I*EEE Transactions on Power Apparatus and systems*, 1977, 96(5), pp. 1546–1555.

P.W.Bridgman, *The Physics of high pressure*, G. Bell and Sons editors, London, 1949.

B.Chervy, A.Gleizes, and M.Razafinimanana, Thermodynamic properties and transport coefficients in SF_6-Cu mixtures at temperatures of 300-30 000K and pressures of 1.-1MPa, *J.Phys D: Appl. Phys.*, 1994, 27, pp. 1193–1206.

L.G.Chritophorou, J.K.Olthoff, and R.J.Van Brunt, Sulfur Hexafluoride and the Electric Power Industry, *IEEE Electrical Insulation Magazine*, 1997, 13(5), pp. 20–24.

F.Y.Chu, SF_6 Decomposition in Gas-Insulated Equipment, *IEEE Transactions on Electrical Insulation*, 1986, 21(5), pp, 693–725.

L.Fleischer, H.J.Müller, R.Poth, and H.Späck, Patent EP19950940161, 09/30/1998.

S.Gordon and B.J.McBride, *Computer Program for Calculation of Complex Chemical Equilibrium Compositions, Rocket Performance, Incident and Reflected Shocks, and Chapman-Jouguet Detonations*, NASA SP-273, 1976

Y.Hayashi, A.Okino, E.Hotta, T.Uchii, G.Cliteur, and K.Suzuki, Observation of weakly Ionized Dusty Plasma in Exhaust gas in a compact size SF6 gas circuit breaker, *IEEE Transactions on plasma science*, 2001, 29(1), pp. 99–101.

JANAF, *Thermochemical tables*, 4^{th} edn, MW Chases (ed.), J Phys. Chem. Ref Data, 1998, 9.

P.Krenek, Thermophysical properties of the reacting mixture SF_6 and Cu in the range 3000 to 50000 K and 0.1 $\times$ 2 MPa, *Acta Techn CSAV*, 1992, 37, pp. 399–410.

J.P.Manion, J.A.Philosophos, and M.B.Robinson, US Patent 3650955, 1972

W.H.Mears and R.O.Sabatino, US Patent 4071461, 1978.

V.D.Pham, E.Thuries, and J.Martin, Patent EP19910117923, 12/20/1995.

Y.Qui, A.Sun, and E.Kuffel, Improved Dielectric Strength of SF_6 Gas with a Trichlorotrifluoroethane Vapor Additive, 1987, 22(6), pp. 763–768.

D.Rochette, W.Bussiere, and P.Andre, Composition, Enthalpy, and Vaporization Temperature Calculation of Ag-SiO_2 Plasmas with Air in the Temperature Range from 1000 to 6000 K and for Pressure Included between 1 and 50 bars, *Plasma*

Chemistry and Plasma Processing, 2004, 24(3), pp. 475–492.

D.W.Shiminn, G.R.Jones, and S.M.G.Ali, Transient pressure variations in SF6 puffer circuit breakers, *J. Phys D: Appl. Phys.*, 1990, 23, pp. 533–541.

Y.Tanaka, Particle composition of high pressure SF_6 plasma with electron temperature greater than gas temperature, *IEEE Transactions on plasma science*, 1997, 25(5), pp. 991–995.

HIGH TEMPERATURE MATERIAL PROCESSES **14** (2010) 295-303

COMPOSITION OF A THERMAL PLASMA FORMED FROM PTFE WITH COPPER IN NON-OXIDANT ATMOSPHERE, PART II: COMPARISON OF A TEST CASE WITH NITROGEN

P. Andre[1], **Z. Koalaga**[2]

[1] *LAEPT, Blaise Pascal University, 24 av des Landais 63117 Aubiere Cedex, France*
[2]*LAME, Ouagadougou University, 03 BP7021, Ouagadougou, Burkina Faso*

ABSTRACT: The aim of this work is to compare the main characteristic of good dielectric gas defined in our previous paper with nitrogen gas. We study the molar fraction of chemical species in PTFE, N_2 and Cu mixture for several proportions and pressures. We show that the nitrogen gas does not satisfy the characteristic of good dielectric leading manufacturers to modify entirely their electrical insulation set up.

KEY WORDS: circuit breakers, nitrogen, PTFE, carbon formation, copper, dielectric gas, plasma composition

1. INTRODUCTION

In our previous paper we have defined a test case with the SF_6, PTFE and Cu to choose the better insulating compounds (Andre and Koalaga, 2010). As a matter of fact the SF_6 gas is widely used for electrical insulating and in high voltage circuit breakers (Chu, 1986; Qui et al., 1987; Pham etal., 1995; Fleischer et al., 1998; Chritophorou et al., 1997). During the last decade the main published papers were devoted to the modeling of the gas phase and the plasma phase at thermal equilibrium or in plasma out of thermal equilibrium (Gonzalez et al., 2000; Lee and Kim, 2006; Yokomizu et al., 2009). In such modeling the condensed phase is not considered that is why such calculation has to be made in the temperature range where the condensed phases appear. That is to say between 1000 and 6000 K.

The environmental impact and the life cycle cost are, at the present time, keys for new markets. So the competition between industries is high for their image and for the purchasers to find alternatives.

Studying the electrical breakdown strength of nitrogen and SF_6 with Pashen curves (Koch, 1997) one can think that by modifying the pressure we can obtain the same breakdown strength. That is to say with a higher pressure the electrical breakdown strength of nitrogen is the same that the one of SF_6. For the test case with SF_6, PTFE and Cu we have shown that we have to avoid the production of

condensed matter and that we have a good proportion of electronegative species decreasing the electrons mobility (Andre and Koalaga, 2010). The composition results can give available indications. Consequently, the study of the composition for N_2, PTFE and Cu with a pressure of 1 to 30 10^5 Pa is useful.

First we explicit the chosen chemical species and the specific enthalpy calculation with condensed phase. Secondly, we study the results for three mixtures case 1: 1% $(C_2F_4)_n$, 98% N_2, 1% Cu in weight percent (wp); case 2: 50% $(C_2F_4)_n$, 49% N_2, 1% Cu in weight percent (wp) and case 3: 98% $(C_2F_4)_n$, 1% N_2, 1% Cu in weight percent (wp) and for the case 2 with three pressures 1, 10 and 30 10^5 Pa. Finally, we give a conclusion.

2. CHEMICAL SPECIES AND ENTHALPY CALCULATION

In our calculation, for the N_2, PTFE, Cu mixtures, 11 monatomic species are taken into account: C, C^-, C^+, Cu, Cu^-, Cu^+, F, F^-, F^+, N, N^+ and electrons, 17 diatomic species: C_2, C_2^-, C_2^+, CF, CF^+, CN, CN^-, CN^+, Cu_2, CuF, F_2, F_2^-, F_2^+, FN, N_2, N_2^-, N_2^+ and 25 polyatomic species: C_2F_2, C_2F_3N, C_2F_4, C_2F_6, C_2N, C_2N_2, C_3, C_4, C_4N_2, C_5, CF_2, CF_2^+, CF_3, CF_3^+, CF_4, CFN, CNN, CuF_2, F_2N, F_2N_2_C, F_2N_2_T, F_3N, F_4N_2, N_3, NCN. For solid and liquid phases we take the carbon solid, liquid copper and solid copper into account. As in our previous paper, the thermodynamic properties versus temperature are taken from (JANAF, 1998) for solid and liquid copper. The thermodynamic properties for solid carbon are those of the graphite taken from (JANAF, 1998). For the gaseous polyatomic species data are taken from (JANAF, 1998). For the monatomic and diatomic species the thermodynamic properties are calculated from the partition functions (Andre, 1995). The enthalpies of formation are taken in (JANAF, 1998). To determine the composition we used the numerical method as described in (Andre and Koalaga, 2010; Rochette et al., 2004). Concerning the enthalpy since we have solid and liquid phases we calculated it by unit of mass.

$$H = \left(\frac{\sum_{i=1}^{N} x_i h_i + \Delta H}{\sum_{i=1}^{N} x_i m_i} \right)$$

where x_i the molar fraction, h_i the specific enthalpy of each chemical species, m_i the molar weight and ΔH the enthalpy correction due to Debye effect that is very low in our temperature range

3. N_2, $(C_2F_4)_N$, CU MIXTURES

3.1 Influence of Stoichiometric Parameters

In Fig. 1, the molar fraction has been plotted for three mixtures based on N_2, PTFE and copper. In the case 1, 1% $(C_2F_4,)_n$, 98% N_2, 1% Cu in weight percent

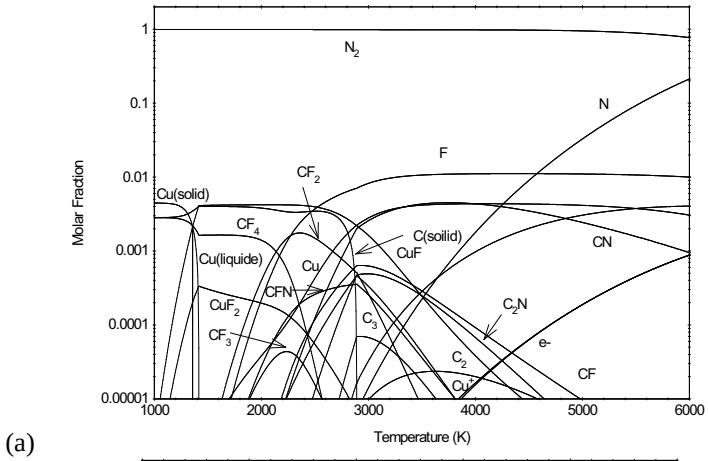

(a)

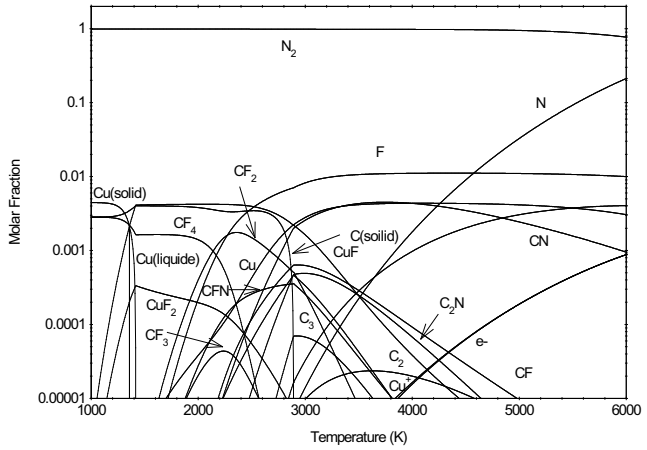

(b)

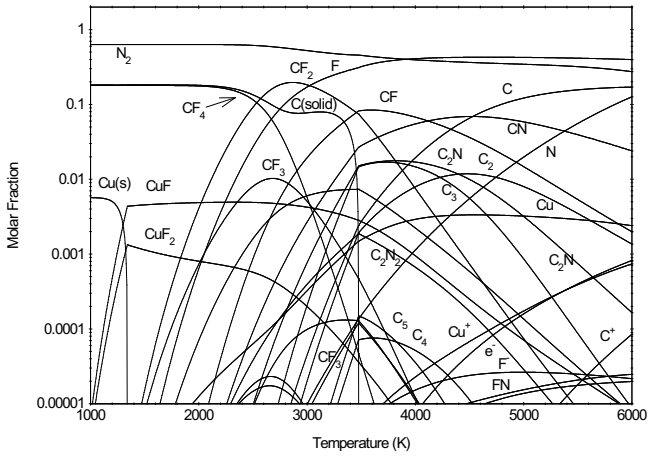

(c)

Fig. 1: Molar fraction versus temperature at 10^5 Pa for a mixture of (a) 1% $(C_2F_4)_n$, 98% N_2, 1% Cu in weight percent (wp), (b) 50% $(C_2F_4)_n$, 49% N_2, 1% Cu in weight percent (wp), and (c) 98% $(C_2F_4)_n$, 1% SF_6, 1% Cu in weight percent (wp).

(wp), the main chemical species is the Nitrogen N_2. We observe condensed phase liquid and solid copper and carbon solid in the considered temperature range. The N_2 molecules does not dissociate at a high rate in the considered temperature range. The carbon solid sublimates in Cyanogen CN around 2890 K. The solid copper sublimates and reacts with F to form CuF before to be in liquid phase. For temperature higher than 3000 K the main species are N_2, N and F. For the charged particles, the electrical neutrality is reached between e^- and Cu^+.

In the case 2, 50% $(C_2F_4)_n$ 49% N_2 1% Cu in weight percent (wp), the main chemical species are N_2, CF_4, solid carbon and solid copper. The CF_4 molecules dissociate in CF_2 and F at a temperature around 2500 K. Equilibrium is established between CF_2 molecules, F and carbon solid until 3480 K when carbon sublimates. For this temperature the CF_2 molecules dissociate in CF and F. The solid copper sublimates in CuF and CuF_2 at a temperature of 1350 K. For the higher temperature at 6000 K the main chemical species are N_2, F, C, N, CN, CF, Cu and C_2. The electrical neutrality is reach between Cu^+ and F^- for the temperature lower than 4250 K and e^- and Cu^+ for the higher temperature in the considered temperature range.

In the case 3, 98% $(C_2F_4,)_n$ 1% N_2 1% Cu in weight percent (wp), the main chemical species are solid carbon, CF_4, Nitrogen N_2 and solid copper at low temperature. The CF_4 molecules dissociate in CF_2 and F at a temperature around 2650 K. CF_2 molecules dissociate in solid carbon and F between 3050 K and 3700 K. Thus the molar fraction of solid carbon is stable in this temperature range. At 3685 K, when solid carbon sublimates in CF and C_3, the CF_2 molecules dissociate in CF and F. Around 4470 K, CF dissociates in C and F. The solid copper sublimates in CuF and CuF_2 at a temperature of 1418 K. For the higher temperature 6000 K the species are monatomic F, C, CF, CN, C_2 and Cu. The electrical neutrality is reached between Cu^+ and F^- for the temperature lower than 4500 K and e^- and Cu^+ for the higher temperature in the considered temperature range.

Comparing the three considered cases, we observe that in each case the carbon solid and the solid copper are presents. So, the modification of proportion between N_2, PTFE, Cu does not allow the creation uniquely of gaseous species. By this way, one can not avoid the carbon solid formation. The CF_4 molecules are present in each considered cases. The neutrality in gas phase is made at low temperature between F^- and Cu^+ and between e^- and Cu^+ for the higher temperature in the considered temperature range.

3.2 Influence of the Pressure

In Fig. 2, in the case of 50% $(C_2F_4)_n$, 49% N_2, 1% Cu in weight percent (wp) for two pressures 10 10^5 Pa and 30 10^5 Pa, the molar fractions are plotted versus the temperature. The dissociation of CF_4 in CF_2 and F is made at 2540 K for 10^5 Pa, 2790 K for 10 10^5 Pa and 2920 K at 30 10^5 Pa. The carbon solid sublimates at

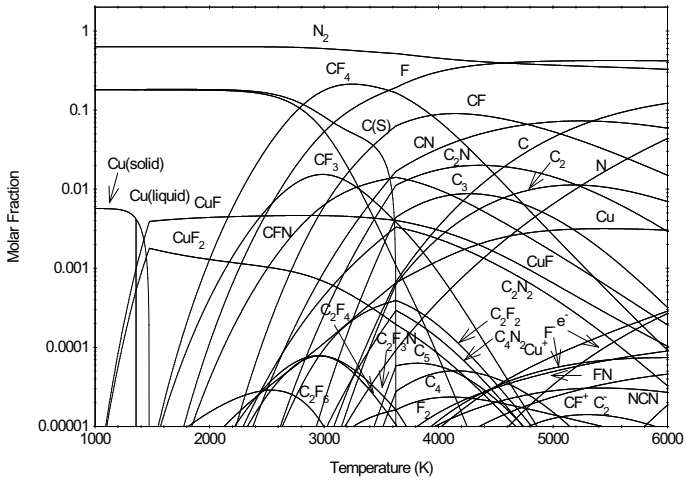

(a)

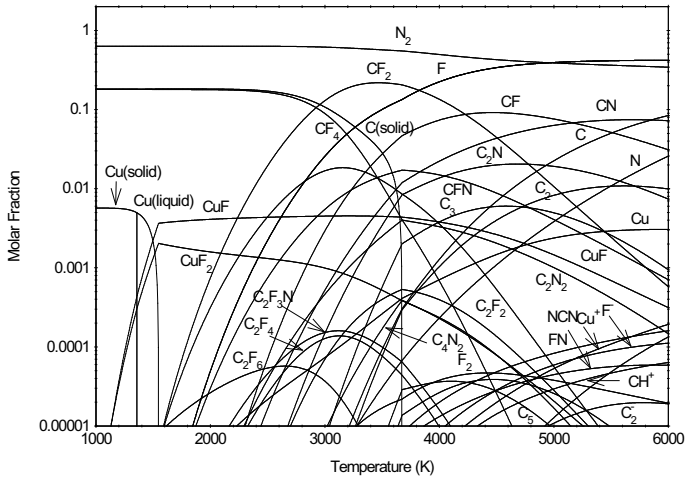

(b)

Fig. 2: Molar fraction versus temperature at (a) 10 10^5 Pa for a mixture of 50% $(C_2F_4)_n$, 49% N_2, 1% Cu in weight percent (wp), (b) 30 10^5 Pa for a mixture of 50% $(C_2F_4)_n$, 49% N_2, 1% Cu in weight percent (wp).

3475 K for 10^5 Pa, at 3630 K for 10 10^5 Pa and at 3670 K for 30 10^5. The CF_2 dissociates in CF and F around 3460 K at 10^5 Pa, 3560 K at 10 10^5 Pa and 3830 K at 30 10^5 Pa. CF dissociates in C and F around 4100 K for 10^5, 3940 K at 10 10^5 and 4220 K at 30 10^5 Pa. The solid copper sublimates and liquid copper vaporized in CuF and CuF_2 at a temperature of 1340 K at 10^5 Pa, 1470 K at 10 10^5 Pa and 1545 K for 30 10^5 Pa. For the higher temperature 6000 K, we observe that the higher the pressure the higher the molecule molar fractions. So the main species for 6000 K at 10^5 Pa are F, N_2, C, N, CN, CF, Cu and C_2 and for 30 10^5 Pa N_2, F, C, CF, CN, N, C_2N, C_2, and Cu. The electrical neutrality is reach between Cu^+ and F^- for the

temperature lower than 4250 K and e^- and Cu^+ for the higher temperature in the considered temperature range at 10^5 Pa. For 10 10^5 Pa, the electrical neutrality is reach between Cu^+ and F^- for the temperature lower than 5230 K and e^- and Cu^+ for the higher temperature. For 30 10^5 Pa, the electrical neutrality is made between F^-, CF^+ and Cu^+.

4. SPECIFIC ENTHALPY

In Fig. 3, we have plotted the specific enthalpy versus temperature for the three considered cases, the nitrogen and SF_6 gases and three pressures for case 2. The

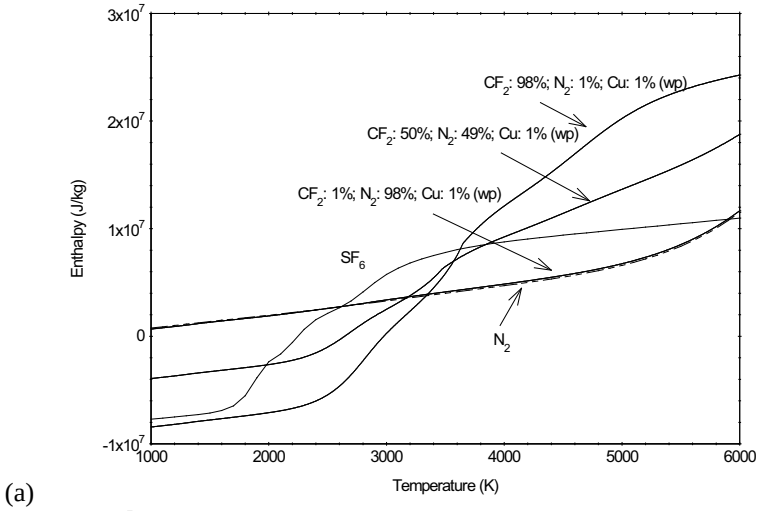

(a)

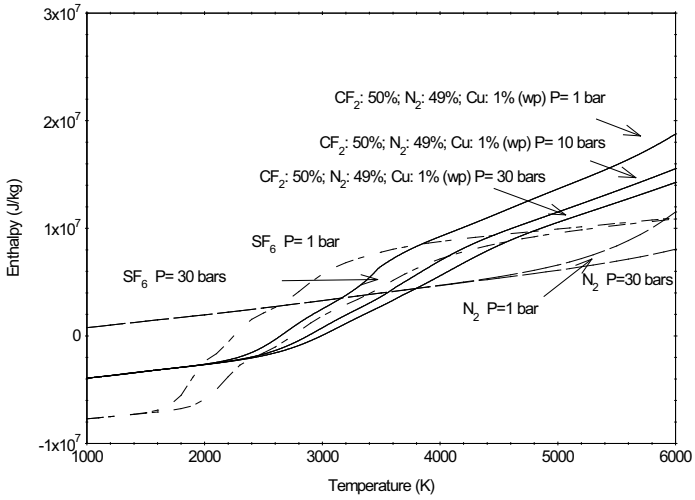

(b)

Fig. 3: Specific enthalpy versus temperature (a) at 10^5 Pa for several mixtures, SF_6 and N_2, (b) for case 2, SF_6 and N_2 at tree pressures (10^5, 10. 10^5 and 30 10^5 Pa).

nitrogen gas is considered as a reference gas due to its enthalpy of formation equal to zero (JANAF, 1998). As a matter of fact it exists at 10^5 Pa. The enthalpy of the SF_6 gas has a variation of enthalpy between 1800 K and 4000 K due to dissociation of SF_6, SF_4, and SF_2 (Brand and Kopainsky, 1978; Andre, 1997). This variation of enthalpy is useful to extinguish an electrical arc since the electrical energy from the electrical circuit is consumed by the chemical reaction in the gas. Unlike the variation of enthalpy for the nitrogen gas monotonically increases in the considered temperature range. As a matter of fact no dissociation occurs. The same conclusion can be made for the mixture of the case 1, 1% $(C_2F_4,)_n$, 98% N_2, 1% Cu in weight percent (wp) due to the fact that the main chemical species is the nitrogen (Figs. 1 and 2). For the case 2 and case 3, the variation in enthalpy in the temperature range is due to the sublimation of solid carbon and to the dissociation of CF_4 and CF_2 (Figs. 1 and 2). The increase in the enthalpy is due to the chemical reactions. The higher the pressure the higher the temperature when the chemical reactions occur. In Fig. 3b, we have plotted the specific enthalpy versus temperature in the case 2, SF_6 and nitrogen gases for three pressures 10^5, 10^6 and 30 10^5 Pa. The variation of enthalpy in SF_6 gas is due to the dissociations of gaseous species: SF_6, SF_4, and SF_2. So since the pressure increases the dissociation reactions are made at higher temperature. Concerning the case 2 the increase in enthalpy is due to the carbon sublimation and dissociation of CF_4 and CF_2 gaseous species. Even if the sublimation is abrupt (Figs 1 and 2) no shark increases in specific enthalpy is observed. As a matter of fact around the same temperature, gaseous dissociations occur. With the increase of pressure the enthalpy increases at higher temperatures. Since no dissociation occurs in the temperature range 1000 to 5000 K no variation in enthalpy for nitrogen plasma is observed in this temperature range.

5. CONCLUSION

We have presented the molar fraction and specific enthalpy versus temperature of mixture of PTFE, N_2 and Cu for several proportions and pressures. The industries, since the SF_6 gas has a very bad ecological impact, wish to replace the SF_6 gas for their electrical apparatus (electrical insulating, circuit breakers). In our previous paper, we have shown that a good proportion (stoichiometric coefficients) of SF_6 with PTFE and copper avoids the condensed phase (Andre and Koalaga, 2010; Speckhofer et al., 1999). With nitrogen the condensed phase are always present for all mixtures of PTFE, N_2 and Cu. So an electrical apparatus with nitrogen has to use a high pressure to clean and push the polluted gas far from the electrodes to avoid restriking. The energy gained by the gas flow can be similar between SF_6 gas and nitrogen gas. This energy transport, in the former case, is due to the dissociation of SF_6, SF_4 and SF_2, CF_4 and CF_2 and in the latter case due to sublimation of condensed carbon. The molar fraction of electron negative ions is low due to the fact that the N^- is unstable. Nevertheless, one can remark that the electron negative ions

are mainly due to the species from wall ablation. Finally, it seems that the nitrogen is not an available gas for electrical insulating in the existing system. To use the nitrogen, manufacturers have to change their electrical apparatus.

6. ACKNOWLEDGMENTS

The authors wish to thank the European Edulink Program RAMSES for their financial support to help the development of scientific cooperation between Blaise Pascal University and University of Ouagadougou, and the two laboratories LAME and LAEPT.

REFERENCES

P.Andre, Partition functions and concentrations in plasmas out of thermal equilibrium, *IEEE Transactions on Plasma Science*, 1995, 23(3), pp. 453–458.

P.Andre., Etude d'un plasma de SF_6 hors d'équilibre thermique, *J. Phys. III*, 1997, 7, pp. 1339–1359, (in French).

P.Andre and Z. Koalaga, Composition of a thermal plasma formed from PTFE with copper in non-oxidant atmosphere. Part I: definition of a test case with the SF_6, *JHTMP*, 2010, 14(2), pp. 285-294.

K.P.Brand and J.Kopainsky, Particle Densities in a Decaying SF_6 Plasma, *Appl. Phys.*, 1978, 16, pp. 425–432.

L.G.Chritophorou, J.K.Olthoff, and R.J.Van Brunt, Sulfur Hexafluoride and the Electric Power Industry, *IEEE Electrical Insulation Magazine*, 1997, 13(5), pp. 20–24.

F.Y.Chu, SF_6 Decomposition in Gas-Insulated Equipment, *IEEE Transactions on Electrical Insulation*, 1986, 21(5), pp. 693–725.

L.Fleischer, H.J.Müller, R.Poth, and H.Späck, Patent EP19950940161, 09/30/1998.

J.J.Gonzalez, R.Girard, and A.Gleizes, Decay and post-arc phases of a SF_6 arc plasma: A thermal and chemical non-equilibrium model, *J. Phys. D: Appl. Phys.*, 2000, 33, pp. 2759–2768.

JANAF, *Thermochemical tables*, 4^{th} edn, MW Chases (ed.), J Phys. Chem. Ref Data, 9, 1998.

J.-C.Lee and Y.J.Kim, Effects of nozzle shape on the interruption performance of thermal puffer-type gas circuit breakers, *Vacuum*, 2006, 80, pp. 599–603.

D.Koch, SF_6 properties, use in MV and HV switchgear, ECT188, Schneider Electric, 1997.

V.D.Pham, E.Thuries, J.Martin, Patent EP19910117923, 12/20/1995.

Y.Qui, A.Sun, and E.Kuffel. Improved Dielectric Strength of SF_6 Gas with a Trichlorotrifluoroethane Vapor Additive, 1987, 22(6), pp. 763–768.

D.Rochette, B W.ussière, and P.Andre, Composition, Enthalpy, and Vaporization Temperature Calculation of Ag-SiO_2 Plasmas with Air in the Temperature Range

from 1000 to 6000 K and for Pressure Included between 1 and 50 bars, *Plasma Chemistry and Plasma Processing*, 2004, 24(3), pp. 475–492.

G.Speckhofer, R.Gilles, W.Smith, and M.Bures, *A consistent Set of Thermodynamic Properties and Transport Coefficients for High-Temperature Plasmas*, in Proc. 14th ISPC, ed. Hrabovsky, Czech Republic, 1999.

Y.Yokomizu, R.Ochiai, and T.Matsumura, Electrical and thermal conductivities of high-temperature CO_2–CF_3I mixture and transient conductance of residual arc during its extinction process, *J. Phys. D: Appl. Phys.*, 2009, 42, p. 215204.